

SILICON, SILICON CARBIDE, AND GALLIUM NITRIDE NANOWIRE  
BIOSENSORS

by

Elissa H. Williams  
A Dissertation  
Submitted to the  
Graduate Faculty  
of  
George Mason University  
in Partial Fulfillment of  
The Requirements for the Degree  
of  
Doctor of Philosophy  
Chemistry & Biochemistry

Committee:

\_\_\_\_\_ Dr. John A. Schreifels, Dissertation Director  
\_\_\_\_\_ Dr. Rao V. Mulpuri, Dissertation Director  
\_\_\_\_\_ Dr. Barney Bishop, Committee Member  
\_\_\_\_\_ Dr. Robert Honeychuck, Committee  
Member  
\_\_\_\_\_ Dr. Albert V. Davydov, Committee Member  
\_\_\_\_\_ Dr. John A. Schreifels, Department Chair  
\_\_\_\_\_ Dr. Donna M. Fox, Associate Dean, Office  
of Student Affairs & Special Programs,  
College of Science  
\_\_\_\_\_ Dr. Peggy Agouris, Interim Dean, College  
of Science

Date: \_\_\_\_\_ Spring Semester 2014  
George Mason University  
Fairfax, VA

Silicon, Silicon Carbide, and Gallium Nitride Nanowire Biosensors

A Dissertation submitted in partial fulfillment of the requirements for the degree of  
Doctor of Philosophy at George Mason University

by

Elissa H. Williams  
Master of Science  
George Mason University, 2010

Directors: Dr. John A. Schreifels, Chair & Professor, Dr. Rao V. Mulpuri, Professor  
Department of Chemistry & Biochemistry

Spring Semester 2014  
George Mason University  
Fairfax, VA



This work is licensed under a [creative commons attribution-noncommercial 3.0 unported license](https://creativecommons.org/licenses/by-nc/3.0/).

## **DEDICATION**

This work is dedicated to my loving parents, Michael H. Williams and Pamela S. Williams, as well as my grandfather, Hudson H. Williams. May you rest in peace Grandpa.

## **ACKNOWLEDGEMENTS**

I would like to thank my family and friends who have been there to support me through this long journey. I would like to acknowledge the professors in the Chemistry & Biochemistry Department at George Mason University as well as the many scientists at the National Institute of Standards and Technology (NIST, Gaithersburg, MD), as they have taught me the fundamental skills and knowledge to succeed in scientific research. I would like to express my sincere gratefulness of my academic father, Dr. John A. Schreifels, as well as Dr. Rao V. Mulpuri, Dr. Albert V. Davydov, and Dr. Barney Bishop, who gave me the opportunity to grow in so many ways. I would like to thank both George Mason University and the National Institute of Standards and Technology for providing laboratory space for me to conduct research. I acknowledge, with gratitude, the financial support of the National Science Foundation (Grant #ECCS-0901712). In addition, please see the “Acknowledgments” section at the end of chapter 2, 3, and 4 for detailed contributions to each conducted research study.

## TABLE OF CONTENTS

	Page
List of Figures .....	viii
List of Abbreviations and Symbols.....	xiii
Abstract.....	xv
1: Introduction.....	1
1.1: Semiconductor Field-Effect-Transistor (FET) Based Biosensors.....	2
1.1.1: Semiconductor FET Based Biosensor Considerations .....	3
1.1.2 Types of Materials in Semiconductor FET Based Biosensors .....	6
1.2: Semiconductor Thin Film FET Based Biosensors .....	7
1.3: Semiconductor Nanowire FET Based Biosensors .....	11
1.4: Outline of Proceeding Chapters .....	17
2: Selective streptavidin bioconjugation on silicon and silicon carbide nanowires for biosensor applications.....	19
2.1: Abstract .....	19
2.2: Introduction .....	19
2.3: Experimental .....	21
2.3.1: Nanowire Growth .....	21
2.3.2: Nanowire Functionalization .....	21
2.3.3: Protein Immobilization .....	22
2.3.4: Characterization Methods.....	24
2.4: Results & Discussion .....	26
2.4.1: XPS.....	26
2.4.2: HRTEM.....	31
2.4.3: AFM .....	33
2.4.4: Fluorescence Microscopy .....	36
2.5: Conclusions .....	39
2.6: Acknowledgements .....	40

3: Solution-based functionalization of gallium nitride nanowires for protein sensor development.....	41
3.1: Abstract .....	41
3.2: Introduction .....	42
3.3: Materials & Methods.....	43
3.3.1: Experimental Design for Protein Selective Sensing.....	43
3.3.2: Nanowire Growth & Functionalization .....	45
3.3.3: Protein Immobilization .....	46
3.3.4: Characterization Methods.....	47
3.4: Results & Discussion .....	49
3.4.1: APTES Functionalization, Biotinylation & Protein Immobilization .....	49
3.4.2: Control (Specificity) Tests .....	55
3.5: Conclusions .....	57
3.6: Acknowledgements .....	59
3.7: Supplementary Data .....	59
3.7.1: HRTEM & EELS Analysis of the GaN Surface Oxide.....	59
3.7.2: Analysis of the Oxygen Plasma Cleaned and APTES-coated GaN NWs Using FESEM/EDX .....	60
3.7.3: AFM Analysis of Agglomerates on the SA Conjugated GaN NW Surface....	62
4: Lipid Encapsulated Silicon Nanowire Devices- A Novel Detection Method for Probing Bacterial Cell Membrane Mechanisms and Interactions .....	63
4.1: Abstract .....	63
4.2: Introduction .....	64
4.3: Materials & Methods.....	66
4.3.1: Device Design .....	66
4.3.2: Device Fabrication.....	67
4.3.3: Device Insulation.....	69
4.3.4: Preparation of Liposomes & Tween20.....	69
4.3.5: Device Testing.....	70
4.3.6: Optical & Fluorescence Microscopy .....	71
4.4: Results & Discussion .....	71
4.4.1: Characterization of the Si NW Devices.....	71
4.4.2: Sensor Chip Device Testing .....	73

4.4.3: Mechanism of Lipid Layer Formation & Destruction on NWs .....	77
4.5: Conclusions .....	80
4.6: Acknowledgements .....	81
5: Final Conclusions & Future Work.....	82
References.....	89

## LIST OF FIGURES

Figure	Page
Figure 1: A schematic demonstrating a semiconductor field-effect-transistor (FET) based biosensor. The solution & analyte act as the gate. ....	2
Figure 2: APTES functionalization of the semiconductor surface. ....	5
Figure 3: Biological sensing with an AlGaIn/GaN thin film based FET. A) Demonstrates the arrangement of the AlGaIn/GaN hetero-structure type FET as well as the APTES surface functionalization of FET device. B) Shows the electrical detection of biotin followed by streptavidin using the FET biosensor. Copyright: B.S. Kang, F. Ren, L. Wang, C. Lofton, W.W. Tan, S.J. Pearton, A. Dabiran, A. Osinsky, and P.P. Chow. ....	9
Figure 4: Highly selective, sensitive, and multiplexed electrical detection of the prostate specific antigen (PSA) using Si NW FET devices. Copyright: G. Zheng, F. Patolsky, Y. Cui, W.U. Wang, and C.M. Lieber. ....	12
Figure 5: The utilization of Si NW FETs to probe cellular mechanisms and interactions. A) Demonstrates how a Si NW device can be used to mimic a cell, B) shows the electrical response from a bare NW, a bilayer (BL) coated NW, and a NW with a bilayer incorporating protein pores ( $\alpha$ -HL), C) are fluorescence microscopy images of the bilayer coated NWs (scale bar is 5 $\mu$ m). Copyright: S.-C.J. Huang, A.B. Artyukhin, J.A. Martinez, D.J. Sirbully, Y. Wang, J.-W. Ju, P. Stroeve, and A. Noy. ....	14
Figure 6: Two recently developed methods for selective protein immobilization on GaN NWs. Copyright: D.J. Guo, A.I. Abdulagatov, D.M. Rourke, K.A. Bertness, S.M. George, Y.C. Lee, and W. Tan. ....	15
Figure 7: A) Cross-section FESEM image of Si NWs grown on a Si(111) substrate and B) plan-view FESEM image of 3C-SiC NWs grown on a 4H-SiC(0001) substrate. Corresponding high-magnification images of individual NW tips are shown in the insets (note solidified Au and Ni catalytic metal caps atop Si and SiC NWs in the A and B insets, respectively).....	21
Figure 8: Streptavidin (SA) and Bovine Serum Albumin (BSA) binding to APTES-coated NWs. Note: Amino groups on the NW surface after APTES functionalization exist in a $\text{NH}_3^+$ and a hydrogen bonded ( $\text{NH}_2\text{---H}$ ) form as well as free $\text{NH}_2$ groups. Only $\text{NH}_3^+$ groups are shown in the schematic to emphasize the possibility of electrostatic binding of proteins to the APTES functionalized NW surface. ....	23
Figure 9: Streptavidin (SA) binding and inhibition of Bovine Serum Albumin (BSA) binding to biotinylated NWs. Note: Unlike Figure 8, the $\text{NH}_3^+/\text{NH}_2\text{---H}$ forms of the APTES amino groups are not included in the schematic to illustrate the mechanism for the specific binding of SA after biotinylation.....	24

Figure 10: XPS spectra of Si NWs: A) as-grown; B) APTES-coated; C) biotinylated; and D) SA immobilized. The upper-left inset shows the N 1s peaks from  $\text{NH}_3^+/\text{NH}_2\text{---H}$  (401.5 eV) and  $\text{NH}_2$  (399.8 eV) after APTES functionalization; the upper-right inset shows the S 2p peaks after biotinylation; and the upper-center inset shows the C 1s signal related to SA conjugation. Note: the S 2p peak is riding on the slope of the Si 2s energy loss peak and is not discernible in the survey scans but becomes clear in the high resolution narrow scans. Also, trace amounts of Na, P, and K observed in some spectra can be attributed to residual phosphate buffer. .... 27

Figure 11: XPS spectra of SiC NWs: A) as-grown; B) APTES-coated; C) biotinylated; and D) SA immobilized. The upper-left inset shows the C 1s peaks from the as-grown SiC NWs; the second from left inset shows the N 1s peaks from  $\text{NH}_3^+/\text{NH}_2\text{---H}$  and  $\text{NH}_2$  after APTES functionalization; the next inset shows the S 2p peaks after biotinylation; and the right-most inset shows the C 1s signal related to SA conjugation. Note: same as in the Si NW case, the S 2p peak is riding on the slope of the Si 2s energy loss peak, which becomes clear in the high resolution narrow scans. Also, trace amounts of Na, P, and K observed in some spectra can be attributed to residual phosphate buffer. .... 29

Figure 12: Bright-field HRTEM images of near-edge regions of: A) as-grown Si NW with native oxide layer; B) APTES-coated Si NW; C) biotinylated Si NW; and D) fully functionalized Si NW. The 0.32 nm Si {111} lattice fringes in A)-C) indicate the  $\langle 111 \rangle$  growth direction of the Si NW. White dashed lines help guide the eye and mark the interface between the NW edge and the amorphous outer layers (native  $\text{SiO}_x$  and/or organic layers). Noteworthy, with the organic layer accumulation, the interface between the edge of the NW and the deposited organic layers, as well as the Si lattice fringes, become barely visible. Region (1) in A) refers to the oxide layer; region (2) in B) is the oxide/APTES layer; region (3) in C) represents the oxide/APTES/biotin layer; and region (4) in D) is the oxide/APTES/biotin/SA layer. The scale bars are 5 nm. .... 31

Figure 13: HRTEM images of near-edge regions of SiC NWs coated with: A) native oxide layer (region (1)); B) APTES (layer (2)); C) APTES/biotin (layer (3)); and D) APTES/biotin/SA (layer (4)). White dashed eye-guiding lines mark the interface between the NW edge and the amorphous oxide and organic layers. The 0.25 nm SiC {111} lattice fringes (labeled in A) indicate the  $\langle 111 \rangle$  growth direction of the 3C-polytype SiC NWs. Note the high density of the {111} stacking faults in 3C-SiC that are aligned  $20^\circ$  to the NW axis, clearly visible in A) and D). The scale bars are 5 nm. .... 33

Figure 14: AFM images with corresponding line scans of: A1-A3) an as-grown Si NW; B1-B3) an APTES-coated Si NW; C1-C3) a biotinylated Si NW; and D1-D3) a SA immobilized Si NW. For A1-D1) the X-Y length scale bar in A1) applies to all four images; the vertical bar on the right is the color-coded 200 nm Z-scale. For A2-D2) the line scans, taken perpendicular to the NW growth axis, show the NW cross-sectional morphologies; the inscribed dash-lined hexagons represent a schematic cross-section of the as-grown Si NW with an average diameter of 125 nm. For A3-D3) the 300 nm long line scans, taken along the NW growth axis, show typical top surface roughness after each functionalization step. .... 34

Figure 15: AFM images with corresponding line scans of: A1-A3) an as-grown SiC NW; B1-B3) an APTES-coated SiC NW; C1-C3) a biotinylated SiC NW; and D1-D3) a SA

immobilized SiC NW. For A1-D1) the X-Y length scale bar in A1) applies to all four images; the vertical bar on the right is the color-coded 170 nm Z-scale. For A2-D2) the line scans, taken perpendicular to the NW axis, show the NW cross-sectional morphologies. For A3-D3) the 300 nm long line scans, taken along the NW growth axis, show typical top surface morphology after each functionalization step. .... 36

Figure 16: Fluorescence microscopy images of APTES-coated and biotinylated Si and SiC NWs after exposure to the SA/BSA mixture. For the APTES-coated samples (columns 1 and 2), the same NW of each material is imaged for the red (SA) and green (BSA) fluorescence, respectively. Likewise, columns 3 and 4 show the response from the same biotinylated NW of each kind. The dashed ovals in column 4 mark the locations of non-fluorescing NWs, confirming the absence of non-specific BSA attachment. The 3  $\mu$ m scale bar in the upper-right square applies to all images. .... 37

Figure 17: Fluorescence intensity line profiles for the A) SA and B) BSA proteins taken across as-grown, APTES functionalized, and biotinylated SiC NWs after exposure to the SA/BSA mixture. The line profiles correspond to the SiC NWs shown in the bottom row of Figure 16 (except for the as-grown NWs). .... 38

Figure 18: Experimental reaction scheme..... 45

Figure 19: A cross-section FESEM image of GaN NWs grown on a Si(111) substrate. The magnified image in the inset shows hexagonal faceting of NW sidewalls..... 49

Figure 20: FESEM images of the GaN NW sidewalls after: A) oxygen plasma cleaning, B) APTES functionalization, C) biotinylation, and D) SA immobilization. The hexagonal faceting of the clean NW in image A) gradually disappears upon the B), C), and D) functionalization steps as surface roughening increases. The arrows in D) point to hemispherical agglomerates, likely made of SA molecules. Note: the initial diameters of the NWs in A)-D) are not the same and therefore, the NW diameter in A) cannot be subtracted from the NW diameters in B)-D) to quantitatively determine organic layer thicknesses. The 50 nm scale bar in A) applies to all images..... 50

Figure 21: HRTEM images of near edge regions of a GaN NW after: A) oxygen plasma cleaning, B) APTES functionalization, C) biotinylation, and D) SA immobilization. The 0.26 nm GaN lattice fringes, clearly evident in A)-C), indicate the [0001] c-axis NW growth direction. Arrows point out the surface layers of: A) the native oxide, B) APTES, C) APTES/biotin, and D) APTES/biotin/SA. Note: with successive organic layer accumulation, the interface between the edge of the NW and the deposited organic layers, as well as the GaN lattice fringes, become barely visible. The scale bar in the right corner of each image is 5 nm. .... 50

Figure 22: XPS narrow scans: A) N 1s scan, B) Ga 2p<sub>3/2</sub> scan, and C) Si 2p scan. For all three scans, (1) is the oxygen plasma cleaned NWs, (2) is the APTES-coated NWs, (3) is the biotinylated NWs, and (4) is the SA immobilized NWs..... 53

Figure 23: A) and B): a biotinylated GaN NW after exposure to the SA/BSA mixture under the EF.4 fluorescence filter cube for SA detection (A), and the B-2E/C fluorescence filter cube for BSA detection (B). Note: the dashed line oval in image B) marks the location of the non-fluorescing NW. C) and D): an APTES-coated GaN NW after exposure to the SA/BSA mixture under the EF.4 fluorescence filter cube for SA detection (C), and the B-2E/C fluorescence filter cube for BSA detection (D). Note:

images A) and C) were taken with a 1 s exposure time, while B) and D) with a 3 s exposure time. The 5 $\mu\text{m}$ scale bar in A) applies to all images. ....	56
Figure 24: <i>Top left image</i> : a HRTEM image of a GaN NW edge. Region ① marks the NW interior and region ② is an amorphous-like surface oxide about 1 nm thick (marked with two vertical arrows). The [0001] growth direction of the NW is indicated. <i>Bottom left picture</i> : a schematic view of the imaging geometry of the NW. <i>Right spectra</i> : representative EELS spectra of the NW interior ① (blue spectrum) and surface oxide ② (red spectrum). The Ga/N ratio in region ② (not shown) is lower than its stoichiometric value in the NW interior, which is consistent with the formation of a gallium oxide/oxy-nitride surface layer.....	60
Figure 25: EDX spectrum of a cleaned GaN NW before (red spectrum) and after (gray-shaded spectrum) APTES functionalization. The appearance of a Si peak and an increase in C and O peak intensity indicate successful binding of APTES molecules to the NW surface. Note: The Au signal arises from the underlying Au-coated substrate. ....	61
Figure 26: An AFM image of a SA immobilized GaN NW. The vertical bar on the right is the 200 nm color coded Z-scale and the horizontal bar in the lower right corner is the 400 nm X-scale. The inset shows a line scan across a typical protein agglomerate taken along the NW growth axis. ....	62
Figure 27: The Si NW sensor chip. A: The overall design of the sensor chip. The chip contains 6 NW devices, a fluid channel, and a fluid reservoir. B: A schematic of an enlarged region of one of the 6 NW devices on the sensor chip.....	67
Figure 28: Schematic of the silicon nanowire two-terminal sensor chip fabrication and insulation. A: shows the steps for sensor chip fabrication, B: shows the steps for sensor chip insulation, and C: is an image of a fabricated and insulated sensor chip.....	68
Figure 29: Left graph: current (A) versus voltage (V) curves for a Si NW device before anneal (blue diamonds), after anneal (red squares), and after PI insulation (green triangles). Right images are 50 x optical microscopy images of a Si NW device: A) before anneal, B) after anneal, and C) after polyimide insulation. The scale bar in all three images is 10 $\mu\text{m}$ . ....	72
Figure 30: Current (A) versus time (s) response of a Si NW device upon the addition of 1) 20 $\mu\text{L}$ of phosphate buffer, 2) 20 $\mu\text{L}$ of phosphate buffer, 3) 20 $\mu\text{L}$ phosphate buffer, 4) 60 $\mu\text{L}$ PC/PG liposomes, and 5) 30 $\mu\text{L}$ Tween20 solution. ....	74
Figure 31: Confocal fluorescence microscopy (at a magnification of 40 x) of a Si NW after exposure to the PC/PG liposome solution (A). A zoomed in image of the NW in (A) is shown in image (B). A fluorescence intensity line scan taken along the NW's length in image (B) is shown in (C). The red arrows in image (C) indicate the NW region with an average fluorescence intensity of 38.....	76
Figure 32: Confocal fluorescence microscopy (at a magnification of 40 x) of a Si NW after exposure to the Tween20 solution (A). A zoomed in image of the NW in (A) is shown in image (B). A fluorescence intensity line scan taken along the NW's length in image (B) is shown in (C). The red arrows in image (C) indicate the NW region with an average fluorescence intensity of 11.....	77

Figure 33: Mechanism of lipid bilayer formation/destruction on a Si NW and effect on NW conductance. A) shows the formation of the lipid bilayer with PC/PG liposomes and the destruction of the bilayer using Tween20, B) demonstrates the change in NW conductance due to lipid encapsulation. .... 78

Figure 34: Si NW FET device response to 1) phosphate buffer, 2) phosphate buffer, 3) PC/PG liposome solution, and 4) the NA-CATH antimicrobial peptide..... 85

Figure 35: Confocal fluorescence microscopy images of a Si NW FET device after exposure to PC/PG liposomes (left image) and after the application of NA-CATH to the lipid coated NW (right image). The dashed oval in the right image marks the region of the non-fluorescing NW. The scale bar in both images is 1  $\mu\text{m}$ ..... 87

## LIST OF ABBREVIATIONS AND SYMBOLS

3-Aminopropyltriethoxysilane .....	APTES
3-Mercaptopropionic acid .....	MPA
Aluminum .....	Al
Atomic force microscopy .....	AFM
Bovine serum albumin .....	BSA
Chemical vapor deposition .....	CVD
Cyanine-3 .....	Cy-3
Deoxyribonucleic acid .....	DNA
Drain .....	D
Electron energy loss spectroscopy .....	EELS
Energy dispersive x-ray spectroscopy .....	EDXS
Enzyme-linked immunosorbent assay .....	ELISA
Escherichia coli .....	<i>E. coli</i>
Field emission scanning electron microscopy .....	FESEM
Field-effect-transistor .....	FET
Fluorescein isothiocyanate .....	FITC
Fluorescence microscopy .....	FM
Four bilayer periodicity of stacking in a hexagonal lattice .....	4H
Gallium nitride .....	GaN
Gold .....	Au
High resolution transmission electron microscopy .....	HRTEM
High-electron-mobility transistor .....	HEMT
Indium .....	In
Ion-selective field-effect-transistor .....	ISFET
Metal-oxide-semiconductor field-effect-transistor .....	MOSFET
Nanowire .....	NW
National Institute of Standards and Technology .....	NIST
Phosphatidylcholine .....	PC
Phosphatidylglycerol .....	PG
Polyimide .....	PI
Prostate specific antigen .....	PSA
Silicon .....	Si
Silicon carbide .....	SiC
Silicon dioxide .....	SiO <sub>2</sub>
Small unilaminar vesicles .....	SUVs
Source .....	S

Streptavidin .....	SA
Three bilayer periodicity of stacking in a cubic lattice.....	3C
Titanium .....	Ti
X-ray photoelectron spectroscopy .....	XPS

## **ABSTRACT**

### **SILICON, SILICON CARBIDE, AND GALLIUM NITRIDE NANOWIRE BIOSENSORS**

Elissa H. Williams, Ph.D.

George Mason University, 2014

Dissertation Directors: Dr. John A. Schreifels, Dr. Rao V. Mulpuri

Semiconductor nanostructures, such as silicon (Si), silicon carbide (SiC), and gallium nitride (GaN) nanowires (NWs), arranged as the active sensing element in an electrical device, present many advantages over the conventional methods used for biological detection. While Si NWs have demonstrated compatibility towards functionalization protocols, as well as the sensitive and selective electrical recognition of a wide range of biomolecules, SiC and GaN NWs have not yet been studied extensively in their propensities towards biofunctionalization. As a result, a solution-based functionalization protocol was developed for the specific attachment of the streptavidin (SA) protein to Si, SiC, and GaN NWs for the development of portable, highly sensitive, and selective biosensors. Successful SA immobilization on the functionalized Si, SiC, and GaN NW surface was proven using fluorescence microscopy, field emission scanning electron microscopy, high resolution transmission electron microscopy, atomic force microscopy,

and x-ray photoelectron spectroscopy. After demonstrating Si, SiC, and GaN NW functionalization and biocompatibility, Si NW field-effect-transistor (FET) type devices were fabricated for sensing bacterial cell membrane interactions and mechanisms. Spontaneous formation of a lipid bilayer around Si NW devices was found to occur upon exposure to 50 nm liposomes consisting of phosphatidylcholine (PC) and phosphatidylglycerol (PG), the lipids present in an *E. coli* cell membrane. Lipid bilayer formation on the Si NWs was detected by real-time electrical resistivity changes and it was found that the negative charge associated with the PC/PG layer resulted in an induced negative gate on the NW surface and caused a 1-2 % decrease in NW conductance. A strong detergent, Tween20, was found to remove the lipid bilayer from the NW surface very quickly and result in the return of NW conductance to its baseline value in buffer. Formation and destruction of the lipid bilayer on the NW devices was also confirmed by confocal fluorescence microscopy. The *E. coli* cell membrane encapsulated Si NW FET based biosensors demonstrate a novel platform to electrically probe bacterial cell membrane reactions.

## **1: INTRODUCTION**

Detection and quantification of biological species is a necessity for all fields of the life sciences [1], [2], as well as for homeland security, environmental monitoring, and food safety [3]. Over the past few decades, there has been an increased interest in the fabrication of semiconductor based biosensors that have the ability to electrically detect and quantify biomolecules with great selectivity and sensitivity [4], [5]. The interest in electrical biosensors can be attributed to the fact that the current biosensing techniques, such as the enzyme-linked immunosorbent assay (ELISA), particle-based flow cytometric assays, gas chromatography, chemi-luminescence, fluorescence, and high density peptide arrays, to name a few, often lead to false positives, display variations in sensitivity limits, and do not meet the requirements of hand-held sensors for real-time monitoring [1], [4]. Direct electronic and label-free detection of chemical and biological molecules is one of the great promises of semiconducting devices, with the goal of delivering the desired portable, low-power, and reliable sensors [6]. The development of semiconductor label-free sensors, i.e. sensors in which the molecule of interest does not contain a tag or label, will not only minimize costs and maximize speed and throughput but also enable sensing in a wide range of environments, from point-of-care diagnostic sensing to battlefield bio-war-field sensing [6], [7]. It is therefore evident that semiconductor based biological sensors could greatly advance the fields of biochemistry and medicine by providing the

sensitive, selective, and rapid detection of chemical and biological species, pollutants, hazardous agents, and pathogens.

### 1.1: Semiconductor Field-Effect-Transistor (FET) Based Biosensors

Recently, the great promises or advantages of semiconductor based biological sensors have been realized with doped semiconductor materials configured as field-effect-transistor (FET) type devices [1], [4]–[6]. Figure 1 demonstrates a schematic in which a doped semiconductor material is arranged in a FET type device for biosensing.

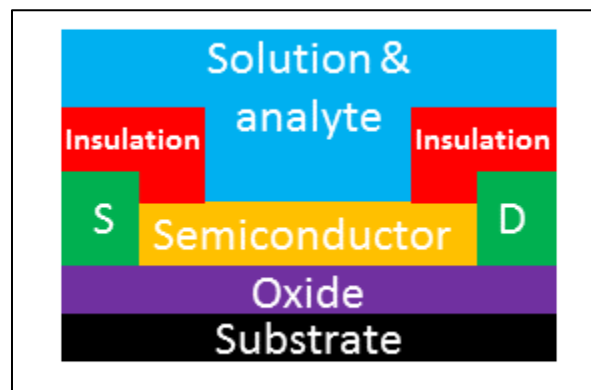


Figure 1: A schematic demonstrating a semiconductor field-effect-transistor (FET) based biosensor. The solution & analyte act as the gate.

In this device configuration, a doped semiconductor is positioned on top of an oxidized substrate, typically a silicon dioxide on silicon substrate. The semiconductor material is connected to a source and drain electrode (the source is referred to as S and the drain as D in Figure 1) which are capped with an insulating material. When a particular bias is applied between the source and drain electrodes, a specific current value in the doped semiconductor material is produced. If a solution containing a charged

biological analyte is applied to the FET device while the device is biased (see solution & analyte in Figure 1), the biological analyte will interact with the semiconductor material and change its conductivity, i.e. the solution and analyte will act as a gate. Depending on the charge of the biological molecule, and the dopant type of the semiconductor, the application of the biological analyte in solution will lead to either an increase or decrease in current in the semiconductor, i.e. a direct electrical signal upon biomolecule-semiconductor surface interaction. A positively charged biomolecule will lead to an accumulation of carriers in a n-type doped semiconductor and induce an increase in current [1], [6] or a depletion of carriers in a p-type doped semiconductor and thus a decrease in current [1], [6]. A negatively charged biomolecule will have just the opposite effect; a decrease in current in a n-type semiconductor and an increase in current in a p-type semiconductor [1], [6]. The ability of semiconductor FETs to provide direct electronic detection of biomolecules demonstrates that these devices are ideal for biological sensing.

### **1.1.1: Semiconductor FET Based Biosensor Considerations**

Not only do semiconductor FET based biosensors allow for the real-time, electrical detection of biomolecules, they also confer great sensitivity in the detection of biological species of interest [4], [8], [9]. Sensitivity of a FET device is dependent on the dimensions, as well as the surface-to-volume ratio, of the semiconductor material, the active sensing element in the device. The smaller the size of the semiconductor material, and the greater the surface-to-volume ratio, the higher the sensitivity of the FET [8], [10], [11]. With small dimensions and high surface-to-volume ratio, only a small number of

biological molecules are required to induce a detectable current change in the semiconductor. The small size and high surface-to-volume ratio of the semiconductor material also results in a fast response and short recovery time for the FET device [2]. As a consequence, the recent focus of semiconductor FET biosensors has been on the incorporation of small, high-surface-to-volume ratio nanostructures as the active sensing platform [1], [2], [6]. These nanostructured based FETs are described in more detail below in section 1.3: Semiconductor Nanowire FET Based Biosensors. The fabrication of small, high surface-to-volume ratio semiconductors and their use in FETs has resulted in sensitive, miniature, hand-held biosensors, which meet the demands of industry [4], [6], [9].

While semiconductor FET devices can lead to the direct, electronic detection of biomolecules, a FET device by itself does not confer any specificity towards a biomolecule of interest. Therefore, in order to enable FET devices that utilize the direct, selective sensing of biomolecules; one must first develop an analyte-specific functionalization of the semiconductor surface and deduce mechanisms in which the analyte molecules bind to the semiconductor. Numerous conjugation techniques have been developed for the attachment of specific biomolecules of interest to the surfaces of semiconductors. These conjugation methods often utilize various organic linking molecules [12]–[14]. One such organic linking molecule is 3-aminopropyltriethoxysilane (APTES). The covalent attachment of APTES to oxidized semiconductor materials is widely used as the first step of semiconductor surface functionalization in FET based biosensors [13]–[17]. Figure 2 demonstrates the reaction in which APTES is covalently

immobilized on a oxidized semiconductor surface, a process that is catalyzed by water [17].

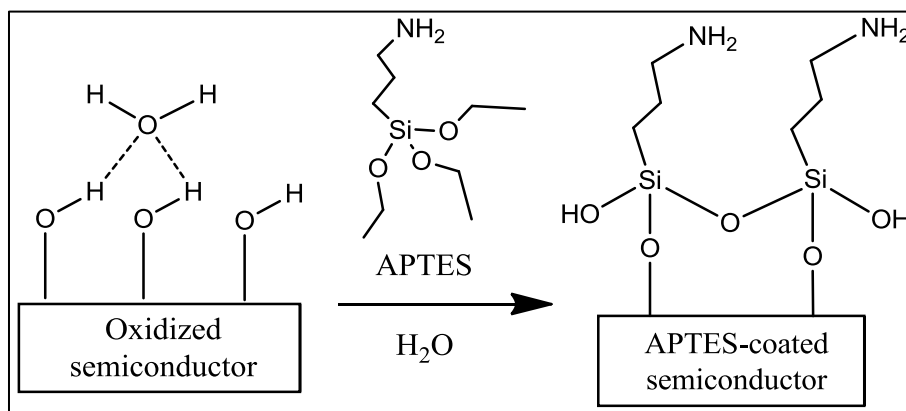


Figure 2: APTES functionalization of the semiconductor surface.

The widespread use of APTES in FET biosensor functionalization can be attributed to the fact that APTES functionalized semiconductors contain an amine terminated surface [17] and it is this amine group that confers great versatility and adaptability of the FET biosensor. Amine groups can react with any biomolecule containing or modified with an ester group, leading to the formation of a stable amide bond between the semiconductor and an analyte of interest. Evidently, APTES functionalized semiconductors are ideal for use in biosensing FETs because they permit selective binding of biomolecules of interest. In fact, APTES functionalized semiconductors of FET devices have been found to lead to the direct, selective electrical detection of proteins [8], [15], [18], peptides, strands of DNA, antigens, and antibodies [9].

### **1.1.2 Types of Materials in Semiconductor FET Based Biosensors**

Of the semiconductor materials, silicon (Si) has been most explored in FET biosensing devices due to the fact that the Si material is relatively cheap, Si is easy to dope, Si can be grown reproducibly, Si is a non-toxic and biocompatible material, and Si surface chemistries and functionalization methods are well-developed (such as the APTES functionalization scheme shown above in Figure 2) [4]. However, the wide band gap semiconductor materials, particularly silicon carbide (SiC) and gallium nitride (GaN), may have more advantages in biosensing over their Si counterpart due to improved electronic abilities, sensitivity to light which can be applicable to or exploited during the sensing process, as well as thermal stability [4], [11], [19], [20]. In addition, GaN is chemically inert towards the acids and bases encountered in biological sensing; this is not the case with the Si and SiC materials [4]. These advantages of GaN and SiC, as compared to Si, have led to their current exploration as sensing platforms in FET biosensors [15], [21].

The development of FETs for biological sensing began in the 1970s, about 30 years before the boom of nanotechnology [22]–[24]. As a consequence, FETs for biological sensing first utilized semiconductor thin films, specifically Si thin films, as the active biosensing element. Still today, work is being conducted regarding semiconductor thin film based FETs for biosensing, exploring unique semiconductor materials, such as SiC and GaN [4], [15]. However, due to the small dimensions of NWs, and thus their potential for higher sensitivity in biological detection, FETs have turned towards these nanostructured elements to serve as the active platform; primarily Si NWs, however, SiC, GaN, and other types of NWs are currently being investigated [2], [6], [8]. In the

following two sections, a short historical review of semiconductor thin film and NW based FET biosensors is presented.

## **1.2: Semiconductor Thin Film FET Based Biosensors**

The first FET based biosensor was developed by Bergveld in 1970 and was able to detect both sodium and potassium ions as well as changes in pH [23], [25]. Bergveld discovered that when the gate metal of a metal-oxide-semiconductor FET (MOSFET) was etched away, the resulting device structure was sensitive to ions in solution. The ion sensitive MOSFET device without its gate was coined as the ion-selective FET (ISFET) [23], [25]. The structure of the ion-selective FET that Bergveld used to probe ions was that of Figure 1, where the semiconductor material was doped Si and contained a thin surface oxide layer. Due to increased sensitivity compared to the conventional pH sensors at that time, these Si thin film ISFETs or pH-FETs were commercialized in the mid-1980s [5]. Any biological or chemical process that resulted in a pH change could be detected using the ISFET devices, however, the ISFETs could not directly detect biomolecule binding or biomolecule interactions [5]. As a consequence, beginning in the 1980s and still up through today, functionalization protocols for the selective binding of biomolecules of interest to the Si/SiO<sub>2</sub> thin film surface in FETs have been developed and are becoming well characterized [12], [22], [26]. Most notably utilized and studied for selective binding of biomolecules in Si thin film FETs for biosensing applications are the silane chemistries, specifically the use of APTES, as described above in section 1.1.1: Semiconductor FET Based Biosensor Considerations. With surface functionalization,

particularly silanization of the Si thin film material, FET devices have been able to demonstrate the selective electrical detection of a wide range of biomolecules [22], [25].

Throughout the years, doped Si thin films have been the main focus as the active semiconductor material in FET biosensors; however, the Si material does not come without disadvantages. Si based FETs demonstrate instability in acids, bases, or fluorine based chemicals, some of which are commonly used in biochemistry, as these compounds will etch away the Si surface [5]. The chemical limitations of Si have resulted in a shift to incorporate different semiconductor materials in FETs, such as wideband gap semiconductors. Compared to Si, wideband gap materials such as SiC and GaN are overall more efficient in many electronic processes, can withstand larger voltages, have higher thermal conductivity, are more stable over time in aqueous solution, and could potentially be more reliable and sensitive in biosensing applications [4], [5].

Within the past 10 to 15 years, the GaN thin film semiconductor material has gained quite a bit of attention for incorporation in FET biosensors. In 2005, a GaN thin film based FET was found to demonstrate a higher sensitivity to pH as compared to the Si thin film based FETs (a sensitivity of 57 mV/pH for the GaN FETs compared to 32-40 mV/pH for Si FETs) [15]. The GaN surface in the FET device was also found to be chemically inert to very high and low pH values [4], [15]. APTES functionalization of GaN thin films have been achieved, studied extensively, and found to selectively bind to biomolecules of interest [13]–[15]. In fact, GaN thin film based FET devices, surface functionalized with APTES or APTES-like silanes, have demonstrated the sensitive, selective, and real-time detection of proteins [15], enzymes [26], and DNA [27]. In

Figure 3, a sensitive and selective GaN thin film FET based biosensor is shown. Figure 3A shows the arrangement of the FET; a hetero-structure type FET with an AlGaN/GaN layer as the active sensing element that is surface functionalization with APTES for subsequent biomolecule attachment [15]. The sensitive electrical detection of the small biomolecule biotin, followed by the streptavidin protein is demonstrated by the FET device in Figure 3B [15].

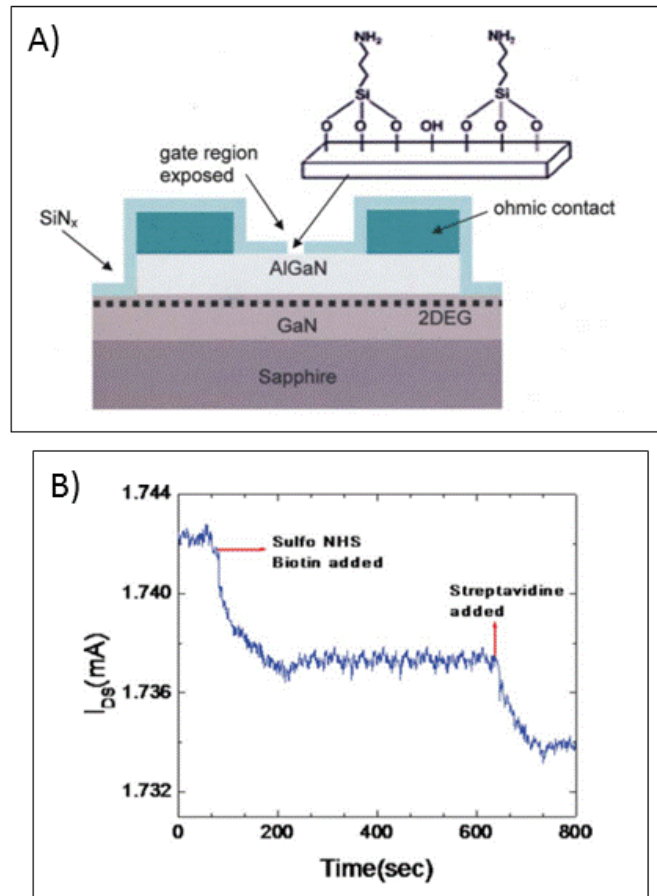


**Figure 3: Biological sensing with an AlGaN/GaN thin film based FET. A) Demonstrates the arrangement of the AlGaN/GaN hetero-structure type FET as well as the APTES surface functionalization of FET device. B) Shows the electrical detection of biotin followed by streptavidin using the FET biosensor. Copyright: B.S. Kang, F. Ren, L. Wang, C. Lofton, W.W. Tan, S.J. Pearton, A. Dabiran, A. Osinsky, and P.P. Chow.**

Research concerning GaN thin film FET based biosensors continues as these biological sensing platforms look very promising for the selective and sensitive detection of biomolecules in especially harsh environments.

SiC thin films are beginning to emerge as a potential candidate for integration into biosensing FETs as functionalization protocols enabled for Si are being proved successful on SiC. In 2007, Yakimova *et al.* studied the immobilization of APTES on the SiC thin film material as well as its subsequent functionalization with 3-mercaptopropionic acid (MPA) [19]–[21]. In 2012, Williams *et al.* revealed that APTES functionalization, followed by biotinylation of the SiC thin film surface resulted in the selective immobilization of the streptavidin protein on this semiconductor [16]. SiC thin films have been utilized in gas sensing [5], yet, their incorporation into FET biosensors has not yet been realized. However, it is clear that it is only a matter of time before SiC thin film based FETs devices demonstrate the direct, sensitive, and selective electronic detection of biomolecules.

Since the development of the first FET biosensor in 1970, great advancements have been made to not only allow for the direct electrical detection of biomolecules of interest to the semiconductor surface through the use of functionalization schemes but also improvements in the sensitivity of the FET devices by utilizing different thin film materials. However, the development of NW structures that can be grown reproducibly in bulk has completely shifted the focus of FET biosensors in the past 15 years. As discussed above in section 1.1.1: Semiconductor FET Based Biosensor Considerations, the smaller the dimensions of the semiconductor material, and the greater the surface-to-

volume ratio, the higher the sensitivity of the FET device. By incorporating semiconductor NWs as the active sensing element in a FET, extremely low limits of detection of biological compounds have been achieved [6]. A detailed discussion concerning NW based FET devices is discussed in the next section below.

### **1.3: Semiconductor Nanowire FET Based Biosensors**

The interest in the incorporation of semiconductor NWs in FET biosensors can be attributed to the following: like semiconductor thin films, semiconductor NWs display the electrical properties required for a biosensor, i.e. they allow for the direct electrical measurement of conductance/resistance changes when exposed to an analyte of interest [11], [28]. NWs can be utilized to produce a field-effect-transistor type device, such as that shown in Figure 1, where the semiconductor material represents a NW. The application of biological compounds to the FET acts as an effective gate on the NW surface leading to an increase or decrease in conductance in the NW, i.e. a direct electrical signal upon binding of a biomolecule of interest [1], [2], [6], [29]. However, in contrast to thin films, the small size of the NW permits electronic biological sensing with a minimal power requirement [4] and the high surface-to-volume ratio of the NW results in a much more sensitive sensing surface [6], [11]. Only a small number of biological molecules are required to cause detectable conductance/resistance changes in NW FETs and therefore, NWs are ideal for biosensing, especially with small volumes [4], [11]. Unlike thin films, the dimensions of NWs are comparable to that of biological molecules [1]. In addition, NW based FETs allow for the flexible assembly of multiple biomolecule specific sensing areas (functionalized NWs) on a single biosensing chip thus resulting in

multiplexed biomolecule detection. Clearly, semiconductor NWs are the ultimate material for incorporation into FETs for biosensing and present an excellent interface between the biological world and macroscopic instruments [1].

Like thin films, the Si material has been most utilized in NW based biosensors due to the fact that Si NWs can be grown reproducibly, Si is a biocompatible and non-toxic material, and Si surface chemistries and functionalization methods (see section 1.1.1: Semiconductor FET Based Biosensor Considerations) are well developed. Surface functionalized Si NW FET biosensors have demonstrated the rapid, sensitive, selective and label-free electrical recognition of small strands of DNA, enzymes, antibodies, antigens, even single virus molecules, all in real-time [1], [6], [8], [9], [29]–[31].

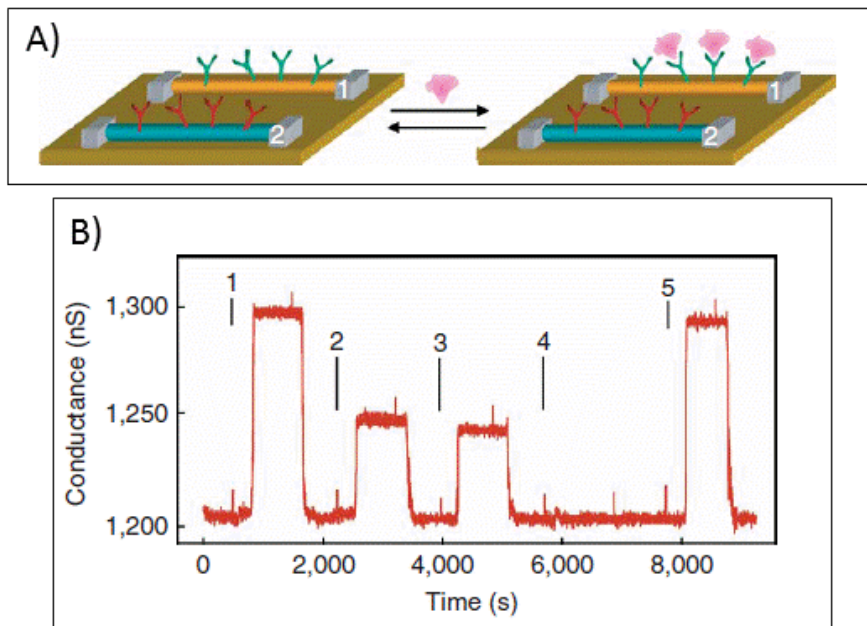
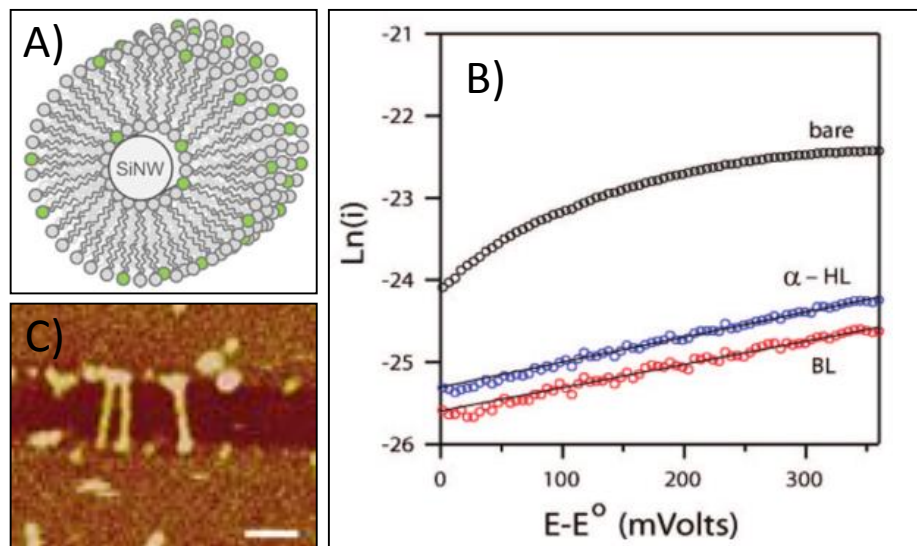


Figure 4: Highly selective, sensitive, and multiplexed electrical detection of the prostate specific antigen (PSA) using Si NW FET devices. Copyright: G. Zheng, F. Patolsky, Y. Cui, W.U. Wang, and C.M. Lieber.

Figure 4 demonstrates an example of a highly sensitive and selective Si NW FET sensor for the electrical detection of the prostate specific antigen (PSA). In Figure 4A, the NW marked as 1 is surface functionalized with antibodies specific for the attachment of PSA; the NW marked as 2 is functionalized with antibodies specific for another type of antigen. When prostate specific antigen is applied to these two NWs, PSA binds selectively to the NW marked as 1 and a conductance change is induced in the NW. There is no binding of PSA to the NW marked as 2 and therefore, the conductance in this NW remains unchanged. The Si NW FET sensor in Figure 4A is an example of multiplexed biomolecule detection; multiple biomolecule specific sensing areas (functionalized NWs) on a single biosensing chip. The conductance change in the NW marked as 1 upon the binding of different concentrations of prostate specific antigen is demonstrated in Figure 4B; (1) indicates the addition of 9 pg/mL of PSA to the device, (2) 0.9 pg/mL of PSA, (3) 0.9 pg/mL of PSA, (4) 10 mg/mL of bovine serum albumin (a control protein), and (5) 9 pg/mL of PSA. It is evident that the Si NW FET sensor in Figure 3 [32], is highly sensitive (the sensor is able to detect pg/mL levels of PSA) and is selective; the sensor only demonstrates a signal upon the addition of PSA and there is no conductance change with a control protein, bovine serum albumin. These Si NW FETs were later found to be able to detect as low as femtomolar concentrations of cancer markers, a 1,000 fold improvement over the current ELISA biosensing method [29].

The success of Si NW FET devices in the detection of biological compounds has opened up the possibility of using these nanostructured sensors to probe cellular mechanisms and interactions [30], [33], [34]. A large portion of cell reactions, however,

involve the cell membrane itself or proteins or ion channels embedded within the cell membrane [33]–[35]. As a consequence, studies have recently been carried out to encapsulate Si NW devices in a lipid bilayer as to mimic a cellular membrane in which the Si NW serves as the cell interior (see Figure 5A) [33]–[37].



**Figure 5:** The utilization of Si NW FETs to probe cellular mechanisms and interactions. A) Demonstrates how a Si NW device can be used to mimic a cell, B) shows the electrical response from a bare NW, a bilayer (BL) coated NW, and a NW with a bilayer incorporating protein pores ( $\alpha$ -HL), C) are fluorescence microscopy images of the bilayer coated NWs (scale bar is 5  $\mu\text{m}$ ). Copyright: S.-C.J. Huang, A.B. Artyukhin, J.A. Martinez, D.J. Sirbulu, Y. Wang, J.-W. Ju, P. Stroeve, and A. Noy.

A. Noy’s group demonstrated lipid bilayer formation on Si NW devices using both electrical measurements (see Figure 5B) and fluorescence microscopy (see Figure 5C). Noy’s group was also able to incorporate pore channels in the lipid encapsulated NWs and electrically detect ion transport through the pores embedded in the lipid bilayer [33]. The studies conducted in [33] and [35] reveal the potential of lipid encapsulated Si NWs as a platform to probe cellular mechanisms and interactions, particularly cell

membrane interactions [33], [34]. In addition these studies reveal that Si NW FET structures are bringing us closer and closer to being able to electrically probe cellular chemistry.

Similar to thin film FET based biosensors, researchers are moving away from the standard Si NW material and are beginning to use the more unique SiC and GaN NW materials in FETs. GaN NW based biosensors are beginning to emerge [11], [38], [39] as functionalization techniques for specific biomolecule immobilization are developed and studied [4], [27].

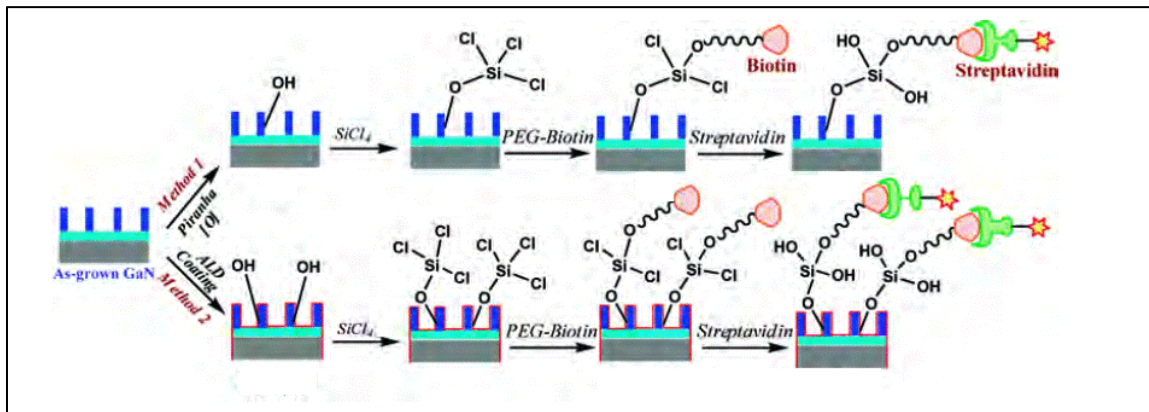


Figure 6: Two recently developed methods for selective protein immobilization on GaN NWs. Copyright: D.J. Guo, A.I. Abdulagatov, D.M. Rouke, K.A. Bertness, S.M. George, Y.C. Lee, and W. Tan.

Figure 6 demonstrates two functionalization protocols developed recently in 2010 for specific protein, i.e. streptavidin, attachment on GaN NWs [11]. In Figure 6, the GaN NWs are represented as blue bars. In Figure 6, method 1, the first step of functionalization (oxidation) is achieved by a piranha etch (a hydrogen peroxide/sulfuric acid etch) of the GaN NWs. In Figure 6, method 2, the first step of functionalization

(oxidation) is achieved by coating the NW surface with a layer of oxide using atomic layer deposition (ALD). The subsequent functionalization steps in both method 1 and 2 in Figure 6, silanization, biotinylation, and streptavidin immobilization, were identical. It was determined that the oxidized NW surface achieved by atomic layer deposition demonstrated much greater streptavidin protein attachment than the piranha oxidized NW surface [11]. Functionalization studies such as these are paving the way for selective biomolecule detection using GaN NW FET sensors.

SiC NW based biosensors have yet to be developed, however, as described in section 1.2: Semiconductor Thin Film FET Based Biosensors, bulk SiC has been shown to demonstrate successful functionalization towards specific biological analytes of interest [16], [21]. Biofunctionalization methods for Si NWs should be easily transferable to SiC NWs, and may be even more compatible with SiC, thus easing the need for functionalization protocol development [16], [21].

Si NWs have demonstrated biocompatibility towards functionalization protocols as well as the sensitive and selective electrical detection of a range of biomolecules. On the other hand, the wideband gap SiC and GaN NW materials have not yet been studied extensively in their propensities towards biofunctionalization. It is unknown if SiC and GaN NWs could be arranged in FETs to detect biological species in liquids. Since these two wideband gap semiconductor nano-materials could result in an enhanced electrical detection of biological molecules as compared to Si NW based devices, it is imperative that the biocompatibility of SiC and GaN be proven and functionalization methods for the attachment of biomolecules to SiC and GaN NW surfaces be further developed and

studied. If SiC and GaN NWs prove biocompatible, fabrication, assembly, and testing of SiC and GaN NW based biosensors could then be implemented and highly sensitive biomolecule detection could be achieved. The ineffectiveness of conventional biosensing techniques and the capabilities of Si NW based biosensors demonstrate that Si, SiC, and GaN NW FET devices need to be further investigated and studied for accurate, ultrasensitive biological detection. In addition, the successes of Si NW FET based biosensors in biological detection have opened up the possibility of using these nanostructures to probe cellular mechanisms and interactions. Preliminary studies have demonstrated that Si NW FET devices can be coated with a bilayer to mimic a cell and that even protein pores can be embedded in the bilayer on the NW surface. Additional tests are required however, to more closely probe bilayer formation and destruction on the Si NW surface for their use in studying cell reactions.

#### **1.4: Outline of Proceeding Chapters**

In this work, the following two chapters investigate the biocompatibility of Si, SiC, and GaN NWs as well as their propensities towards functionalization. A well-known functionalization protocol for the selective attachment of protein molecules on oxidized surfaces was employed on Si, SiC, and GaN NWs. Each organic layer, including the final protein step, employed in the functionalization protocol was studied on the three NW materials using surface characterization techniques including: x-ray photoelectron spectroscopy (XPS), atomic force microscopy (AFM), transmission electron microscopy (TEM), and fluorescence microscopy (FM). Functionalization and protein immobilization was successful on the Si, SiC, and GaN NWs, proving the biocompatibility of these

materials and confirming the plausibility of Si, SiC, and GaN NW FET devices for biological detection.

The fourth chapter of this work reveals a new method of utilizing Si NW FET devices to probe cellular interactions and mechanisms. More specifically, in this fourth chapter, a lipid bilayer mimicking an *E. coli* cell membrane was formed on Si NW devices. The in-situ electrical detection as well as fluorescence detection of *E. coli* cell membrane formation and destruction was observed on the Si NW FETs. This is the first report, to our knowledge of the real-time electrical detection of the encapsulation and destruction of an *E. coli*-like cell membrane on Si NW FET devices. The *E. coli* cell membrane encapsulated Si NW FET devices demonstrate a novel platform to electrically probe bacterial cell membrane mechanisms and interactions.

The fifth and final chapter of this work discusses the major accomplishments of the second through fourth chapters and describes future work that will and may come about from these studies.

## **2: SELECTIVE STREPTAVIDIN BIOCONJUGATION ON SILICON AND SILICON CARBIDE NANOWIRES FOR BIOSENSOR APPLICATIONS**

### **2.1: Abstract**

A functionalization method for the specific and selective immobilization of the streptavidin (SA) protein on semiconductor nanowires (NWs) was developed. Silicon (Si) and silicon carbide (SiC) NWs were functionalized with 3-aminopropyltriethoxysilane (APTES) and subsequently biotinylated for the conjugation of SA. Existence of a thin native oxide shell on both Si and SiC NWs enabled efficient binding of APTES with the successive attachment of biotin and SA confirmed with X-ray photoelectron spectroscopy (XPS), high-resolution transmission electron microscopy (HRTEM), and atomic force microscopy (AFM). Fluorescence microscopy demonstrated non-specific, electrostatic binding of the SA and the bovine serum albumin (BSA) proteins to APTES-coated NWs. Inhibition of non-specific BSA binding and enhancement of selective SA binding were achieved on biotinylated NWs. The biofunctionalized NWs have the potential to be employed as biosensing platforms for the specific and selective detection of proteins.

### **2.2: Introduction**

Over the past decade, there has been an increased interest in the fabrication of chemiresistive-type biosensors that have the ability to selectively detect the binding of label-free biomolecules through a mechanism in which device resistivity changes upon bioconjugation [1], [8], [40]–[43]. Surface functionalized nanowires (NWs) are ideal

active elements for such biosensors due to their high surface-to-volume ratio [42], [43]. In terms of material systems, silicon (Si) and silicon carbide (SiC) are attractive semiconductors for incorporation in biosensing devices due to their electronic properties [1], [8], [21], [43], biocompatibility [1], [8], [16], [19], [40], [41], and ability for selective functionalization towards specific analytes [1], [8], [16], [19], [40], [41].

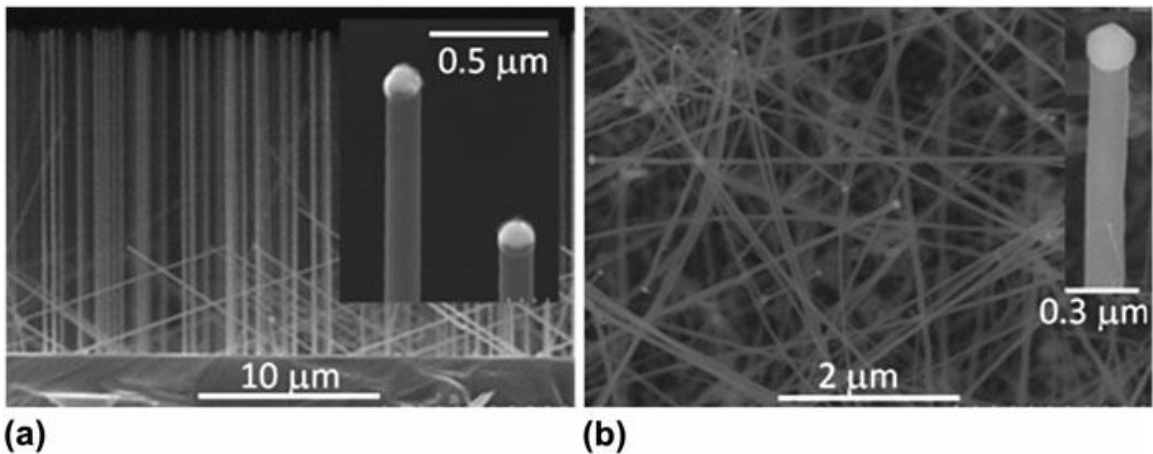
To develop semiconductor NW based devices that directly sense the binding of biomolecules through resistivity changes, an analyte-specific functionalization of the NW surface is necessary. An understanding of the mechanisms by which the functional and analyte molecules bind to the surface is essential for device fabrication and usage. Here we have presented a solution-based sequential layer functionalization method for streptavidin (SA) protein immobilization on Si and SiC NWs. This method combines the protocol for SA bioconjugation to SiC planar surfaces [16] with the “in-suspension” biofunctionalization of NWs developed for attaching DNA to Au NWs [44]. An advantage of this technique is the flexibility of parallel protein-specific functionalization of separate NW batches which enables the assembly of multi-functionalized NW arrays on a single bio-sensing chip.

Each step of the solution-based functionalization method, which included APTES functionalization, biotinylation, and protein immobilization on the NWs, was confirmed by a suite of surface analysis techniques including X-ray photoelectron spectroscopy (XPS), high-resolution transmission electron microscopy (HRTEM), atomic force microscopy (AFM), and fluorescence microscopy.

## 2.3: Experimental

### 2.3.1: Nanowire Growth

Nanowires of Si and 3C-polytype SiC were grown on Si(111) and 4H-SiC(0001) substrates respectively by chemical vapor deposition (CVD) [45], [46]. For both materials, a metal catalyst was utilized to facilitate the vapor-liquid-solid growth mechanism. NW dimensions and morphology were characterized using a Hitachi-4700 field emission scanning electron microscope (FESEM) (see Figure 7) and the NW length (diameter) values were for Si – 7  $\mu\text{m}$  to 20  $\mu\text{m}$  (110 nm to 130 nm) and for SiC – 5  $\mu\text{m}$  to 15  $\mu\text{m}$  (80 nm to 200 nm).



**(a)** Figure 7: A) Cross-section FESEM image of Si NWs grown on a Si(111) substrate and B) plan-view FESEM image of 3C-SiC NWs grown on a 4H-SiC(0001) substrate. Corresponding high-magnification images of individual NW tips are shown in the insets (note solidified Au and Ni catalytic metal caps atop Si and SiC NWs in the A and B insets, respectively).

### 2.3.2: Nanowire Functionalization

The as-grown Si and SiC NW samples were ultrasonically agitated in separate vials in 2% 3-aminopropyltriethoxysilane (APTES) solution in toluene in order to detach

the NWs from the substrates and form a suspension. After a 30 min exposure in APTES, the NW suspensions were sedimented by centrifugation for 2 min at 10,000 rpm (4 cm centrifuge rotor radius) and rinsed with toluene. The APTES functionalized NWs were re-suspended in toluene, placed onto 1 cm × 1 cm Si pieces, and allowed to air dry. Upon drying, the Si and SiC NWs adhere to the substrate surface by strong electrostatic and van der Waals forces and are resistant to removal except by extreme ultrasonication. The APTES-coated Si and SiC NWs were then analyzed using XPS, HRTEM, and AFM.

### **2.3.3: Protein Immobilization**

To examine the binding of the SA and the bovine serum albumin (BSA) proteins, the substrates coated with APTES functionalized NWs were placed in a mixture of 0.058 mg/mL streptavidin labeled cyanine-3 (SA-cy3) and 0.058 mg/mL bovine serum albumin labeled fluorescein isothiocyanate (BSA-FITC) in 0.01 mol/L sodium or potassium phosphate buffer (pH = 7.4) solution for 2 h, followed by a brief sonication, then rinsed with buffer, and dried in a N<sub>2</sub> flow (see Figure 8). Fluorescence microscopy was used to characterize the APTES functionalized NWs exposed to the SA/BSA mixture. The SA protein was utilized in this study since it is specific for biotin; BSA was used as a control protein for testing non-specific binding (BSA has no affinity for biotin).

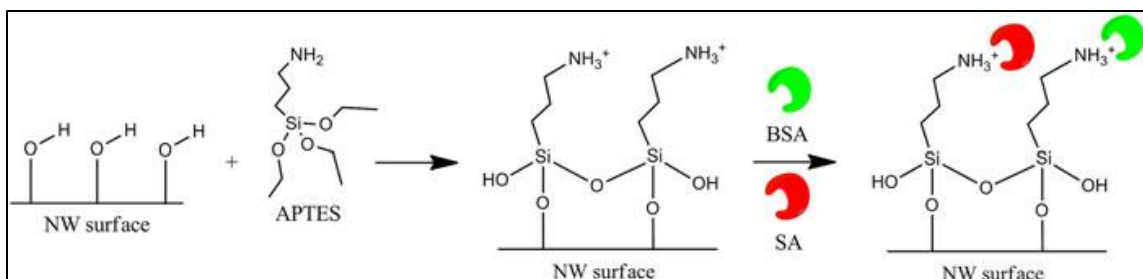


**Figure 8: Streptavidin (SA) and Bovine Serum Albumin (BSA) binding to APTES-coated NWs. Note: Amino groups on the NW surface after APTES functionalization exist in a  $\text{NH}_3^+$  and a hydrogen bonded ( $\text{NH}_2\cdots\text{H}$ ) form as well as free  $\text{NH}_2$  groups. Only  $\text{NH}_3^+$  groups are shown in the schematic to emphasize the possibility of electrostatic binding of proteins to the APTES functionalized NW surface.**

To examine the binding of the SA and the BSA proteins to the biotinylated NWs, 0.5 mL of biotin, at a concentration of 5 mg/mL in 0.01 mol/L phosphate buffer (pH = 7.4), was added to each of the two vials containing sedimented, APTES-coated Si or SiC NWs (see Figure 9). The vials were then sonicated to bring the NWs back into suspension followed by a 2 h exposure to the biotin solution. The biotinylated NW suspensions then were centrifuged, followed by removal of residual biotin solution from the vials. After rinsing in phosphate buffer, drops of the biotinylated NW batches were deposited on clean Si substrates and air dried on a hot plate at 90 °C to facilitate the evaporation of the solvent. XPS, HRTEM, and AFM were used to confirm biotinylation. The substrates with the attached biotinylated NWs were then exposed for 2 h to a 0.058 mg/mL SA only in phosphate buffer solution (for XPS, HRTEM, and AFM) or the SA/BSA mixture described above (for fluorescence microscopy) followed by a brief sonication, rinsed with phosphate buffer, and dried in a  $\text{N}_2$  flow.

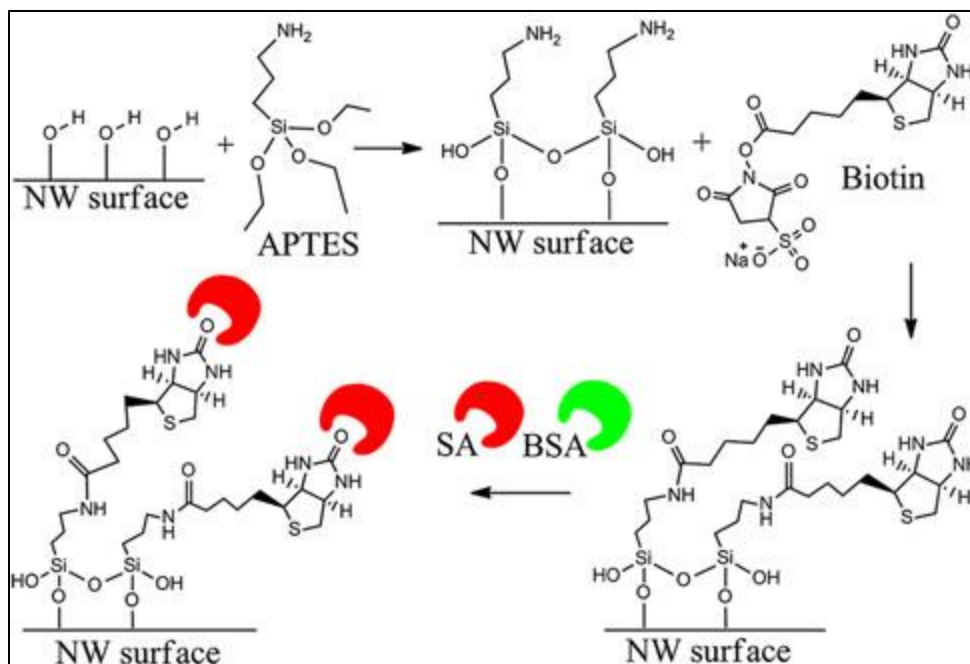


**Figure 9: Streptavidin (SA) binding and inhibition of Bovine Serum Albumin (BSA) binding to biotinylated NWs. Note: Unlike Figure 8, the  $\text{NH}_3^+/\text{NH}_2\text{---H}$  forms of the APTES amino groups are not included in the schematic to illustrate the mechanism for the specific binding of SA after biotinylation.**

Additionally, to examine the non-specific binding of SA and BSA to as-grown Si and SiC NWs, the as-grown NWs were sonicated off the substrates in vials with toluene and transferred onto clean Si pieces. As-grown NWs adhered onto the Si pieces were analyzed using XPS, HRTEM, and AFM. The Si pieces with as-grown NWs were then placed in the SA/BSA mixture described above for 2 h followed by a brief sonication, rinsed with phosphate buffer, and dried. A fluorescence microscopy analysis was then performed on the as-grown NWs after exposure to the protein mixture.

#### 2.3.4: Characterization Methods

For the XPS studies, the as-grown and functionalized Si and SiC NWs on the Si substrates were analyzed in a Kratos Analytical Axis Ultra DLD instrument with a

monochromated Al K $\alpha$  X-ray source at 150 W (10 mA, 15 kV). X-rays were collected at a 0° angle from the surface normal on an area of 300  $\mu\text{m}$   $\times$  700  $\mu\text{m}$ . Low resolution survey scans (160 eV pass energy, 0.5 eV step size) and high resolution narrow scans (40 eV pass energy, 0.1 eV step size) of O 1s, N 1s, C 1s, Si 2p, and S 2p were obtained with the data analyzed using the CasaXPS program [47]. The binding energy scale was calibrated to the C 1s, C\*-C aliphatic carbon peak at 285.0 eV. Charge neutralization was not necessary during sample analysis due to the calibration to the aliphatic C 1s peak. In addition, SiC NWs were also dispersed on indium foil to circumvent the contributions of the Si peaks from the Si substrate; In 3d high resolution narrow scans were also obtained in this case.

The Si and SiC NWs were examined by HRTEM to determine the efficacy and the layer thickness after each functionalization step. The morphology and microstructure of the as-grown and coated NWs were characterized at room temperature on a FEI Titan 80-300 TEM, equipped with S-TWIN objective lenses, at a 300 kV accelerating voltage. Low intensity illumination conditions and beam blanking were used to minimize possible radiation damage of the organic layers.

The surface topography and morphology of the as-grown and functionalized Si and SiC NWs were investigated with a Veeco DI Dimension AFM on a 1  $\mu\text{m}$   $\times$  1  $\mu\text{m}$  scale in tapping mode. Images were analyzed using WSxM v5.0 software [48].

Fluorescence microscopy of the as-grown, APTES-coated, and biotinylated Si and SiC NWs, after exposure to the SA/BSA mixture, was performed using a Nikon Eclipse TE300 inverted epifluorescence microscope with a Plan Apo 60 x (N.A. 1.4) oil

immersion objective. SA-cy3 was imaged using a Nikon EF.4 filter cube with an excitation of 515 nm to 565 nm at a 1 s exposure time. BSA-FITC was imaged using the Nikon B-2E/C filter cube with an excitation of 465 nm to 495 nm at a 9 s exposure time; the relatively long exposure time of 9 s was necessary to enhance the weak fluorescence signal of BSA. A fluorescence intensity analysis of the recorded images was performed using the ImageJ v1.45 software [49].

## **2.4: Results & Discussion**

### **2.4.1: XPS**

The XPS spectra from the Si NWs after each functionalization step are shown in Figure 10, A-D. The XPS spectrum of the as-grown Si NWs on Si (Figure 10, A) shows elemental silicon, Si 2p<sub>3/2</sub> at 98.1 eV, and two peaks originating from the SiO<sub>x</sub> native oxide, a Si 2p peak at 103.1 eV and an O 1s peak at 532.5 eV [50]. Notably, a thin amorphous oxide layer, often in a hydroxylated state, is formed on the Si NW surface upon exposure to lab air [51], [52]. This hydroxyl terminated oxide shell on the NW is necessary for subsequent APTES hydrolysis and condensation reactions [21] (see Figure 8 and Figure 9). The C 1s peaks at 285.0 eV and 286.6 eV are indicative of surface contamination with residual hydrocarbons [50]. Note that the Si substrate also generates a similar XPS spectrum and likely contributes to the spectrum from the randomly distributed Si NWs in Figure 10, A, as the NWs are not evenly distributed on the Si substrate and there are regions on the substrate which have no NWs.

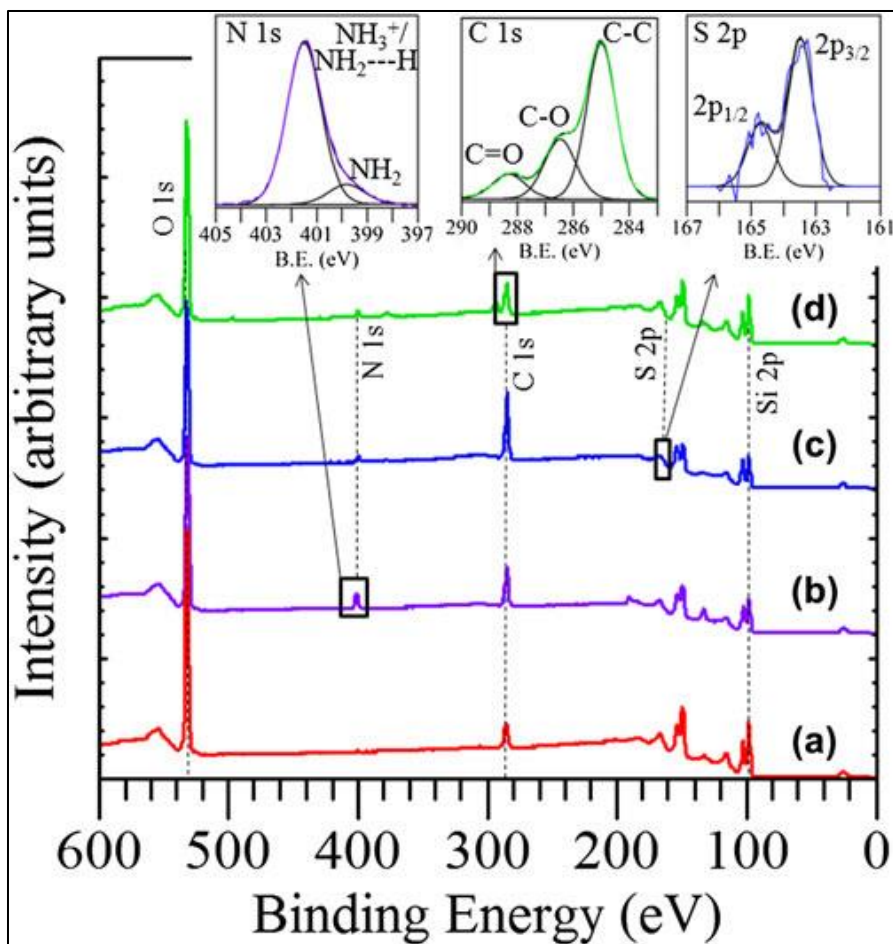


**Figure 10: XPS spectra of Si NWs: A) as-grown; B) APTES-coated; C) biotinylated; and D) SA immobilized. The upper-left inset shows the N 1s peaks from  $\text{NH}_3^+/\text{NH}_2\text{---H}$  (401.5 eV) and  $\text{NH}_2$  (399.8 eV) after APTES functionalization; the upper-right inset shows the S 2p peaks after biotinylation; and the upper-center inset shows the C 1s signal related to SA conjugation. Note: the S 2p peak is riding on the slope of the Si 2s energy loss peak and is not discernible in the survey scans but becomes clear in the high resolution narrow scans. Also, trace amounts of Na, P, and K observed in some spectra can be attributed to residual phosphate buffer.**

Upon APTES functionalization of the Si NWs, a nitrogen peak appears on the XPS spectrum (Figure 10, B and upper-left inset). This peak confirms APTES conjugation to the NW surface since APTES contains a terminal amino group as indicated in Figure 8 and Figure 9. The N 1s peak can be de-convoluted into two peaks at 401.5 eV and 399.8 eV [14], [53], [54]. The peak at 401.5 eV represents a  $\text{NH}_3^+$  group (as in Figure 8) or a hydrogen bonded  $\text{NH}_2\text{---H}$  and the peak at 399.8 eV is

indicative of a free  $\text{NH}_2$  (as in Figure 9) [14], [53], [54]. The terminal amino group on the NW surface may exist in all three forms at the  $\text{pH} = 7.4$  utilized in this study, as it was also observed by XPS in our previous work utilizing the same  $\text{pH}$  [16].

Following biotinylation of the APTES-coated Si NWs, a sulfur 2p doublet appears on the spectrum ( $\text{S } 2\text{p}_{3/2}$  at 163.5 eV and  $\text{S } 2\text{p}_{1/2}$  at 164.7 eV, Figure 10, C, and upper-right inset). The sulfur peak can be attributed to the sulfur atom contained within the tetrahydrothiophene-ring of biotin (see Figure 9), indicating that biotin is bound to the APTES functionalized NW surface. Samples analyzed after SA immobilization show C 1s peaks ( $\text{C}^*-\text{C}$  at 285.0 eV,  $\text{C}^*-\text{O}$  at 286.5 eV, and  $\text{C}^*=\text{O}$  at 288.3 eV, see Figure 10, upper-center inset) consistent with SA immobilization [55] as well as a N 1s peak (see Figure 10, D) [55], [56].

The XPS spectra from the SiC NWs on Si after each functionalization step are shown in Figure 11, A-D. The XPS spectrum of the as-grown SiC NWs on a Si substrate (Figure 11, A and upper-left C 1s inset) shows a  $\text{C}^*-\text{Si}$  peak at 283.4 eV [50]. The Si 2p region of the spectrum is dominated by the substrate, which is composed of elemental Si with a thin  $\text{SiO}_x$  native oxide layer, and makes it difficult to distinguish the  $\text{Si}^*-\text{C}$  peak. Additional measurements of the as-grown NWs dispersed on indium foil also show the silicon carbide characteristic  $\text{C}^*-\text{Si}$  peak at 283.0 eV and the Si 2p  $\text{Si}^*-\text{C}$  peak at 100.9 eV (XPS spectrum not shown). Also present is a small  $\text{Si}^*-\text{O}_x$  peak at 103.2 eV due to the native oxide shell on the SiC NW surface (XPS spectrum not shown) [50], [57].

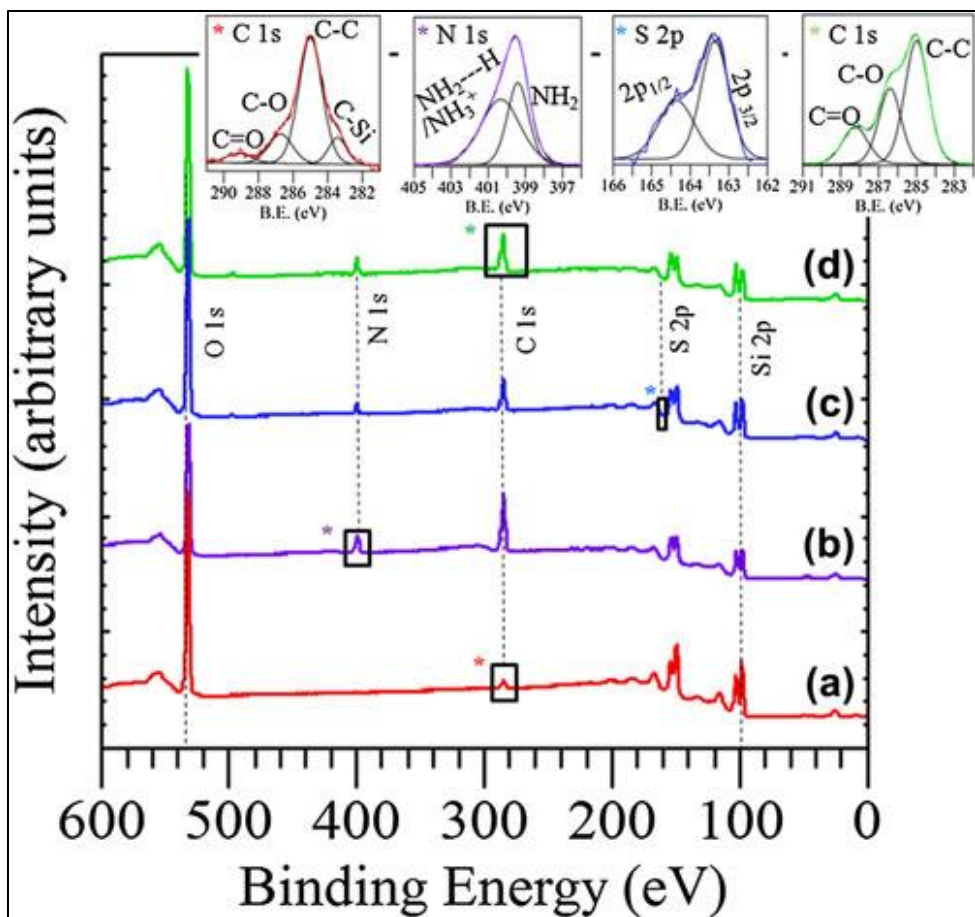


Figure 11: XPS spectra of SiC NWs: A) as-grown; B) APTES-coated; C) biotinylated; and D) SA immobilized. The upper-left inset shows the C 1s peaks from the as-grown SiC NWs; the second from left inset shows the N 1s peaks from  $\text{NH}_3^+/\text{NH}_2\text{---H}$  and  $\text{NH}_2$  after APTES functionalization; the next inset shows the S 2p peaks after biotinylation; and the right-most inset shows the C 1s signal related to SA conjugation. Note: same as in the Si NW case, the S 2p peak is riding on the slope of the Si 2s energy loss peak, which becomes clear in the high resolution narrow scans. Also, trace amounts of Na, P, and K observed in some spectra can be attributed to residual phosphate buffer.

In the C 1s high resolution scan of the SiC NWs on Si, shown in the top-left inset of Figure 11, additional peaks are present at 285.0 eV ( $\text{C}^*\text{-C}$ ), 286.7 eV ( $\text{C}^*\text{-O}$ ), and 289.1 eV ( $\text{C}^*=\text{O}$ ) [50]. These peaks are potentially indicative of significant hydrocarbon contamination of the SiC NWs [50], [57], [58]. Alternately, the  $\text{C}^*\text{-O}$  peak could be originating from the potential presence of  $\text{SiC}_x\text{O}_y$  oxycarbides in the native oxide shell on the SiC NWs [59], as well as the decomposition products of absorbed  $\text{CO}_2$  on the NW,

and/or the oxidation of free graphite possibly present on the SiC NW surface [57], [60], [61]. The C\*=O peak could be attributed to absorbed CO<sub>2</sub> molecules on the NW surface and/or the oxidation of free carbon atoms on the NW [57], [60], [61].

Upon APTES functionalization of the SiC NWs, a nitrogen peak appears on the XPS spectrum (Figure 11, B and left-center inset). The N 1s peak can be de-convoluted into two, NH<sub>3</sub><sup>+</sup>/NH<sub>2</sub>---H (400.1 eV) and NH<sub>2</sub> (399.3 eV), peaks [14], [53], [54]. Similar to the Si NWs, the N 1s peak confirms APTES functionalization and the existence of the terminal amino group in a protonated/hydrogen bonded or de-protonated form. Like the Si NW case, successful conjugation of an APTES layer to the SiC surface was likely facilitated by the presence of a hydroxylated native oxide on the SiC surface [21], [62], [63], since termination of the SiC and Si surfaces with silanol groups is necessary for the reaction and covalent attachment of APTES molecules (see step 1 in Figure 8 and Figure 9).

Following biotinylation of the APTES-coated SiC NWs, a sulfur 2p doublet appears on the spectrum (S 2p<sub>3/2</sub> at 163.4 eV and S 2p<sub>1/2</sub> at 164.4 eV, Figure 11, C and right-center inset). Like the Si NWs, the sulfur peak can be attributed to the sulfur atom contained within biotin and indicates that biotin is bound to the APTES functionalized SiC NW surface. The SiC NWs analyzed after SA immobilization show similar C 1s peaks consistent with SA immobilization [54] as well as the N 1s peak (see Figure 11, D and upper-right inset) that was also found on the SA immobilized on Si NWs [54], [55].

### 2.4.2: HRTEM

HRTEM was utilized to examine the morphology and thickness of the layers on the Si NW surface upon functionalization. The bright-field HRTEM image of the near-edge region of an as-grown Si NW is shown in Figure 12, A. The  $\{111\}$  lattice fringes, with a spacing of 0.32 nm, are perpendicular to the NW edge and indicate the  $\langle 111 \rangle$  growth direction of the NW. The image displays an approximate 3 nm to 5 nm thick  $\text{SiO}_x$  native amorphous oxide on the NW surface (see region (1), Figure 12, A), in agreement with the XPS results.

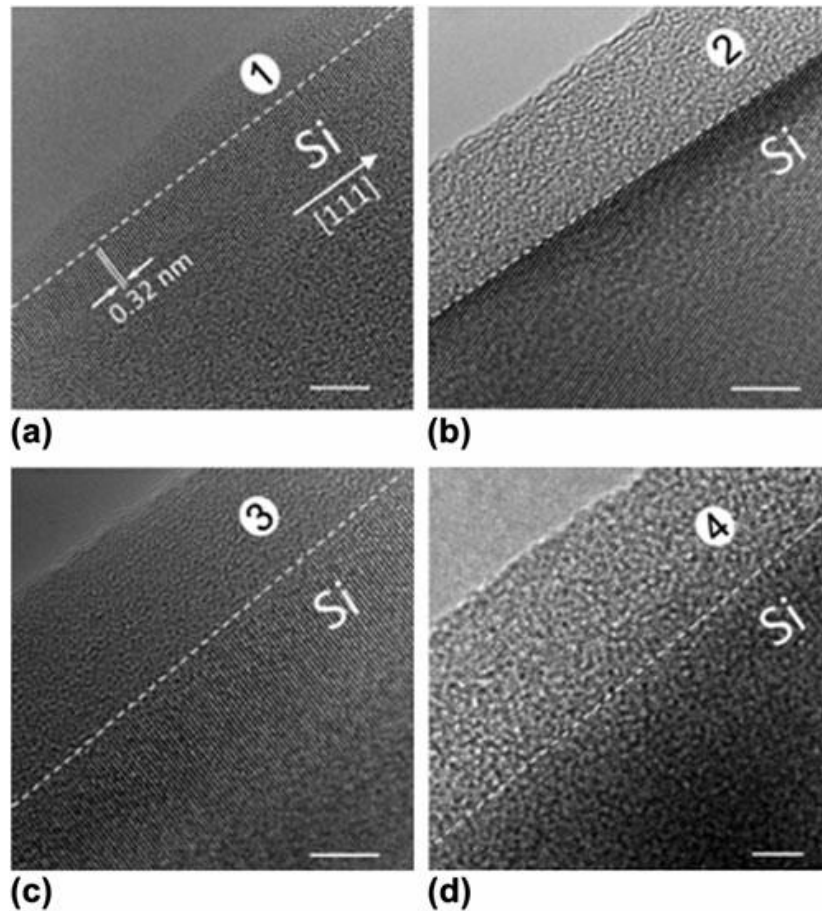


**Figure 12: Bright-field HRTEM images of near-edge regions of: A) as-grown Si NW with native oxide layer; B) APTES-coated Si NW; C) biotinylated Si NW; and D) fully functionalized Si NW. The 0.32 nm Si  $\{111\}$  lattice**

fringes in A)-C) indicate the  $\langle 111 \rangle$  growth direction of the Si NW. White dashed lines help guide the eye and mark the interface between the NW edge and the amorphous outer layers (native  $\text{SiO}_x$  and/or organic layers). Noteworthy, with the organic layer accumulation, the interface between the edge of the NW and the deposited organic layers, as well as the Si lattice fringes, become barely visible. Region (1) in A) refers to the oxide layer; region (2) in B) is the oxide/APTES layer; region (3) in C) represents the oxide/APTES/biotin layer; and region (4) in D) is the oxide/APTES/biotin/SA layer. The scale bars are 5 nm.

Following the successive attachment of APTES, biotin, and SA to the NW surface, HRTEM images in Figure 12, B-D, show an accumulation of 10 nm to 30 nm thick amorphous layers on the NW surface (see regions (2), (3), and (4)).

HRTEM data for SiC NWs demonstrates common similarities with the Si NWs regarding the appearance of a 2 nm to 5 nm thick native oxide layer (Figure 13, A, region (1)) and biocompatibility towards APTES (Figure 13, B, region (2)), biotin (Figure 13, C, region (3)), and SA (Figure 13, D, region (4)). The thickness of amorphous-like organic layers usually ranges from about 7 nm to 20 nm. Compared with the APTES/biotin/SA conjugation to planar SiC surfaces from our previous study [16], the accumulation of organic layers on the NW surface is several times thicker (e.g.,  $\approx 20$  nm on the NW surface versus  $\approx 5$  nm on the planar SiC surface) and is less homogeneous. Therefore, further optimization of the bioconjugation steps on non-planar (3D) surfaces with nano-scale dimensions is necessary in order to achieve more uniform organic layer depositions with controlled thicknesses for reliable NW based biosensing platforms.

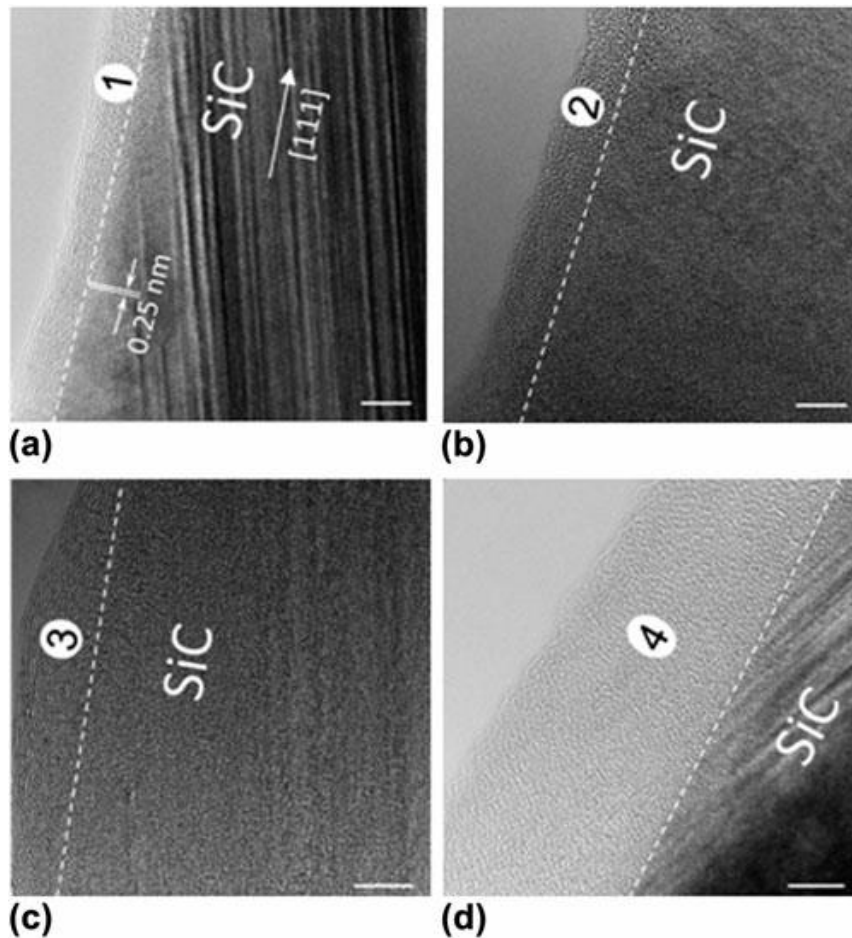


**Figure 13:** HRTEM images of near-edge regions of SiC NWs coated with: A) native oxide layer (region (1)); B) APTES (layer (2)); C) APTES/biotin (layer (3)); and D) APTES/biotin/SA (layer (4)). White dashed eye-guiding lines mark the interface between the NW edge and the amorphous oxide and organic layers. The 0.25 nm SiC {111} lattice fringes (labeled in A) indicate the  $\langle 111 \rangle$  growth direction of the 3C-polytype SiC NWs. Note the high density of the {111} stacking faults in 3C-SiC that are aligned  $20^\circ$  to the NW axis, clearly visible in A) and D). The scale bars are 5 nm.

### 2.4.3: AFM

Figure 14 shows the AFM images (A1-D1), cross-sectional profiles (A2-D2), and surface profiles (A3-D3) of Si NWs after each functionalization step. The schematic NW hexagonal cross-section corresponding to the typical NW diameter of 125 nm is inscribed inside each of the AFM cross-sectional line profiles in Figure 14, A2-D2 to facilitate visualization of the APTES, biotin, and SA layer buildup at each functionalization step.

First, the AFM scan and line profiles of an as-grown NW reveal faceted sidewalls (cross-sectional profile in Figure 14, A2) with smooth surfaces (surface profile in Figure 14, A3). The cross-sectional profile in Figure 14, A2 corresponds well to the Si NW shape observed in FESEM (Figure 7, A), with a slight over estimation of the NW diameter due to AFM tip convolution. Each successive coating leads to a loss of faceting (Figure 14, B2-D2), and an increase in surface roughness (Figure 14, B3-D3) due to the formation of organic molecule conglomerates. SA conjugation results in the formation of the largest composite structures,  $\approx 25$  nm in height, on the NW surface (Figure 14, D3).

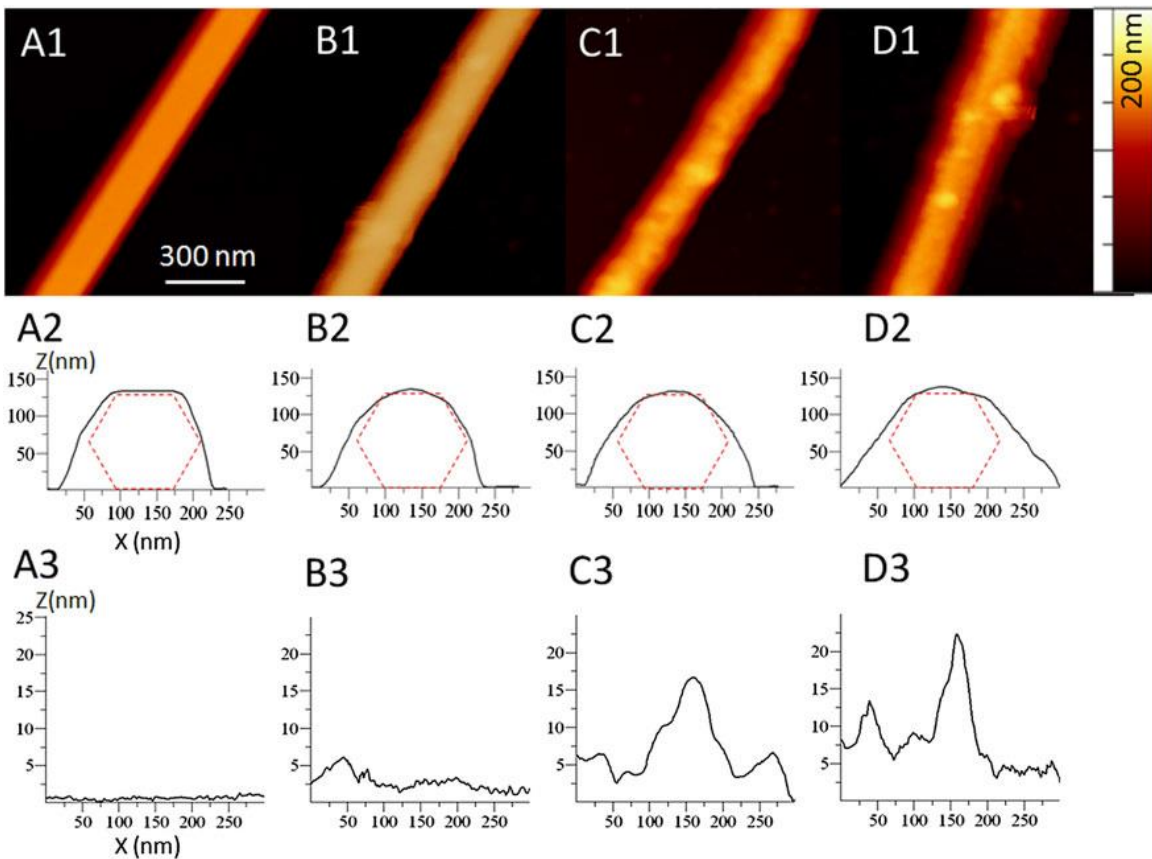


**Figure 14:** AFM images with corresponding line scans of: A1-A3) an as-grown Si NW; B1-B3) an APTES-coated Si NW; C1-C3) a biotinylated Si NW; and D1-D3) a SA immobilized Si NW. For A1-D1) the X-Y length scale

bar in A1) applies to all four images; the vertical bar on the right is the color-coded 200 nm Z-scale. For A2-D2) the line scans, taken perpendicular to the NW growth axis, show the NW cross-sectional morphologies; the inscribed dash-lined hexagons represent a schematic cross-section of the as-grown Si NW with an average diameter of 125 nm. For A3-D3) the 300 nm long line scans, taken along the NW growth axis, show typical top surface roughness after each functionalization step.

Figure 15 shows the AFM images (A1-D1), cross-sectional profiles (A2-D2), and surface profiles (A3-D3) of a SiC NW before and after functionalization. The AFM scan of an as-grown NW reveal a cylindrical-like shape with  $\approx 100$  nm diameter and smooth sidewalls (Figure 15, A1-A3). Similar to the Si NWs, each functionalization step (APTES, biotin, and SA) results in an increase in the diameter of the NW as the molecules adhere and form layers (Figure 15, B2-D2). Like the Si NWs, there is an increase in the NW surface roughness with each functionalization step (Figure 15, B3-D3) due to organic molecule conglomeration. The formation of round-shape features of up to 20 nm in diameter is clearly identifiable in Figure 15, C1, C3, and D1, D3.

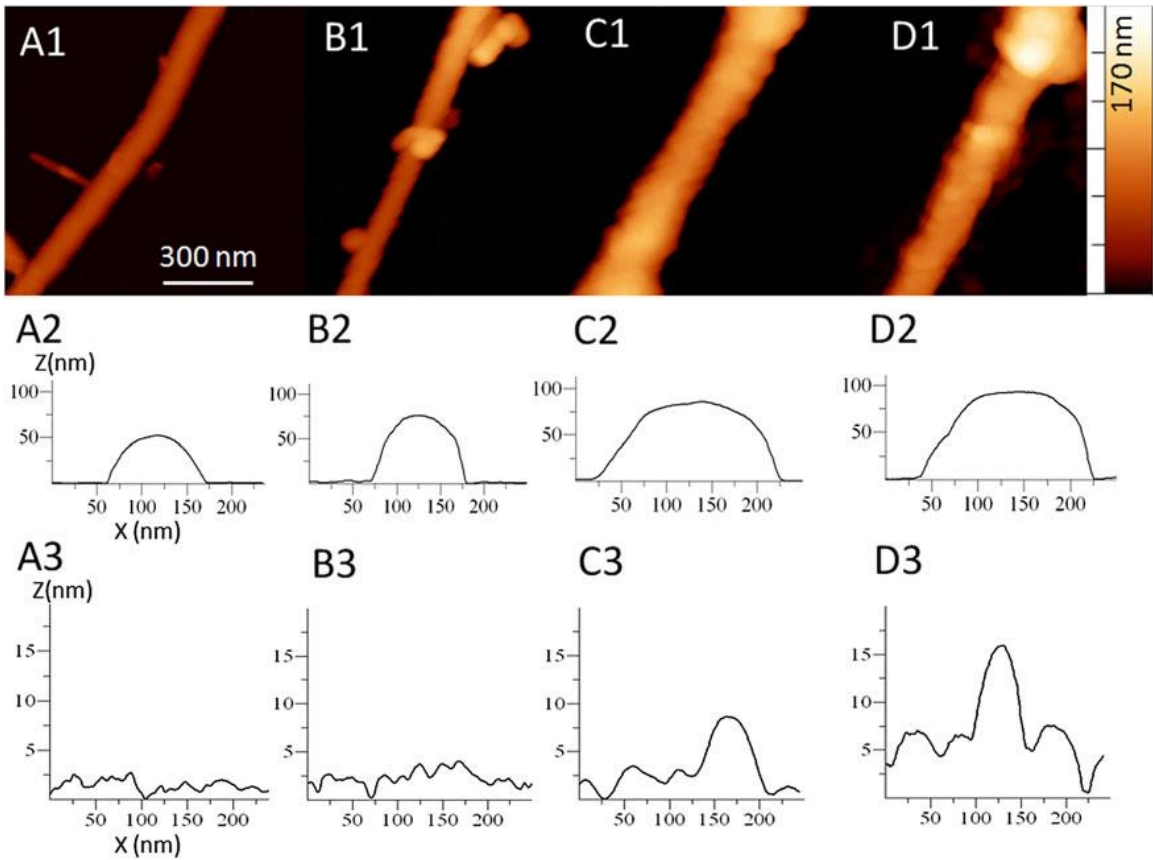


**Figure 15:** AFM images with corresponding line scans of: A1-A3) an as-grown SiC NW; B1-B3) an APTES-coated SiC NW; C1-C3) a biotinylated SiC NW; and D1-D3) a SA immobilized SiC NW. For A1-D1) the X-Y length scale bar in A1) applies to all four images; the vertical bar on the right is the color-coded 170 nm Z-scale. For A2-D2) the line scans, taken perpendicular to the NW axis, show the NW cross-sectional morphologies. For A3-D3) the 300 nm long line scans, taken along the NW growth axis, show typical top surface morphology after each functionalization step.

#### 2.4.4: Fluorescence Microscopy

As-grown, APTES-coated, and biotinylated Si and SiC NWs were exposed to an SA/BSA mixture and then analyzed using fluorescence microscopy to assess the efficiency of protein binding (see Figure 16).

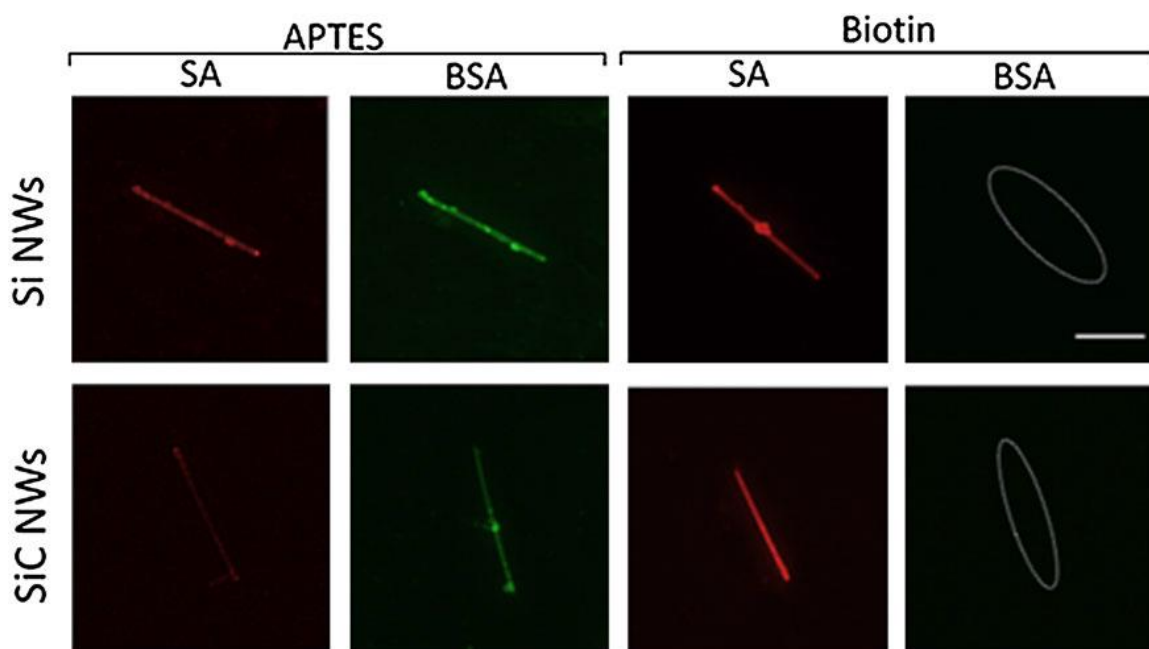


**Figure 16:** Fluorescence microscopy images of APTES-coated and biotinylated Si and SiC NWs after exposure to the SA/BSA mixture. For the APTES-coated samples (columns 1 and 2), the same NW of each material is imaged for the red (SA) and green (BSA) fluorescence, respectively. Likewise, columns 3 and 4 show the response from the same biotinylated NW of each kind. The dashed ovals in column 4 mark the locations of non-fluorescing NWs, confirming the absence of non-specific BSA attachment. The 3  $\mu\text{m}$  scale bar in the upper-right square applies to all images.

As expected, untreated (as-grown) Si and SiC NWs exposed directly to the SA/BSA protein mixture exhibit no fluorescence under the EF.4 and B-2E/C filter cubes, respectively (images not shown). The native oxides on the Si and SiC NW surfaces likely carry some negative surface charge (in the form of  $\text{O}^-$  species), and therefore repel the BSA and SA protein molecules, which are also negatively charged at the working pH of 7.4 [64]. This interaction results in little, if any, protein conjugation to the NW surface (fluorescence images not included in Figure 16, but the noise-level intensity line profiles for the as-grown SiC NWs exposed to SA/BSA are shown in Figure 17 as dotted lines).

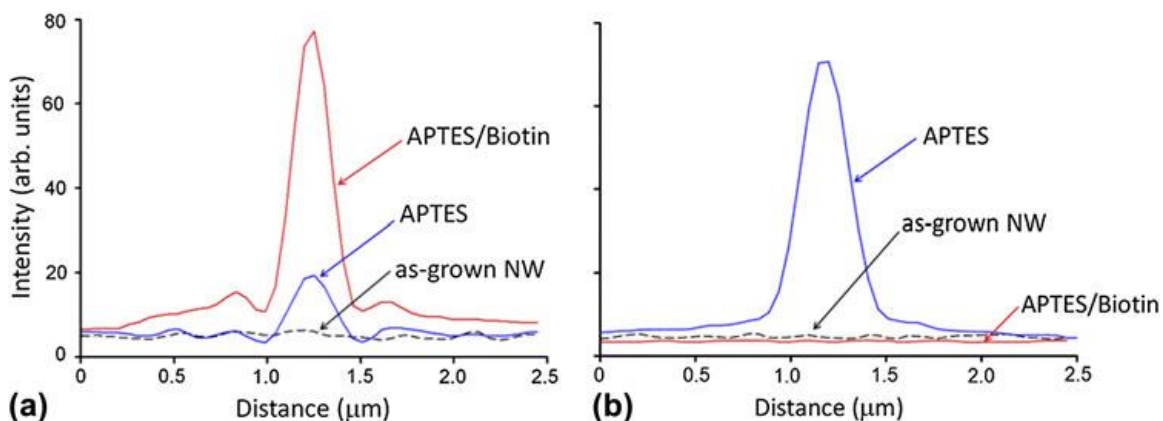


**Figure 17:** Fluorescence intensity line profiles for the A) SA and B) BSA proteins taken across as-grown, APTES functionalized, and biotinylated SiC NWs after exposure to the SA/BSA mixture. The line profiles correspond to the SiC NWs shown in the bottom row of Figure 16 (except for the as-grown NWs).

In contrast, APTES-coated Si and SiC NWs exposed to a SA/BSA mixture demonstrated noticeable conjugation of both proteins as evidenced from columns 1 and 2 in Figure 16. This non-specific attachment can be attributed to the electrostatic attraction between the  $\text{NH}_3^+/\text{NH}_2\text{---H}$  groups in APTES (the presence of which was confirmed by XPS in Figure 10 and Figure 11), and the negatively charged SA and BSA molecules (see Figure 8) [64], [65].

Non-specific protein attachment is eliminated by completing the surface functionalization protocol with the biotinylation step. As can be seen from Figure 16, the biotinylated Si and SiC NWs exhibit bright red SA fluorescence (column 3 in Figure 16) and minimal green BSA fluorescence (column 4 in Figure 16) indicating significant attachment of SA to the biotinylated NW surfaces but little non-specific attachment of BSA. This can be attributed to the fact that BSA has no affinity for biotin, while SA exhibits a strong, specific, non-covalent interaction with biotin (see Figure 9) [16]. The attachment of only SA to the fully processed Si and SiC NWs confirms that the NW

surfaces were successfully biotinylated using the solution-based functionalization technique.

## **2.5: Conclusions**

A biofunctionalization method for SA protein conjugation to biotinylated Si and SiC NWs was developed and validated using a suite of surface characterization techniques. The 2-step, all solution-based protocol included an initial coating of the NW surfaces with APTES followed by the attachment of biotin. Successful attachment of APTES is likely promoted by the presence of thin native oxide shells on the Si and SiC NWs, inducing chemical reactions between the oxidized/hydroxylated surfaces and the APTES molecules.

Fluorescence microscopy revealed that APTES-coated NW surfaces were prone to non-specific attachment of proteins due to the electrostatic attraction of SA and BSA molecules to the amine terminalized NW surfaces [64], [65]. The application of biotin to the APTES-coated NWs inhibited BSA binding while promoting the strong, specific, non-covalent interaction between SA and the biotinylated NW surfaces. The XPS, HRTEM, AFM, and fluorescence microscopy surface characterization techniques revealed that both materials, Si and SiC, display the same tendencies toward functionalization for the described bioconjugation protocol. APTES/biotin functionalized Si and SiC NW surfaces present selective and specific SA conjugation, making both of these semiconductors suitable for NW based sensing platforms for the multiplexed electrical detection of biological analytes.

## **2.6: Acknowledgements**

The authors are appreciative of the helpful discussions with Dr. Marlon L. Walker (Material Measurement Laboratory, NIST) and Dr. Rebecca A. Zangmeister (Material Measurement Laboratory, NIST) as well as the assistance of Dr. Anthony G. Birdwell (Sensors & Electronic Devices Directorate, Army Research Laboratory). EHW, MVR, and JAS gratefully acknowledge the financial support of the National Science Foundation (Grant # ECCS-0901712); VPO gratefully acknowledges the financial support from NIST under contracts SB134110SE0579 and SB134111SE0814. AKM was supported by a contractual appointment to the U.S. Army Research Laboratory Postdoctoral Fellowship Program administered by Oak Ridge Associated Universities.

### **3: SOLUTION-BASED FUNCTIONALIZATION OF GALLIUM NITRIDE NANOWIRES FOR PROTEIN SENSOR DEVELOPMENT**

#### **3.1: Abstract**

A solution-based functionalization method for the specific and selective attachment of the streptavidin (SA) protein to gallium nitride (GaN) nanowires (NWs) is presented. By exploiting streptavidin's strong affinity for its ligand biotin, SA immobilization on GaN NWs was achieved by exposing the GaN NW surface to a 3-aminopropyltriethoxysilane (APTES) solution followed by reaction with biotin. Functionalization of the NWs with APTES was facilitated by the presence of an  $\approx 1$  nm thick surface oxide layer, which formed on the NWs after exposure to oxygen plasma. Biotinylation was accomplished by reacting the APTES-functionalized NWs with sulfo-N-hydroxysuccinimide-biotin at slightly alkaline pH. It was determined that the biotinylated GaN NW surface was specific towards the binding of SA and demonstrated no affinity towards a control protein, bovine serum albumin (BSA). There was however, evidence of non-specific, electrostatic binding of both the SA protein and the BSA protein to the APTES-coated NWs, revealing the importance of the biotinylation step. Successful SA immobilization on the biotinylated GaN NW surface was verified using fluorescence microscopy, field-emission scanning electron microscopy, high-resolution transmission electron microscopy, atomic force microscopy, and x-ray photoelectron

spectroscopy. The functionalized GaN NWs demonstrate potential as biosensing platforms for the selective detection of proteins.

### **3.2: Introduction**

The detection of biological species in gases and in liquids is necessary for homeland security, medical diagnoses, environmental monitoring, as well as food safety [4], [29]. Current biosensing techniques do not meet the requirements of portable sensors for real-time monitoring. Consequently, there has been a shift to develop semiconductor thin film and nanowire based conductometric biosensors. These thin film/nanowire based biosensors can detect a biomolecule binding event through resistivity changes and have the advantages of a small footprint, a high sensitivity, and low power consumption [4], [15], [29], [66].

Gallium nitride (GaN) is an attractive semiconductor for such biosensors since it exhibits excellent transport properties, such as high electron mobility and saturation velocity, as well as biocompatibility, non-toxicity, and stability under physiological conditions [4], [13], [15]. GaN thin film high-electron-mobility transistors (HEMTs), or hetero-structure FETs, have proven ability to electrically detect proteins, antibodies, small molecules such as glucose, and strands of DNA with selectivity and high sensitivity [4], [15]. Compared to their thin film counterparts, GaN nanowire (NW) based devices can display an even higher relative resistance change upon exposure to analytes due to their high surface-to-volume ratio [4], [66]. In addition, several analyte specific nanowire sensors can be integrated on a single chip enabling a multiplexed mode of detection. GaN NW based chemical sensors have recently demonstrated a ppb level detection of

aromatics [66] and alcohols [67]–[69] in air. GaN NW based biosensors are also emerging [38], [39], as functionalization techniques for specific biomolecule attachment to GaN NWs are being developed [11], [27].

In this chapter, a 2-step, solution-based sequential layer functionalization method for streptavidin (SA) immobilization on GaN NWs for protein sensor applications is presented. This is an extension of the recently developed protocol for specific SA functionalization of silicon and silicon carbide NWs [70]. This approach performs all functionalization steps in solution thus enabling the assembly of multiple protein-specific NWs on a single biosensing platform. A variety of spectroscopic and microscopic techniques were utilized to verify each functionalization step on the NW surface.

### **3.3: Materials & Methods**

#### **3.3.1: Experimental Design for Protein Selective Sensing**

The streptavidin (SA) protein exhibits a strong, non-covalent interaction with its ligand biotin and hence biotinylated GaN NWs should enable the specific immobilization of SA. The biotin ligand itself, however, does not bind to the GaN surface and thus a linker molecule is necessary. 3-Aminopropyltriethoxysilane (APTES) is a small organic silane that has the ability to covalently attach to oxidized or hydroxylated surfaces as well as amine reactive biomolecules (i.e. modified forms of biotin) [14], [15], [70]. APTES is one of the most explored coupling agents in the functionalization of semiconductor materials, including GaN. The covalent attachment of APTES to GaN thin films has been well characterized and demonstrated as an initial step for the immobilization of biomolecules [13]–[15]. Kang et al. proved that APTES functionalization, followed by

biotinylation resulted in the electrical detection of the streptavidin protein on AlGaN/GaN thin film devices [15]. To date, no studies have been performed to functionalize the GaN NW surface with APTES nor its subsequent biotinylation and streptavidin immobilization. Consequently, the investigation of APTES functionalization, biotinylation, and streptavidin immobilization on GaN NWs for biosensing applications is as follows and employs a protocol in which all steps are performed in solution.

For the experiment as demonstrated in Figure 18, surface oxidized GaN NWs were exposed to APTES, followed by sulfo-N-hydroxysuccinimide-biotin, with each functionalization step studied by surface characterization techniques. The biotinylated NWs were then exposed to a SA solution, binding of which was confirmed using various methods. Control tests were also conducted to examine the specificity of the functionalized GaN NW surfaces towards SA. Bovine serum albumin (BSA) is a protein that has no affinity for biotin or biotinylated surfaces and hence was chosen as the control protein [15], [70]. The biotinylated GaN NWs were exposed to a mixture of SA and BSA, with each protein containing a different fluorophore. Fluorescence microscopy was then used to determine if the biotinylated NWs were indeed specific to only SA. The SA/BSA mixture was also exposed to the APTES-coated GaN NWs and the cleaned (oxidized) GaN NWs (see Figure 18) and studied using fluorescence microscopy to determine if these surfaces were prone to the non-specific adsorption of SA or BSA.

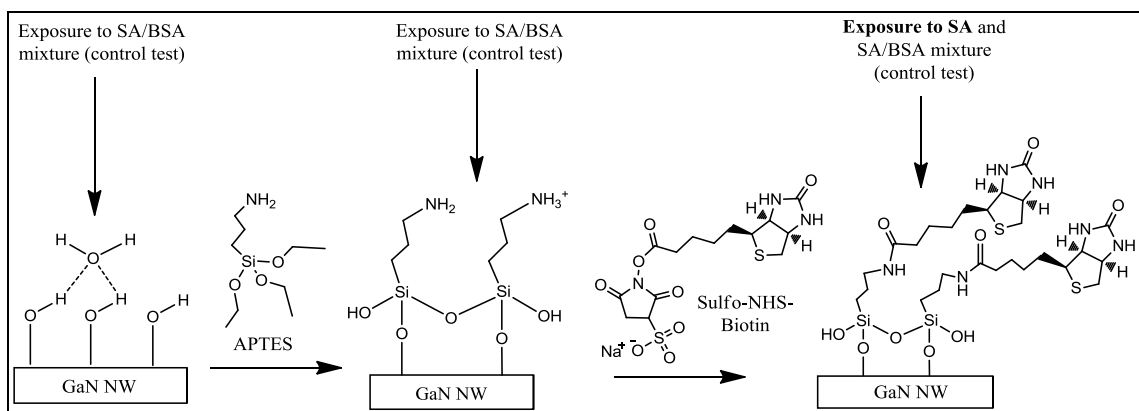


**Figure 18: Experimental reaction scheme.**

### 3.3.2: Nanowire Growth & Functionalization

GaN NWs were grown on Si(111) substrates by molecular beam epitaxy, via the catalyst-free vapor-solid growth mechanism, as described elsewhere [71]. The as-grown NWs on Si were oxygen plasma cleaned in a 20 % oxygen / 80 % argon gas mixture for 5 min and subsequently exposed to laboratory air. For field-emission scanning electron microscopy/energy dispersive x-ray spectroscopy (FESEM/EDXS) analyses, the cleaned NWs were mechanically scraped off the Si substrates and placed onto 1 cm × 1 cm Au-coated Si pieces. For high-resolution transmission electron microscopy/electron energy loss spectroscopy (HRTEM/EELS), the cleaned NWs were mechanically scraped off the substrates and placed onto standard 300 mesh lacey-carbon TEM grids. For fluorescence microscopy and x-ray photoelectron spectroscopy (XPS), the cleaned NWs were placed in a vial containing toluene and ultrasonically agitated to detach the NWs from the Si substrate and form a suspension. Drops of the suspended NWs in toluene were then placed onto 1 cm × 1 cm Si pieces (for fluorescence microscopy) and 1 cm × 1 cm Au-coated Si pieces (for XPS) and allowed to air dry.

APTES functionalization of the NWs was achieved by placing the cleaned NWs in a vial containing a 2 % APTES in toluene solution. The NWs in the APTES solution were ultrasonically agitated to detach the NWs from the Si substrates and form a suspension. After a 30 min exposure to the APTES solution, the NWs were sedimented by centrifugation for 2 min at 10,000 rpm (4 cm centrifuge rotor radius) and rinsed with toluene. The APTES-functionalized NWs were re-suspended in toluene with subsequent placement onto 1 cm × 1 cm Si pieces for FESEM/EDXS, XPS, and fluorescence microscopy, as well as TEM grids for HRTEM.

Biotinylation of the GaN NWs was achieved by adding 0.5 mL of sulfo-N-hydroxysuccinimide-biotin, at a concentration of 5 mg/mL in 0.01 mol/L phosphate buffer (pH= 7.4), to the vial containing the rinsed and sedimented, APTES-coated GaN NWs. The vial was sonicated to bring the NWs back into suspension followed by a 2 h exposure to the biotin solution. The biotinylated NW suspension was centrifuged, followed by the removal of residual biotin solution from the vial. After rinsing in phosphate buffer, drops of the biotinylated NW suspension were deposited onto Si pieces for FESEM, XPS, and fluorescence microscopy, as well as TEM grids for HRTEM, and allowed to dry.

### **3.3.3: Protein Immobilization**

The biotinylated NWs, adhered to the uncoated or Au-coated Si pieces and TEM grids (as described in 3.3.2: Nanowire Growth & Functionalization), were exposed to a 0.058 mg/mL streptavidin, labeled with cyanine-3, in 0.01 mol/L phosphate buffer (pH= 7.4) solution for 2 h, followed by a brief sonication, a rinse in buffer, and drying in a N<sub>2</sub>

flow. The SA immobilized NW samples were then analyzed using atomic force microscopy (AFM), FESEM, XPS, and HRTEM.

For the control experiments on the specificity of SA binding, the cleaned, the APTES-coated, and the biotinylated NWs (each adhered to Si pieces as described in 3.3.2: Nanowire Growth & Functionalization) were placed in a mixture of 0.058 mg/mL streptavidin, labeled with cyanine-3, and 0.058 mg/mL bovine serum albumin, labeled with fluorescein isothiocyanate, in 0.01 mol/L phosphate buffer (pH= 7.4) solution for 2 h, followed by a brief sonication, a rinse with buffer, and drying in a N<sub>2</sub> flow. Fluorescence microscopy was then utilized to study the binding of each protein (SA and BSA) to the cleaned, the APTES-coated, and the biotinylated GaN NWs.

#### **3.3.4: Characterization Methods**

The morphology, dimensions, and elemental composition of the cleaned, APTES-coated, biotinylated, and SA immobilized GaN NWs were characterized using a Hitachi-4700 FESEM equipped with an 80 mm<sup>2</sup> Oxford Instruments X-Max silicon drift EDX detector.

The NW morphology and microstructure, including thickness and composition of organic layers, were examined by an FEI Titan 80-300 HRTEM operated at a 300 kV accelerating voltage and equipped with S-TWIN objective lenses, Gatan's Enfina electron spectrometer, and an EDAX 30 mm<sup>2</sup> Si/Li EDX detector. Low intensity illumination conditions and beam blanking were used to minimize possible radiation damage of the organic layers.

The surface topography and morphology of the functionalized GaN NWs were investigated with a Veeco DI Dimension AFM on a  $1\ \mu\text{m} \times 2\ \mu\text{m}$  scale in tapping mode. Images were analyzed using WSxM v5.0 software [48].

For the XPS study, the cleaned and functionalized GaN NWs on Au-coated Si pieces were analyzed in a Kratos Analytical Axis Ultra DLD XPS instrument with a monochromated Al  $K\alpha$  X-ray source at 150 W (10 mA, 15 kV). X-rays were collected at a  $0^\circ$  angle from the surface normal on an area of  $300\ \mu\text{m} \times 700\ \mu\text{m}$ . It is estimated that there were about  $12,000 \pm 2,000$  nanowires in the  $300\ \mu\text{m} \times 700\ \mu\text{m}$  XPS beam area. The atomic percent of GaN NWs in the measurement area was roughly 10 %, significantly higher than the sensitivity of the XPS instrument (an atomic percent of 0.1 to 1 %), thus allowing for observable XPS signals from the NWs.

XPS low resolution survey scans (160 eV pass energy, 0.5 eV step size) and high resolution narrow scans (40 eV pass energy, 0.1 eV step size) of Au 4f, O 1s, N 1s, C 1s, Si 2p, and Ga  $2p_{3/2}$  were obtained. The binding energy scale was calibrated to the Au  $4f_{7/2}$  peak at 84.0 eV. Charge neutralization was not necessary during sample analysis due to the calibration to the Au  $4f_{7/2}$  peak.

Fluorescence microscopy was performed on the NWs using a Nikon Eclipse TE300 inverted epifluorescence microscope with a Plan Apo 60 x (N.A. 1.4) oil immersion objective. SA was imaged using a Nikon EF.4 filter cube with an excitation of 515 nm to 565 nm at a 1 s exposure time. BSA was imaged using a Nikon B-2E/C filter cube with an excitation of 465 nm to 495 nm at a 3 s exposure time; the longer exposure time of 3 s was necessary to enhance the weak fluorescence signal of BSA.

### 3.4: Results & Discussion

#### 3.4.1: APTES Functionalization, Biotinylation & Protein Immobilization

A cross-section FESEM image of the as-grown GaN NW batch is shown in Figure 19. The NW dimensions ranged from 8  $\mu\text{m}$  to 12  $\mu\text{m}$  in length and 70 nm to 300 nm in diameter. The NWs, with wurtzite crystal structure, were shaped as hexagonal prisms with six equivalent  $\{10\text{-}10\}$  side facets growing along the  $[0001]$  direction [71].

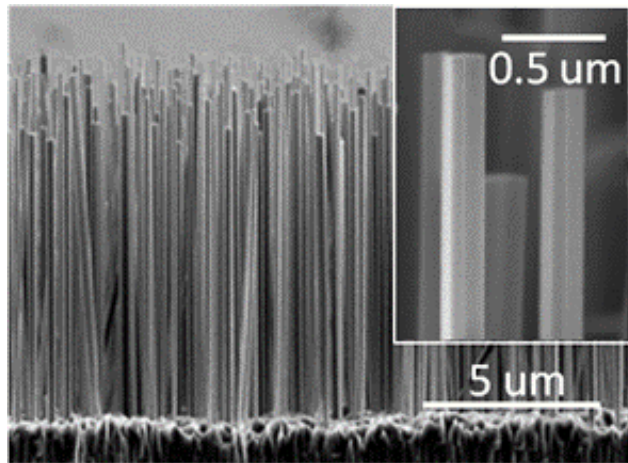
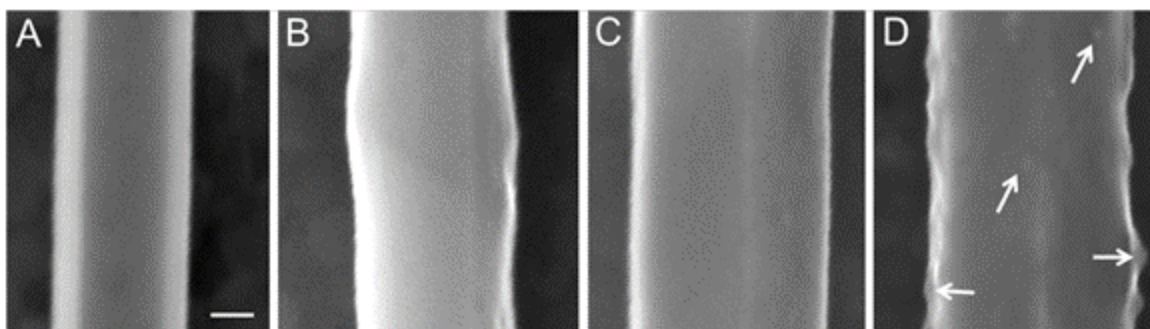
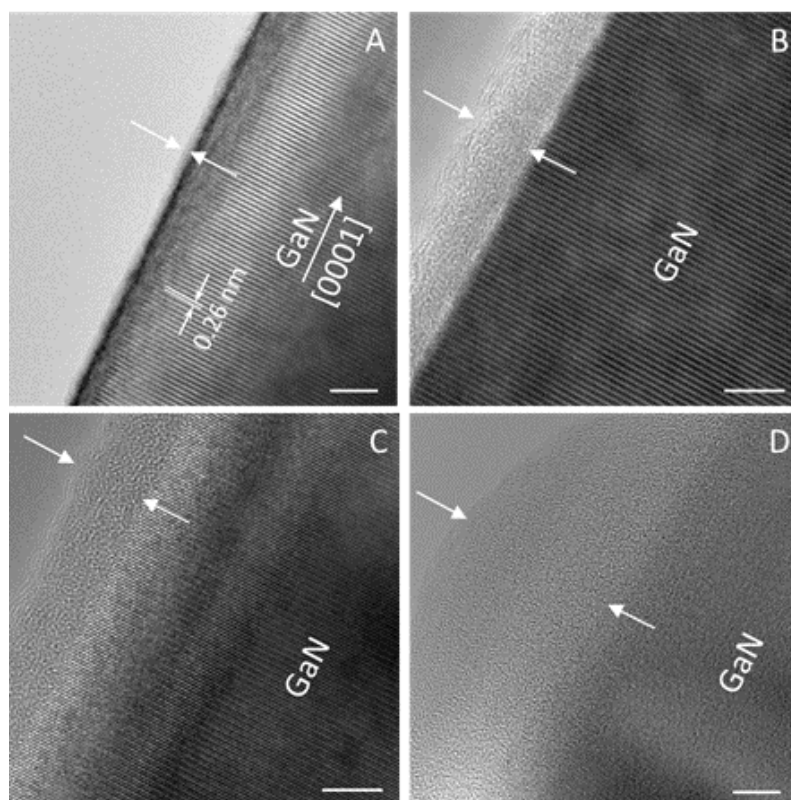


Figure 19: A cross-section FESEM image of GaN NWs grown on a Si(111) substrate. The magnified image in the inset shows hexagonal faceting of NW sidewalls.

A FESEM image of the faceted NW sidewalls after exposure to oxygen plasma is shown in Figure 20A. A corresponding HRTEM image (Figure 21A) shows an  $\approx 1$  nm thick oxide layer on the NW surface. It is likely that some of this oxide layer formed on the NW surface upon removal of the NWs from the growth chamber and subsequent interaction with air [72], [73].



**Figure 20:** FESEM images of the GaN NW sidewalls after: A) oxygen plasma cleaning, B) APTES functionalization, C) biotinylation, and D) SA immobilization. The hexagonal faceting of the clean NW in image A) gradually disappears upon the B), C), and D) functionalization steps as surface roughening increases. The arrows in D) point to hemispherical agglomerates, likely made of SA molecules. Note: the initial diameters of the NWs in A)-D) are not the same and therefore, the NW diameter in A) cannot be subtracted from the NW diameters in B)-D) to quantitatively determine organic layer thicknesses. The 50 nm scale bar in A) applies to all images.



**Figure 21:** HRTEM images of near edge regions of a GaN NW after: A) oxygen plasma cleaning, B) APTES functionalization, C) biotinylation, and D) SA immobilization. The 0.26 nm GaN lattice fringes, clearly evident

in A)-C), indicate the [0001] c-axis NW growth direction. Arrows point out the surface layers of: A) the native oxide, B) APTES, C) APTES/biotin, and D) APTES/biotin/SA. Note: with successive organic layer accumulation, the interface between the edge of the NW and the deposited organic layers, as well as the GaN lattice fringes, become barely visible. The scale bar in the right corner of each image is 5 nm.

However, to induce the formation of a thicker, denser oxide layer, which is necessary for further functionalization steps, oxygen plasma cleaning of the as-grown NWs was performed. The EELS analysis (see the 3.7: Supplementary Data section below) of the oxygen plasma cleaned GaN NWs revealed that the 1 nm oxide layer is composed of Ga, N, and O elements, thus implying that it is a partially oxidized GaN layer (made of gallium oxynitride or a mixture of residual gallium nitride with a newly formed gallium oxide, or both). More detail concerning the chemical composition and microstructure of the oxygen plasma cleaned GaN NWs is shown in the 3.7: Supplementary Data section using HRTEM/EELS.

APTES functionalization of the cleaned NW surfaces produced an  $\approx 5$  nm thick amorphous coating as seen in Figure 21B (also, see 3.7: Supplementary Data for an EDXS analysis of the chemical composition of this layer). A follow up biotinylation step is shown in Figure 20C (FESEM) and Figure 21C (HRTEM); the combined biotin/APTES layer is also amorphous and slightly thicker than the APTES layer with some local thickness variations. The final step of SA conjugation to the biotinylated NW surface caused the thickness of the organic layer to increase to 15 nm to 20 nm as shown in the HRTEM image in Figure 21D. The FESEM image in Figure 20D also shows that the SA immobilized NW surface is covered with small hemispherical agglomerates that

are likely composed of SA molecules (see the 3.7: Supplementary Data for a dimensional analysis of the agglomerates using AFM).

Successive deposition of the APTES, biotin, and SA layers on the NW surface was validated using an XPS analysis. The N 1s, Ga 2p<sub>3/2</sub>, and Si 2p narrow scans for the oxygen plasma cleaned NWs are shown as spectra (1) in Figure 22A, B, and C, respectively. In Figure 22A (spectrum 1), a N 1s signal is centered around 398.5 eV and corresponds to N atoms bound to Ga in GaN [74]. In Figure 22B (spectrum 1), a Ga 2p<sub>3/2</sub> signal appears at 1119 eV, indicative of Ga atoms bound to O and/or Ga atoms bound to N, i.e. Ga\*-O and/or Ga\*-N [74], [75]. The XPS results agree with the EELS analysis suggesting that the surface oxide is a thin, partially oxidized GaN layer made of gallium oxynitride or a mixture of residual gallium nitride with a newly formed gallium oxide, or both. The Si 2p spectrum of the cleaned GaN NWs demonstrates no Si signal as would be expected. The cleaned GaN NWs also demonstrate clear C 1s and O 1s peaks (spectra not shown). However, because the NWs were moderately dispersed on the substrate, the C 1s and O 1s peaks were complicated by carbon and oxygen present on the Au-coated surface.

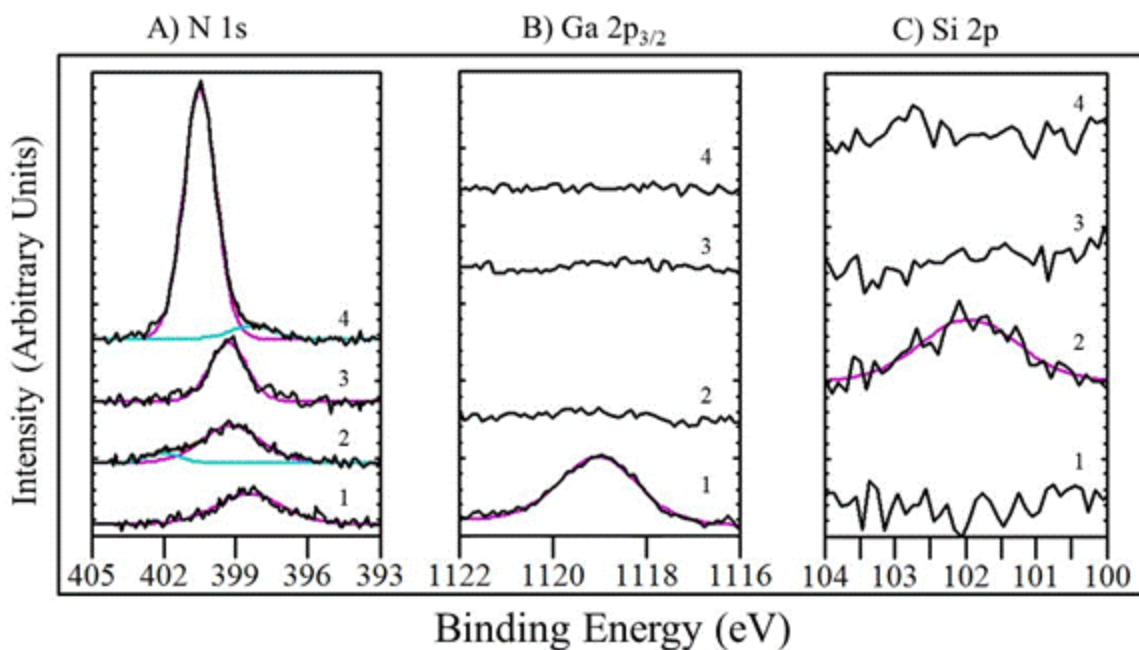


Figure 22: XPS narrow scans: A) N 1s scan, B) Ga 2p<sub>3/2</sub> scan, and C) Si 2p scan. For all three scans, (1) is the oxygen plasma cleaned NWs, (2) is the APTES-coated NWs, (3) is the biotinylated NWs, and (4) is the SA immobilized NWs.

Upon APTES functionalization, there is the appearance of a Si 2p peak (see spectrum 2, Figure 22C) which was absent on the cleaned NWs (spectrum 1). The Ga 2p<sub>3/2</sub> peak on the cleaned NWs (spectrum 1, Figure 22B) has disappeared following APTES functionalization (spectrum 2, Figure 22B) indicating that the NWs have been fully coated with APTES. The fact that a Ga peak is not seen with XPS signifies that the APTES layer thickness must be  $\geq 5$  nm, which is in agreement with the measured thickness of APTES using HRTEM. The absence of a Ga 2p<sub>3/2</sub> peak and presence of a Si 2p peak suggests that the N 1s peak of the APTES-coated NWs (spectrum 2, Figure 22A) results from the amino group of APTES. The N 1s peak of the APTES-coated NWs appears at 399 eV with a shoulder at 402 eV. The peak at 399 eV is the NH<sub>2</sub> form of the

amino group and the peak at 402 eV is the  $\text{NH}_3^+$  or hydrogen bonded  $\text{NH}_2$  form of the amino group that is present in APTES [14], [70]. Feasibility of both forms of the APTES amino group to co-existent is schematically shown in Figure 18 (see the APTES coating step).

The Si 2p peak that was present following APTES functionalization (spectrum 2, Figure 22C) has disappeared post biotinylation (spectrum 3, Figure 22C). In addition there is no Ga 2p<sub>3/2</sub> peak (spectrum 3, Figure 22B). The biotinylated NWs do display a N 1s peak (spectrum 3, Figure 22A) at 399 eV. Since there is neither Si nor Ga present for the biotinylated NWs, the N 1s signal must be fully attributed to the NH amino groups contained within the ureido ring of biotin (see Figure 18). The XPS data suggests the APTES-functionalized NWs must be fully coated with biotin molecules.

The SA immobilized NWs displayed neither a Ga 2p<sub>3/2</sub> peak (spectrum 4, Figure 22B) nor a Si 2p peak (spectrum 4, Figure 22C). There was however, a very strong N 1s peak at 400 eV with a shoulder at 398 eV. These N 1s peaks are consistent with typical protein N 1s binding energies [76]. In addition, the C 1s spectrum for the SA immobilized NWs (not shown) demonstrated very strong C\*-O, C\*-N, and C\*=O components that were substantially more pronounced than in the case of the cleaned, APTES-coated, and biotinylated NWs that were dominated by carbon from the underlying Au substrate.

It should be noted that the functionalization of the NWs, including SA binding, was repeated many times to ensure reproducibility of the solution-based functionalization

technique and the results discussed above were observed in the numerous functionalization trials conducted.

### **3.4.2: Control (Specificity) Tests**

To further confirm SA binding, and to prove specificity towards the SA protein, the biotinylated NWs were exposed to a mixture of red-fluorescent SA and green-fluorescent BSA and then analyzed using fluorescence microscopy. Figure 23A demonstrates the fluorescence microscopy image of a biotinylated NW after exposure to the SA/BSA mixture. The bright red fluorescing NW in image A confirms the presence of SA. Figure 23B demonstrates the fluorescence microscopy image of the same NW imaged in A, but under a different fluorescence filter cube. Since there is no detectable green fluorescing NW in image B (a white, dashed oval marks the location of the NW), it can be concluded that BSA did not bind to the biotinylated NWs, demonstrating specificity of the biotinylated GaN NWs towards the SA protein.

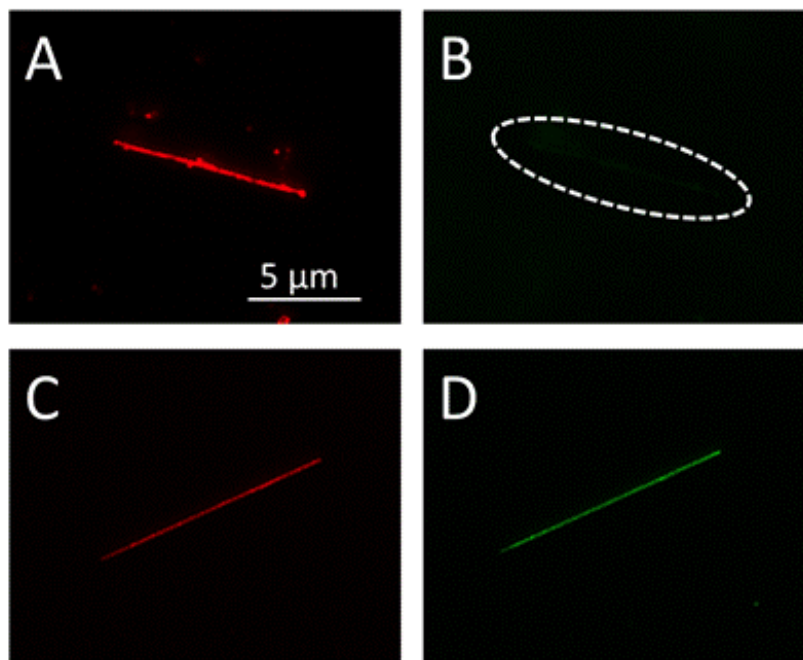


**Figure 23:** A) and B): a biotinylated GaN NW after exposure to the SA/BSA mixture under the EF.4 fluorescence filter cube for SA detection (A), and the B-2E/C fluorescence filter cube for BSA detection (B). Note: the dashed line oval in image B) marks the location of the non-fluorescing NW. C) and D): an APTES-coated GaN NW after exposure to the SA/BSA mixture under the EF.4 fluorescence filter cube for SA detection (C), and the B-2E/C fluorescence filter cube for BSA detection (D). Note: images A) and C) were taken with a 1 s exposure time, while B) and D) with a 3 s exposure time. The 5  $\mu\text{m}$  scale bar in A) applies to all images.

Additional control tests were performed to determine if there was any non-specific binding of the SA and BSA proteins to the cleaned and APTES-coated GaN NWs. The cleaned GaN NWs were exposed to a mixture of SA/BSA and then analyzed using fluorescence microscopy. There was neither red (from SA) nor green (from BSA) fluorescence detected under the respective fluorescence filter cubes (images not shown). Consequently, there was little, if any, non-specific attachment of the SA and the BSA proteins to the cleaned NW surface. This may be attributed to the fact that the native oxide on the GaN NW surface, existence of which was proven using HRTEM, EELS, and EDXS, likely carries some negative charge in the form of  $\text{O}^-$  and  $\text{HO}^-$  species. The surface

negative charge repels the SA and BSA proteins which are also negatively charged at the working pH of 7.4 [18], [64]. On the other hand, APTES-coated GaN NWs exposed to the SA/BSA mixture demonstrated both red fluorescence from SA and green fluorescence from BSA. Figure 23C shows a red fluorescing APTES-coated GaN NW after exposure to the SA/BSA mixture and Figure 23D shows the same NW fluorescing green under a different filter cube. Therefore, there was non-specific attachment of both SA and BSA to the APTES-coated GaN NWs. This non-specific attachment of both proteins could be explained by the fact that the terminal amino group of APTES can exist in a positively charged, protonated state (as schematically shown in Figure 18 and confirmed with XPS in Figure 22) [11], [65]. The SA and BSA proteins, both of which are negatively charged at the working pH, are likely electrostatically bound to the APTES-coated GaN NWs resulting in non-specific attachment [65]. Notably, comparing Figure 23A and Figure 23C, the specifically bound SA on the biotinylated NWs is significantly more fluorescent than the non-specifically bound SA on the APTES-only coated NWs. Therefore, there are likely a greater number of specifically bound SA molecules on the biotinylated NWs as compared to the APTES-coated NWs. Nonetheless, the fact that there was a detectable amount of both proteins on the APTES-coated NWs reveals the importance of the biotinylation step in order to inhibit non-specific SA/BSA binding and to result in specific SA binding only.

### **3.5: Conclusions**

A solution-based functionalization method for SA immobilization on GaN NWs was presented for potential protein sensor applications. The protocol included the initial

formation of an oxide layer on the as-grown NWs, which was facilitated by oxygen plasma cleaning followed by exposure to laboratory air. Specifically, the oxide layer on the NWs was estimated to be about 1 nm thick by HRTEM. Following surface oxidation, the next step of the protocol was achieved by reacting the oxidized NW surfaces with APTES, which led to formation of an  $\approx 5$  nm thick amine terminated APTES layer. The final step of the protocol for enabling SA immobilization employed the biotinylation of the APTES-coated NWs through reaction with an amine-reactive molecule, sulfo-N-hydroxysuccinimide-biotin. SA immobilization on the biotinylated GaN NWs was achieved and was demonstrated by FESEM, AFM, XPS, HRTEM, and fluorescence microscopy. Using these techniques, on average, a 15 nm to 20 nm thick organic layer, consisting of APTES, biotin, and SA, was present on the NW surface. A fluorescence microscopy analysis of the biotinylated NWs further proved SA binding. It also confirmed that SA binding was specific; the biotinylated surfaces demonstrated no affinity towards BSA, a control protein. On the other hand, the APTES-coated NWs demonstrated non-specific (likely electrostatic in nature) binding of both SA and BSA, revealing the importance of the biotinylation step in order to limit non-specific protein binding.

This study has demonstrated that GaN NWs are suitable for protein sensing and for biosensing applications in general. By employing this solution-based functionalization technique with other chemistries, the multiplexed detection of a wide range of biomolecules would be possible on a single biosensing chip.

### **3.6: Acknowledgements**

The authors are appreciative of the helpful discussions with Dr. Rebecca A. Zangmeister (Material Measurement Laboratory, NIST). EHW, MVR, and JAS gratefully acknowledge the financial support of the National Science Foundation (Grant # ECCS-0901712). VPO gratefully acknowledges the financial support from NIST under contracts SB134110SE0579 and SB134111SE0814 and the MML12-1053-N00 Grant, award #0633478. AKM was supported by a contractual appointment to the U.S. Army Research Laboratory Postdoctoral Fellowship Program administered by Oak Ridge Associated Universities.

### **3.7: Supplementary Data**

#### **3.7.1: HRTEM & EELS Analysis of the GaN Surface Oxide**

The oxygen plasma cleaned GaN NWs were analyzed using HRTEM and EELS as demonstrated in Figure 24. The top left picture shows a HRTEM image of a NW edge with an amorphous-like outer layer with a thickness of  $\approx 1$  nm (indicated by arrows). The EELS analysis (Figure 24, spectrum ② on the right) determined that this layer is composed of Ga, N, and O elements, thus implying that it is a partially oxidized GaN layer (made of gallium oxynitride or a mixture of residual gallium nitride with a newly formed gallium oxide, or both). This surface layer was likely produced by reacting the nanowire surface with oxygen plasma and subsequent exposure to air [15], [74], [77].

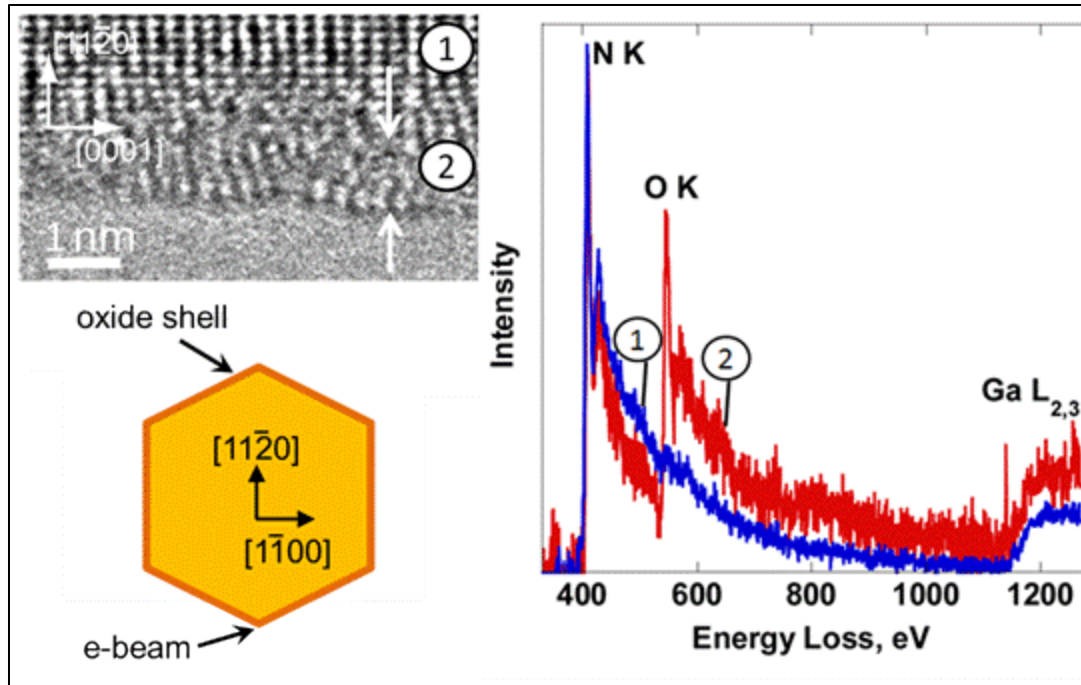


Figure 24: *Top left image*: a HRTEM image of a GaN NW edge. Region ① marks the NW interior and region ② is an amorphous-like surface oxide about 1 nm thick (marked with two vertical arrows). The [0001] growth direction of the NW is indicated. *Bottom left picture*: a schematic view of the imaging geometry of the NW. *Right spectra*: representative EELS spectra of the NW interior ① (blue spectrum) and surface oxide ② (red spectrum). The Ga/N ratio in region ② (not shown) is lower than its stoichiometric value in the NW interior, which is consistent with the formation of a gallium oxide/oxy-nitride surface layer.

It is important to point out that as the NW surface further interacts with air, some hydroxyl groups are formed through the reaction of the surface oxide with water vapor [14], [17]. This oxidized and partially hydroxylated NW surface is necessary for the covalent attachment of APTES to the NW. APTES hydrolysis and condensation reactions must occur with the hydroxyl groups on the NW surface for successful APTES functionalization [13]–[15].

### 3.7.2: Analysis of the Oxygen Plasma Cleaned and APTES-coated GaN NWs Using FESEM/EDX

The EDX spectrum of a cleaned GaN NW deposited on an Au-coated Si substrate is shown in Figure 25 (red spectrum). The spectrum reveals the typical N and Ga peaks

from GaN as well as an Au peak from the underlying substrate. A small carbon signal on the left shoulder of the N peak is attributed to unavoidable hydrocarbon contamination. A small oxygen signal on the right shoulder of the N peak is attributed to the surface oxide on the NW.

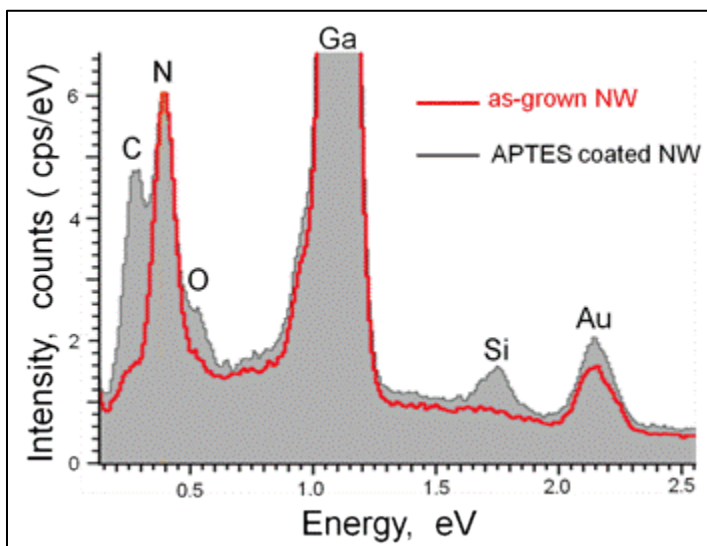


**Figure 25: EDX spectrum of a cleaned GaN NW before (red spectrum) and after (gray-shaded spectrum) APTES functionalization. The appearance of a Si peak and an increase in C and O peak intensity indicate successful binding of APTES molecules to the NW surface. Note: The Au signal arises from the underlying Au-coated substrate.**

EDX of the APTES-coated NWs is shown in Figure 25 as the gray-shaded spectrum. Compared to the data for cleaned GaN NW sample, a Si peak emerges and the C and O peaks intensify. This is consistent with the expected coating of the NW surface with APTES, which contains carbon, oxygen, and silicon.

### 3.7.3: AFM Analysis of Agglomerates on the SA Conjugated GaN NW Surface

To further characterize agglomerates that sparingly appeared on the NW surface after the final SA conjugation step (indicated by arrows in Figure 20D above), which were likely a product of aggregated protein molecules; their dimensions were analyzed with AFM. The inset in Figure 26 shows the profile for a typical agglomerated cluster measuring  $\approx 100$  nm in the lateral and  $\approx 16$  nm in the vertical directions. The heights of similar agglomerates rarely exceeded 20 nm.

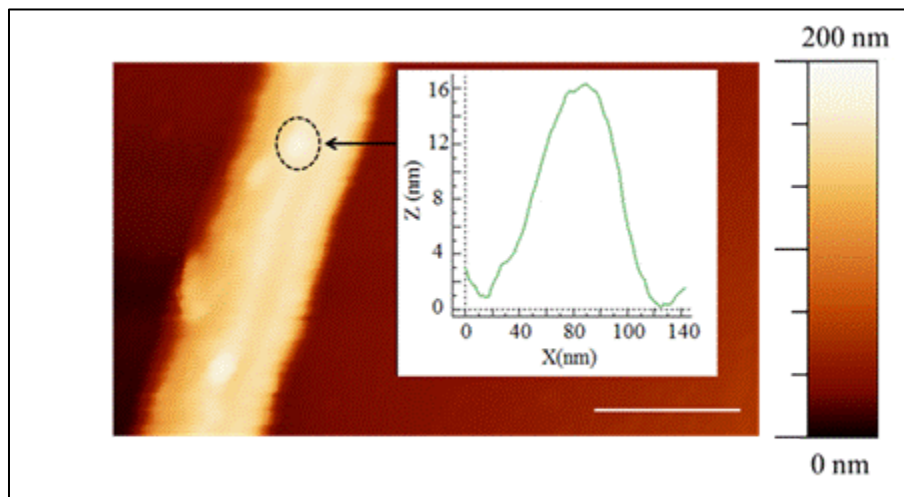


Figure 26: An AFM image of a SA immobilized GaN NW. The vertical bar on the right is the 200 nm color coded Z-scale and the horizontal bar in the lower right corner is the 400 nm X-scale. The inset shows a line scan across a typical protein agglomerate taken along the NW growth axis.

## **4: LIPID ENCAPSULATED SILICON NANOWIRE DEVICES- A NOVEL DETECTION METHOD FOR PROBING BACTERIAL CELL MEMBRANE MECHANISMS AND INTERACTIONS**

### **4.1: Abstract**

Silicon (Si) nanowire (NW) FET type devices were fabricated to electrically probe the formation and destruction of lipid bilayers on Si NWs in real-time. Spontaneous formation of a lipid bilayer around Si NW devices was found to occur when the devices were exposed to 50 nm liposomes consisting of phosphatidylcholine (PC) and phosphatidylglycerol (PG), the lipids present in an *E. coli* cell membrane. Bilayer formation on the Si NWs was detected by real-time electrical resistivity changes as well as by confocal fluorescence microscopy. The formation of the lipid bilayer on the NWs resulted in a 1-2 % decrease in device current, likely due to the charge of the lipids acting as a negative gate on the NW surface. The decrease in NW current could also be attributed to the bilayer shielding the NWs from the external solution. A detergent, Tween20, was found to remove the lipid bilayer from the NW surface very quickly (under ~ 2 min), resulting in a return of NW conductance to its original baseline value. The studies presented demonstrate that 1) a lipid layer mimicking an *E. coli* cell membrane can be formed on Si NW devices and 2) the in-situ electrical detection of *E. coli* cell membrane formation and destruction on Si NW devices can be achieved. The *E. coli* cell membrane encapsulated Si NW devices demonstrate a novel platform to electrically probe bacterial cell membrane mechanisms and interactions.

## 4.2: Introduction

Over the past decade, silicon (Si) nanowires (NWs) have been studied extensively as sensing platforms for the electrical detection of biomolecules [1], [6], [8], [9], [29]–[31]. The rapid, sensitive, selective, and label-free electrical recognition of small strands of DNA, enzymes, antibodies, antigens, even single virus molecules, all in real-time, have been achieved using Si NW based devices [1], [6], [8], [9], [29]–[31]. The profound abilities of Si NW based devices can be attributed to the following: the Si NW can be utilized to produce a FET type device in which biological compounds act as a gate on the NW surface leading to an increase or decrease in conductance in the NW, i.e. a direct electrical signal upon interaction of a biomolecule with the NW surface [1], [2], [6], [29]. Due to the high-surface-to-volume ratio of the nanostructured sensing element (the Si NW) of the device, extremely low limits of detection, or very high sensitivity, can be achieved in sensing analytes [9], [30], [31]. Well-developed functionalization protocols for bio-immobilization on Si substrates have been reproduced on Si NWs thus permitting the ability to selectively bind molecules of interest to the Si NW device surface [9], [29]. In addition, the dimensions of NWs are comparable to that of biological compounds and are thus ideal for biosensing [1], [6], [9]. These advantages of Si NW based devices have caused them to gain significant attention, and research with Si NW devices has already contributed to the advancement of medicine and the life sciences [1], [2], [6], [8], [9], [29]–[31].

The success of Si NW devices in the detection of biological compounds has opened up the possibility of using these nanostructured sensors to probe cellular mechanisms and interactions [30], [33], [34]. A large portion of cell reactions, however,

involve the cell membrane itself or proteins or ion channels embedded within the cell membrane [33]–[35]. As a consequence, studies have recently been carried out to encapsulate Si NW devices in a lipid bilayer as to mimic a cellular membrane in which the Si NW serves as the cell interior [33]–[37]. The studies conducted in [33] and [35] reveal the potential of lipid encapsulated Si NWs as a platform to probe cellular mechanisms and interactions, particularly cell membrane interactions [33], [34].

While the in-situ formation of lipid bilayers on Si NWs was studied using fluorescence microscopy by Römhildt *et al.* [37], no electrical measurements were performed to analyze how membrane formation on the NW affected its conductivity. Electrical signals for a bare Si NW device and a bilayer coated NW device were demonstrated in [33] and [35], however these measurements were not performed during bilayer formation on the NW surface (one cannot pin-point the time of bilayer formation). In addition, the purpose of the studies conducted in [33], [35] focused on embedding ion channels within the bilayer on the Si NW surface and whether ion flux could be measured through the channels using the NW devices. In contrast, for our experiments, we sought out to electrically detect lipid bilayer formation and destruction on Si NW devices in real-time and using confocal fluorescence microscopy for the purposes of exploring bacterial cell membrane mechanisms and interactions. In our studies, the lipids utilized were in a defined ratio to mimic an *E. coli* cell membrane [78]. After demonstrating the real-time electrical detection of an *E. coli* like lipid bilayer on Si NWs, we probed the destruction of the lipid bilayer on the Si NW devices using a detergent (Tween20). The destruction of the bilayer was detected with both real-time electrical measurements and confocal

fluorescence microscopy. The results demonstrate that a lipid layer mimicking an *E. coli* cell membrane can be formed on Si NW devices and the in-situ electrical detection of membrane formation and destruction on Si NW devices can be achieved. The bacterial cell membrane encapsulated Si NW devices demonstrate a novel platform to electrically probe bacterial cell membrane mechanisms and interactions, i.e. the interaction of bacterial cell membranes with antimicrobial and antibiotic molecules.

### **4.3: Materials & Methods**

#### **4.3.1: Device Design**

The Si NW sensor chip design is demonstrated in Figure 27A. The chip design includes twelve  $1 \times 1 \text{ mm}^2$  metal pads (at the top of the sensor chip) that serve as the contacts to a semiconductor parameter analyzer system. The twelve metal pads extend as  $20 \text{ }\mu\text{m}$  wide lines to the center of the chip, where they pair at a  $10 \text{ }\mu\text{m}$  gap. As shown in Figure 27B, a single Si NW is positioned between each gap resulting in a total of 6 NW devices on the sensor chip. A  $5 \text{ }\mu\text{m}$  wide,  $6 \text{ mm}$  long fluid channel encompasses all 6 NWs and flows into a fluid reservoir at the bottom of the chip (see Figure 27A and Figure 27B). The sensor chip dimensions are  $1 \times 1 \text{ in}^2$ .

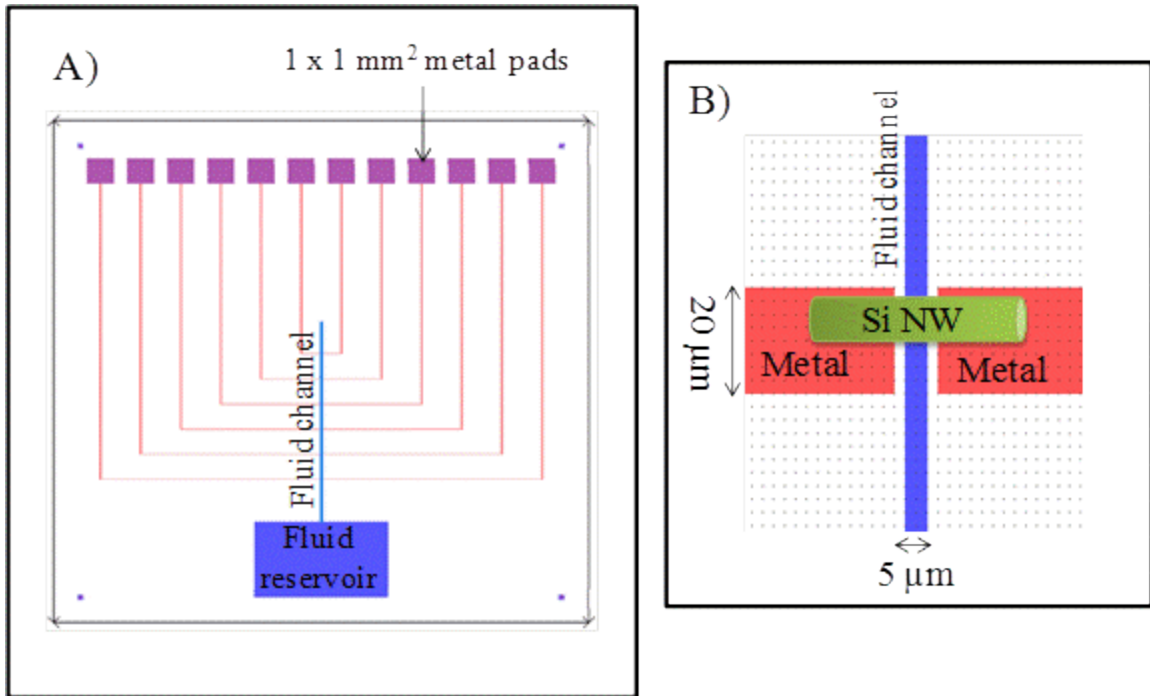


**Figure 27: The Si NW sensor chip. A: The overall design of the sensor chip. The chip contains 6 NW devices, a fluid channel, and a fluid reservoir. B: A schematic of an enlarged region of one of the 6 NW devices on the sensor chip.**

The Si NW sensor chip design was incorporated into two photolithography masks for device fabrication. The first mask contained the twelve  $1 \times 1 \text{ mm}^2$  metal pads and their extensions as lines to the center of the chip. The second mask contained the twelve  $1 \times 1 \text{ mm}^2$  metal pads, the fluid channel, and fluid reservoir.

#### 4.3.2: Device Fabrication

A four inch  $\langle 100 \rangle$  Si wafer, coated with a 300 nm  $\text{SiO}_2$  layer (see Figure 28, A1), was utilized as the substrate for device fabrication. The  $\text{SiO}_2$  coated Si wafer was diced into one inch by one inch sample pieces. The sample pieces were cleaned using acetone and isopropanol, rinsed in distilled water, and then dried using a stream of nitrogen. The clean  $\text{SiO}_2/\text{Si}$  sample pieces were subjected to standard photolithography processing steps

using the first mask described in 4.3.1: Device Design, in order to define the openings for the bottom metal contacts (see Figure 28, A2).

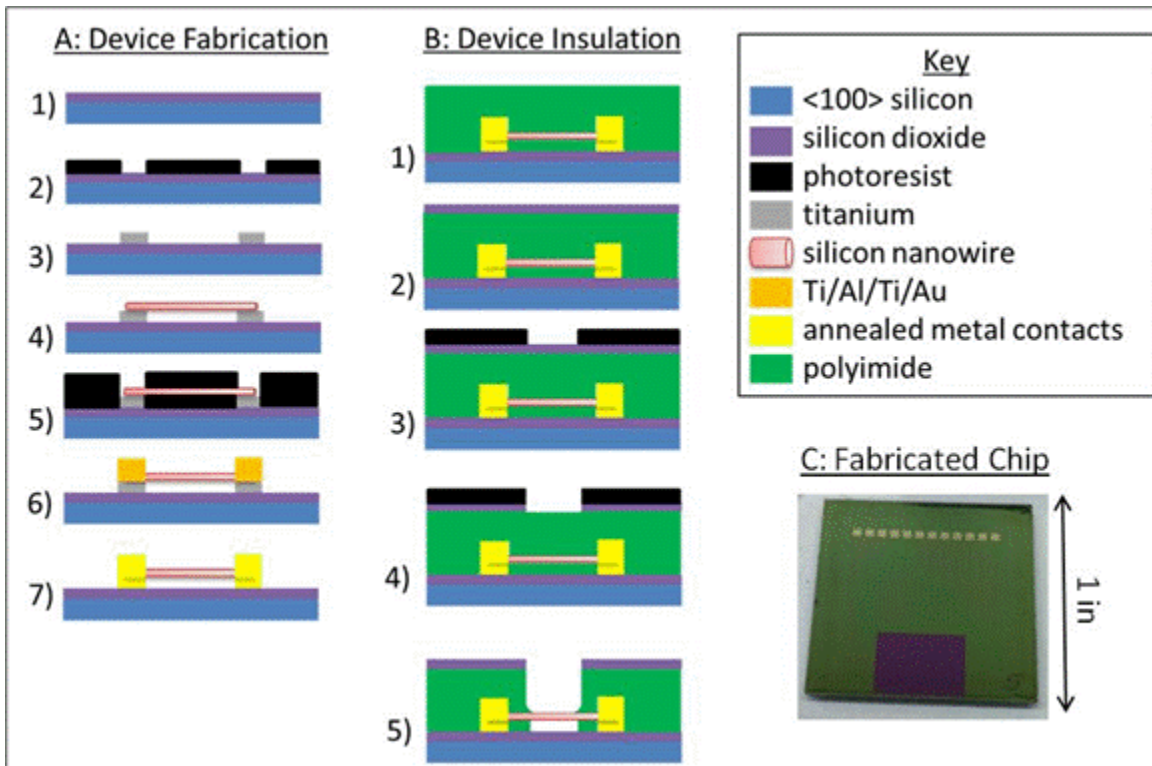


Figure 28: Schematic of the silicon nanowire two-terminal sensor chip fabrication and insulation. A: shows the steps for sensor chip fabrication, B: shows the steps for sensor chip insulation, and C: is an image of a fabricated and insulated sensor chip.

Electron beam deposition was used to deposit 15 nm of Ti metal onto the patterned SiO<sub>2</sub>/Si pieces and the remaining photoresist on the substrate was removed using a standard lift-off recipe (see Figure 28, A3). N-type Si NWs, with a length of about 30 μm and a diameter of 120 nm, grown using catalyst assisted vapor-liquid-solid chemical vapor deposition [45], were dielectrophoretically aligned onto the Ti contacts (see Figure 28, A4). Dielectrophoretic alignment of the nanowires onto the metal contacts

was carried out at 20 V to 30 V and at 1 kHz. Photolithography processing steps were again utilized with the first mask described in 4.3.1: Device Design, this time to define openings for the top metal contacts (see Figure 28, A5). Electron beam deposition was used to deposit the top metal contacts (70 nm of Ti, 70 nm of Al, 50 nm of Ti, and 50 nm of Au) and the remaining photoresist on the substrate was removed using a standard lift-off recipe (see Figure 28, A6). The completed devices were then annealed at 550°C for 30 seconds to facilitate ohmic contact formation (Figure 28, A7).

#### **4.3.3: Device Insulation**

To insulate the silicon nanowire two-terminal devices for the application of fluids, approximately 3  $\mu\text{m}$  of polyimide (PI) was spun onto the surface of the sensor chip (see Figure 28, B1). Following a baking and curing of the polyimide, 100 nm of  $\text{SiO}_2$  was deposited on top of the polyimide using plasma enhanced chemical vapor deposition (see Figure 28, B2). Standard photolithography processing steps were utilized with the second mask described in 4.3.1: Device Design, to define a 5  $\mu\text{m}$  wide channel that would allow for the flow of liquids over the center of the Si NW (see Figure 28, B3). A  $\text{CHF}_3/\text{O}_2$  plasma etch was used to etch through the deposited oxide layer (see Figure 28, B4). Then, an  $\text{O}_2$  plasma etch was used to etch through the polyimide and to remove the top photoresist layer (Figure 28, B5) An image of a fabricated and insulated sensor chip is shown in Figure 28C.

#### **4.3.4: Preparation of Liposomes & Tween20**

Small unilamellar vesicles (SUVs) were prepared using DOPC (1,2-dioleoyl-sn-glycero-3-phosphocholine, 5 mg/mL in chloroform, Avanti Polar Lipids), DOPG (1,2-

dioleoyl-sn-glycero-3-[phospho-rac-(1-glycerol)] (sodium salt), 1 mg/mL in chloroform, Avanti Polar Lipids), and NBD-PG (1-oleoyl-2-{6-[(7-nitro-2-1,3-benzoxadiazol-4-yl)amino]hexanoyl}-sn-glycerol-3-[phospho-rac-(1-glycerol)] (ammonium salt), 1 mg/mL in chloroform, Avanti Polar Lipids). 80 % DOPC, 18 % DOPG, and 2 % NBD-PG (mole percent) were added to a round bottom flask using gas tight syringes. The solution was rotor-evaporated with a nitrogen gas flow followed by vacuum drying to evaporate all of the chloroform solvent. The lipids were resuspended in phosphate buffer, 0.01 M, pH = 7.4, to give a final lipid concentration of 2.5 mg/mL. The lipid solution was rotor-evaporated without gas flow to ensure complete resuspension of the lipids in the buffer. The lipid solution was extruded through an Avanti Mini Extruder, using a 50 nm polycarbonate filter, for 10 total pass throughs to give 50 nm liposomes suspended in buffer [78]. Following 24 h from liposome preparation, liposome solutions were sonicated for 30 min to ensure SUVs.

The common biological detergent, Tween20 (polyethylene glycol sorbitan monolaurate, viscous liquid, Sigma-Aldrich), was dissolved in phosphate buffer (0.01 M, pH = 7.4) to give a 10 % by volume solution.

#### **4.3.5: Device Testing**

The 1 x 1 mm<sup>2</sup> metal pads (at the top of the sensor chip) were connected to a two-probe Agilent Semiconductor Parameter Analyzer system. For current versus voltage measurements, the devices were swept across 5 V to -5 V and resulting NW device current values were obtained. For current versus time measurements, a constant voltage of 500 mV was applied to the device and current values were obtained every second. 10-

100  $\mu$ L drops of phosphate buffer (0.01 M, pH = 7.4), liposome solution, and 10 % Tween20 were applied to the fluid channel of the Si NW sensor chip using a pipette and the current of the NW as a function of time was monitored.

#### **4.3.6: Optical & Fluorescence Microscopy**

Optical microscopy was performed on the Si NW sensor chips using an upright Olympus Optical Microscope. Images of the NW devices were obtained using a 50 x or 100 x objective in bright or dark field mode. Fluorescence microscopy was performed on the Si NW sensor chips using a Leica Microsystems Confocal Microscope. Images were obtained using a 40 x water immersion objective. The power of the laser was set at 23 % at an excitation wavelength of 458 nm and at an emission wavelength range of 500 nm to 600 nm, using a double dichoric (DD) 458/514 filter.

### **4.4: Results & Discussion**

#### **4.4.1: Characterization of the Si NW Devices**

The current versus voltage curves for a Si NW device on a fabricated sensor chip are demonstrated in Figure 29, left graph. Before the sensor chip annealing step (curve with blue diamonds), the devices displayed a semi-S-shaped curved with  $\mu$ A current values. Due to the non-linearity of the curve, it is clear that there was little ohmic contact formation between the NW and the metal contacts at this point in device fabrication. Following the annealing step of the sensor chip, the devices demonstrated a linear I-V curve with much higher  $\mu$ A current values (curve with the red squares). The linearity of the current vs. voltage curve reveals that annealing produced ohmic contacts between the NW and the metal contacts. Following the polyimide insulation layer of the sensor chip,

the Si NW devices retained ohmic behavior with slightly decreased  $\mu\text{A}$  current values (green triangles).

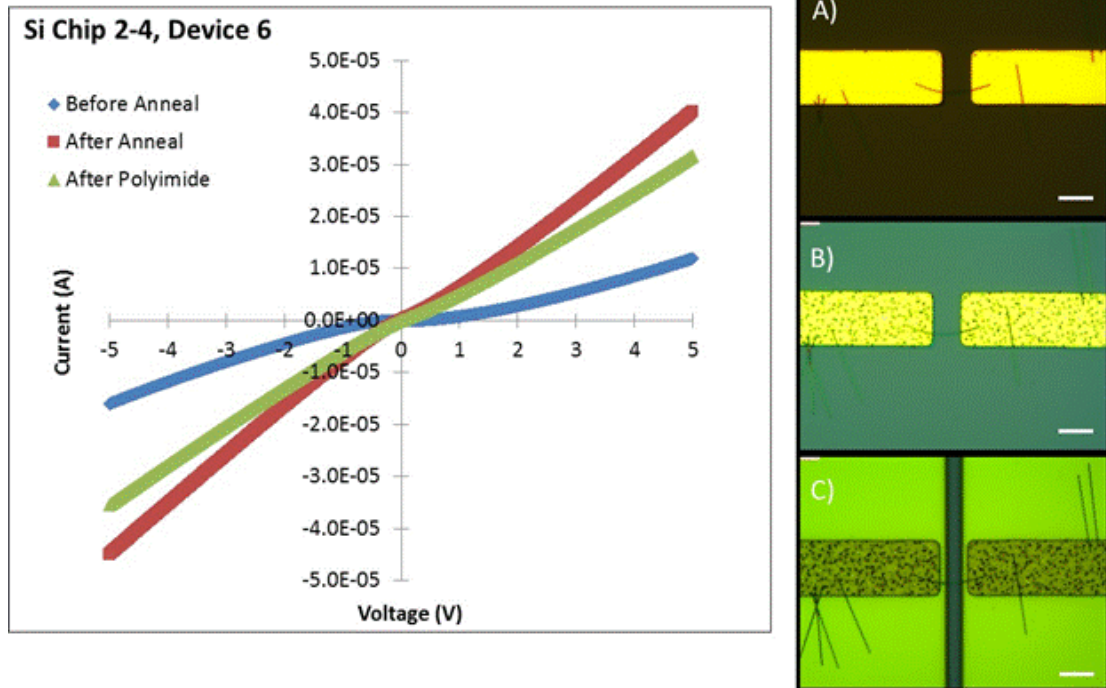


**Figure 29:** Left graph: current (A) versus voltage (V) curves for a Si NW device before anneal (blue diamonds), after anneal (red squares), and after PI insulation (green triangles). Right images are 50 x optical microscopy images of a Si NW device: A) before anneal, B) after anneal, and C) after polyimide insulation. The scale bar in all three images is 10  $\mu\text{m}$ .

Optical microscopy images, at a 50 x magnification, of a Si NW device before the annealing step (A), after the annealing step (B), and following polyimide insulation (C) are shown in Figure 29, right images. Before the annealing step (Figure 29A), a curved Si NW is seen bridging the gap between two smooth metal contacts. Following the annealing step (Figure 29B), circular features appeared on the metal contacts, likely due to the formation of metallic alloys, and the NW remained as the bridge between the

roughened contacts. After the polyimide insulation step (Figure 29C), the NW remains bridging the metal contacts and an open 5  $\mu\text{m}$  wide channel encompasses the center of the NW.

#### **4.4.2: Sensor Chip Device Testing**

The Si NW sensor chip was connected to the Agilent Semiconductor Parameter Analyzer system (described in 4.3.5: Device Testing) for the biosensing experiments. The response of a Si NW device to phosphate buffer, PC/PG liposomes, and Tween20 is demonstrated in Figure 30. Before the start of the sensing experiment in Figure 30, the Si NW sensor chip was incubated in phosphate buffer. After a 10 min incubation in buffer, the sensing experiment was started with an applied voltage of 500 mV. The device in the buffer solution demonstrated a current value of about 2.53  $\mu\text{A}$ . To ensure that the Si NW device had reached an equilibrium conductivity value in buffer at the 500 mV applied voltage, 20  $\mu\text{L}$  of phosphate buffer was added to the device three times (see Figure 30, circles marked as 1, 2, and 3 at 100 s, 200 s, and 400 s, respectively). The current in the Si NW device slightly decreased and reached a baseline value in buffer at 2.52  $\mu\text{A}$  after these three additions of phosphate buffer. A 60  $\mu\text{L}$  drop of the PC/PG liposome solution was then added to the Si NW device (Figure 30, see circle 4 at 550 s). With the addition of the lipid solution, the current in the device nearly instantly decreased to a value of 2.49  $\mu\text{A}$  (a 1.2 % change in current) and remained steady at this decreased value over the course of 20 min. It is believed that the decrease in NW current can be attributed to the formation of a lipid bilayer around the NW (described in more detail below, see 4.4.3: Mechanism of Lipid Layer Formation & Destruction). It should be noted that the

response time of the device to the liposome solution was 88 s. After allowing the Si NW to sit in the liposome solution for 20 min, 30  $\mu\text{L}$  of Tween20 solution was added to the Si NW device (see Figure 30, circle 5 at 1400 s). The current in the NW quickly increased to a value of 2.525  $\mu\text{A}$  (a 1.4 % change in current), which was the baseline current value of the NW in phosphate buffer. Therefore, it is presumed that the Tween20 solution removed the lipid bilayer from the NW surface and lead to a return of NW conductance to its baseline value. It is important to note that the recovery time for this device was 124 s.

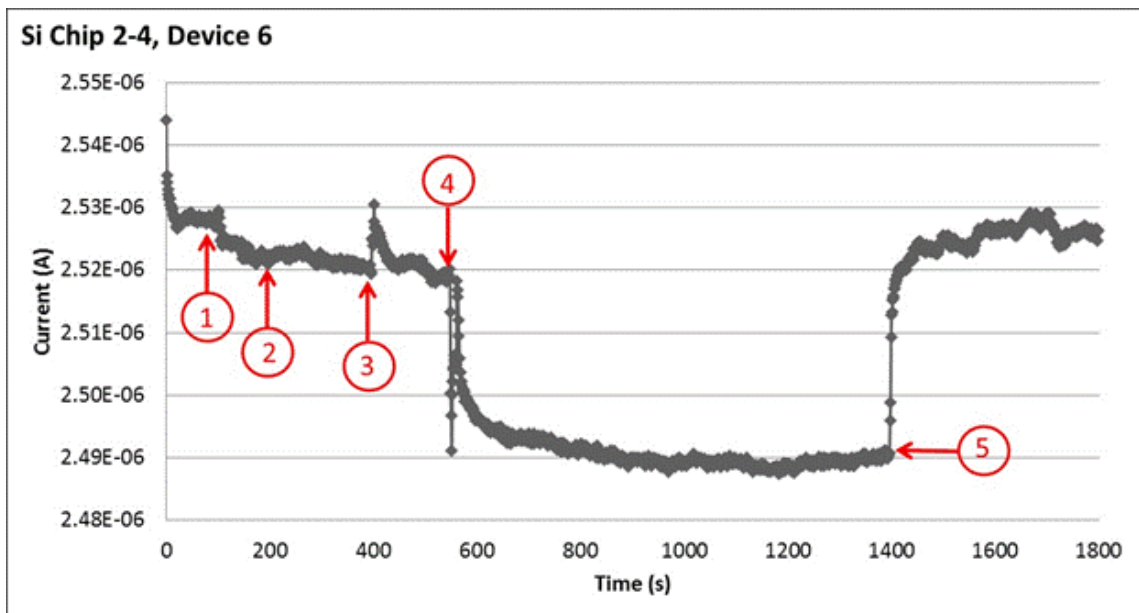


Figure 30: Current (A) versus time (s) response of a Si NW device upon the addition of 1) 20  $\mu\text{L}$  of phosphate buffer, 2) 20  $\mu\text{L}$  of phosphate buffer, 3) 20  $\mu\text{L}$  phosphate buffer, 4) 60  $\mu\text{L}$  PC/PG liposomes, and 5) 30  $\mu\text{L}$  Tween20 solution.

To confirm that the decrease in NW current was attributed to the formation of a lipid bilayer on the Si NWs, confocal fluorescence microscopy was performed. The

liposomes utilized in the experiments contained a green fluorophore and would result in green NW fluorescence if lipids did encapsulate the NW. Figure 31A demonstrates that the NW is fluorescing green following its exposure to the liposome solution (the image corresponds to the region between 4 and 5 in Figure 30). As a consequence, it can be concluded the liposomes did break open and encapsulate the NW, forming a lipid layer around the NW surface [33]–[37]. The green fluorescing NW in image Figure 31A is clear upon focusing in on the NW region (Figure 31B). A fluorescence intensity line scan taken down the length of the NW (indicated by the dashed arrow line in Figure 31B, “line scan direction”) is shown in Figure 31C. The average fluorescence intensity of the NW (the region marked with red arrows in Figure 31C) is 38. The peaks in fluorescence intensity on either side of the NW region are due to the polyimide insulation layer as it is inherently fluorescent and should be ignored. Due to the fact that there are no multiple integer jumps in fluorescence intensity in the NW region, it can be assumed that a lipid bilayer, rather than lipid multilayers, did indeed encapsulate the Si NW [36]. The NW devices resemble and mimic an *E. coli* cell membrane at this stage in the experiments.

Fluorescence microscopy was also performed following the exposure of the lipid encapsulated NWs to the Tween20 solution. Figure 32A demonstrates a loss in the NW’s green fluorescence after Tween20 is applied to the sensor chip (corresponding to region 5, the end of the experiment, in Figure 30). Zooming in on the NW region in Figure 32A is shown as the image in Figure 32B; clearly the NW demonstrates nearly zero fluorescence. A fluorescence intensity line scan taken down the length of the NW (indicated by the dashed arrow line in Figure 32B, “line scan direction”) is shown in

Figure 32C. The average fluorescence intensity of the NW (the region marked with red arrows in Figure 31C) is 11. Again, the peaks in fluorescence intensity on either side of the NW region are due to the polyimide insulation layer as it is inherently fluorescent and should be ignored. Due to the fact that the NW exhibits nearly zero fluorescence, it can be assumed that the Tween20 solution did remove the lipid bilayer from the NW surface.

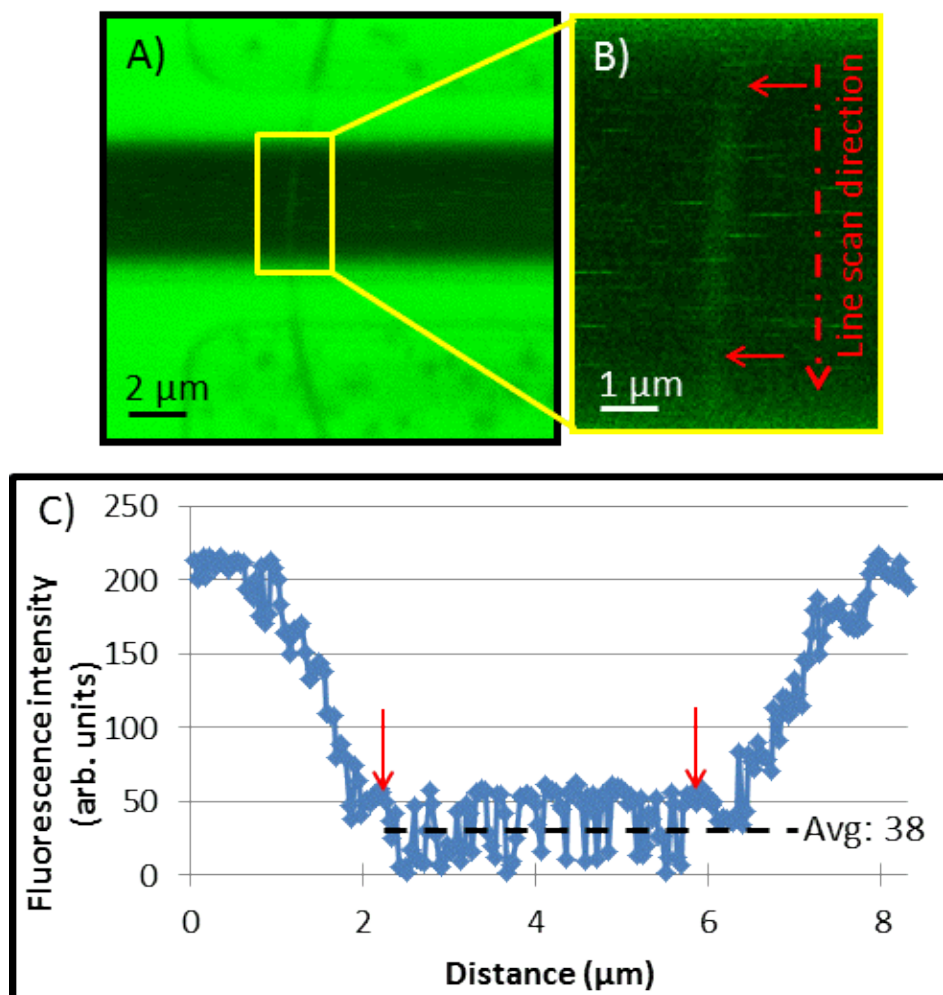


Figure 31: Confocal fluorescence microscopy (at a magnification of 40 x) of a Si NW after exposure to the PC/PG liposome solution (A). A zoomed in image of the NW in (A) is shown in image (B). A fluorescence intensity line scan taken along the NW's length in image (B) is shown in (C). The red arrows in image (C) indicate the NW region with an average fluorescence intensity of 38.

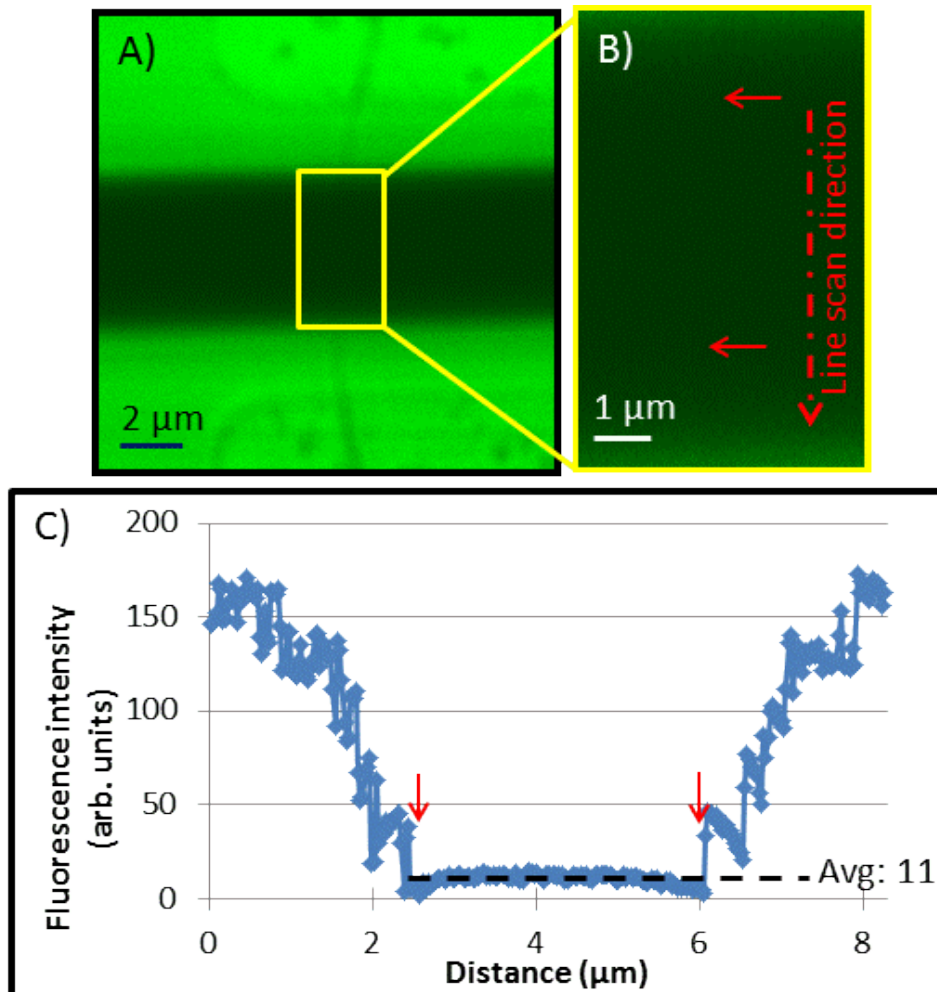
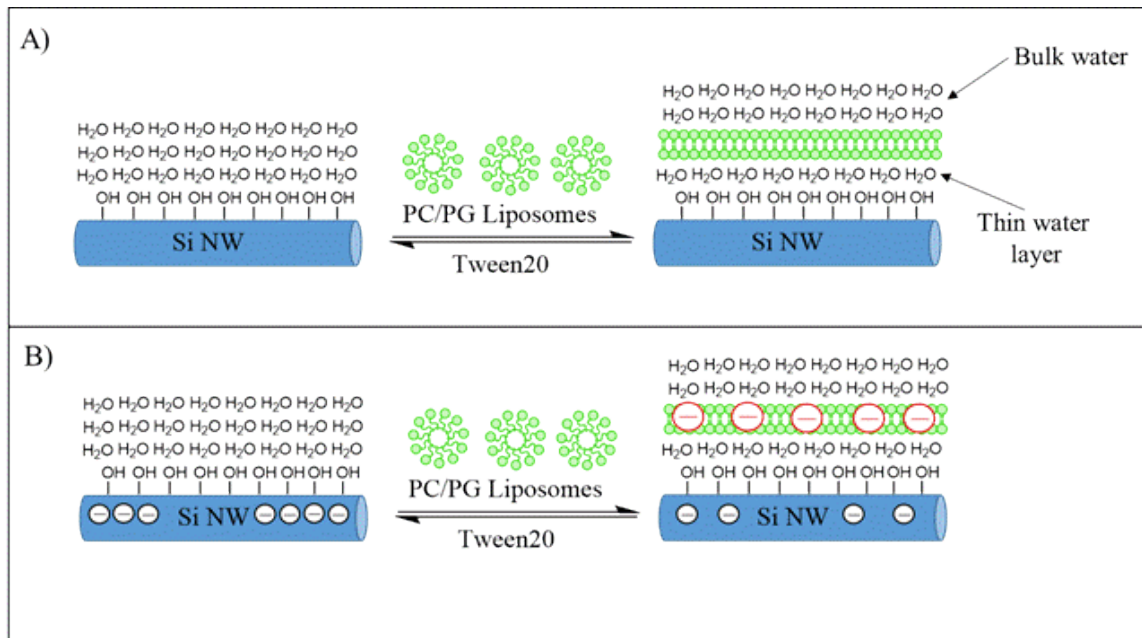


Figure 32: Confocal fluorescence microscopy (at a magnification of 40 x) of a Si NW after exposure to the Tween20 solution (A). A zoomed in image of the NW in (A) is shown in image (B). A fluorescence intensity line scan taken along the NW's length in image (B) is shown in (C). The red arrows in image (C) indicate the NW region with an average fluorescence intensity of 11.

#### 4.4.3: Mechanism of Lipid Layer Formation & Destruction on NWs

It has been demonstrated that liposome vesicles break open and assemble into fluid bilayers on Si and quartz substrates [79]–[81]. It is proposed that as vesicles fuse and assemble as a bilayer onto a solid support, a thin water layer acts as a cushion

between the substrate and the supported bilayer, subsequently pushing the bulk of the water to the other side of the bilayer [79]–[81]. It is presumed that upon exposure to the PC/PG liposomes in our experiments (Figure 30, the circle marked as 4 and Figure 31A and B), this mechanism occurs. A schematic of this mechanism in which PC/PG bilayer formation occurs on a Si NW device is demonstrated in Figure 33A. A. Noy’s group proposed that formation of a water supported membrane on NWs with diameters down to 20 nm is energetically favorable if the liposome vesicle diameter is less than 60 nm [36]. Due to the fact that in our experiments, 50 nm liposome vesicles and 120 nm in diameter NWs were utilized, spontaneous formation of a lipid membrane on the NWs was indeed favorable and was observed.



**Figure 33: Mechanism of lipid bilayer formation/destruction on a Si NW and effect on NW conductance. A) shows the formation of the lipid bilayer with PC/PG liposomes and the destruction of the bilayer using Tween20, B) demonstrates the change in NW conductance due to lipid encapsulation.**

The PC/PG liposome solution and the resulting bilayer that is formed on the NW contains an overall net negative charge [78]. As described above, the Si NWs utilized in the experiments are n-type and therefore contain an excess of negatively charged carriers (electrons). It is expected that bilayer formation on the n-type Si NW devices would lead to a decrease in NW conductance as the bilayer acts as a negative gate on the surface of the device [1], [6]. The negative gate (lipid bilayer) on the n-type Si NW would result in a suppression of negative carriers (surface carrier depletion) and a decrease in NW conductance. A schematic of this mechanism is shown in Figure 33B. The formation of a PC/PG bilayer on the Si NW devices did lead to a reduction in NW conductance (see Figure 30, circle marked as 4) of about 1-2 % in our experiments. We also attribute the decrease in the NW conductance to the lipid bilayer shielding the NW from the bulk water solution. A. Noy proposed that the decrease in NW conductance of lipid encapsulated NWs was likely due to the bulk water screening effect of the lipid layer on the NW [33], [35]. Confirmation that the NW decrease in conductance was due to lipid bilayer formation was also demonstrated by fluorescence microscopy (Figure 31).

Tween20 is a commonly used detergent for lipid solubilization [82]. It is expected that upon exposure of a lipid encapsulated NW to a concentrated solution of Tween20, the lipid bilayer would solubilize and be removed from the Si NW. A schematic showing the removal of the lipid bilayer from the NW surface using Tween20 is demonstrated in Figure 33A. It is expected that upon removal of the lipid bilayer from the NW using a concentrated Tween20 solution, the conductance in the NW would return to its original conductance value in the bulk solution (see Figure 33B). In our experiments, the

application of a 10 % Tween20 solution to a lipid encapsulated NW, Figure 30, the circle marked as 5, produced a quick return of the NW conductance to its original value in the phosphate buffer solution. Therefore, we conclude that this increase in NW conductivity is due to the removal of the lipid bilayer from the NW. Confocal fluorescence microscopy, Figure 32, confirms that no lipids remain immobilized on the Si NW surface after exposure to the Tween20 solution.

#### **4.5: Conclusions**

The design, fabrication, and insulation of a Si NW sensor chip for investigation of bacterial cell membrane interactions and mechanisms were presented. Si NW devices on the sensor chip were exposed to a PC/PG liposome solution, with the same ratio as to mimic an *E. coli* cell membrane. Lipid bilayer formation was found to occur on the Si NWs spontaneously as was demonstrated by both electrical measurements and confocal fluorescence microscopy. The electrical measurements revealed a 1-2 % decrease in NW conductance upon lipid encapsulation of the Si NW devices. This decrease in NW conductivity can be attributed to the overall net negative charge of the lipid bilayer as well as the bilayer effectively shielding the NW from the external bulk solution. The fluorescence microscopy images demonstrated relatively uniform NW fluorescence post exposure to the PC/PG liposome solution indicating near bilayer formation on the NW surface. The lipid encapsulated NW devices were exposed to a concentrated solution of solubilizing agent, Tween20. The Tween20 removed the lipid bilayer from the NW devices as was evidenced by both electrical measurements and fluorescence microscopy. The electrical data revealed that post exposure to Tween20, the conductance in the NW

returned to its conductivity value in phosphate buffer indicating the full removal of the lipid layer from the NW. Fluorescence microscopy demonstrated an absence of NW fluorescence revealing that Tween20 did indeed remove the lipids from the NW surface. The studies presented in this chapter demonstrate that 1) a lipid layer mimicking an *E. coli* cell membrane can be formed on Si NW devices and 2) the in-situ electrical detection of *E. coli* like cell membrane formation and destruction on Si NW devices can be achieved. The membrane encapsulated Si NW devices demonstrate a novel platform to electrically probe bacterial cell membrane mechanisms and interactions.

#### **4.6: Acknowledgements**

The authors are appreciative of the helpful discussions with Stoyan Jeliakov, Hany Issa, and Madhuri Mairipelly. EHW, MVR, and JAS gratefully acknowledge the financial support of the National Science Foundation (Grant # ECCS-0901712).

## 5: FINAL CONCLUSIONS & FUTURE WORK

There is a strong demand for accurate (i.e. selective) and sensitive detection of biological species in liquids such as blood, saliva, urine, drinking water, and food [4], [6]. Due to their high surface-to-volume ratio and electrical characteristics, Si, SiC, and GaN NWs arranged as FET type devices may lead to the most accurate, selective, sensitive, and easy to read method of biological detection to date. Si NW based FETs have already proven the sensitive and selective detection of biological species [2], [6], [29]. SiC and GaN FET biosensors have yet to be developed since biofunctionalization of these two materials is just now being demonstrated [16], [27]. The disadvantages or downfalls of conventional biosensing techniques and the abilities of Si NW FET biosensors demonstrate that Si, SiC, and GaN FET devices need to be further investigated and studied for accurate, ultrasensitive biological detection.

In chapter 2: Selective streptavidin bioconjugation on silicon and silicon carbide nanowires for biosensor applications, the following conclusions were made:

- (1) Confirmation that Si NWs have the ability to be functionalized for the selective attachment of biomolecules, specifically biocompatibility towards proteins. Si NWs are an ideal platform for incorporation into FET based biosensors as has been demonstrated by the literature.

(2) SiC NWs do have the propensity to be functionalized for the selective attachment of protein molecules and are biocompatible towards these molecules. SiC NWs behave very similarly to Si NWs in their ability to be functionalized as well as their biocompatibility. Biofunctionalized SiC NWs have the potential to be used as biosensing platforms in FET devices.

In chapter 3: Solution-based functionalization of gallium nitride nanowires for protein sensor development, the following conclusions were made:

(1) GaN NWs can be functionalized in-solution for the selective attachment of protein molecules and are biocompatible towards these molecules. GaN NWs behave very similarly to Si NWs and SiC NWs towards functionalization schemes and biocompatibility. Biofunctionalized GaN NWs have the potential to be used as biosensing platforms in FET devices.

The studies conducted revealed that all three NW materials, Si, SiC, and GaN, are ideal platforms for biological sensing. SiC and GaN NWs could indeed be incorporated into FET based biosensors. It is likely that SiC and GaN NWs would lead to the selective, sensitive detection of biomolecules as has been demonstrated with Si NWs [29]. SiC and GaN NWs may even surpass Si NWs in FET based biosensing due to their unique electronic, chemical, and physical properties. It is evident that selective and sensitive SiC and GaN NW based FET biosensors will likely emerge in the near future. It is important

to note that the research conducted in chapter 2: Selective streptavidin bioconjugation on silicon and silicon carbide nanowires for biosensor applications was published in the *Journal of Materials Research* in 2013 [70]. The work in chapter 3: Solution-based functionalization of gallium nitride nanowires for protein sensor development has been accepted for publication in the journal *Surface Science* and will be published in 2014.

The studies presented in chapter 4: Lipid Encapsulated Silicon Nanowire Devices- A Novel Detection Method for Probing Bacterial Cell Membrane Mechanisms and Interactions explored Si NW FETs for probing cellular mechanisms and interactions. The following conclusions were made in this chapter:

- (1) A lipid layer mimicking an *E. coli* cell membrane can be formed on Si NW FET devices.
- (2) The in-situ electrical detection of *E. coli* cell membrane formation and destruction on Si NW FET devices can be achieved. A 1-2 % decrease in current occurs upon formation of the lipid bilayer on the NWs and the current returns to its baseline value in buffer upon the destruction of the lipid layer using Tween20.

The *E. coli* cell membrane encapsulated Si NW FET devices demonstrate a novel platform to electrically probe bacterial cell membrane mechanisms and interactions. It is expected that this work will be published in the journal *Biosensors and Bioelectronics* in late 2014.

Further work is currently being conducted to study the interaction of antimicrobial peptides on the *E. coli* cell membrane encapsulated Si NW FETs. Figure 34 demonstrates the electrical signal of a Si NW FET device upon the addition of phosphate buffer at the circles marked 1 and 2, PC/PG liposomes at the circle marked as 3, and a strong antimicrobial peptide (NA-CATH) at the circle marked as 4.

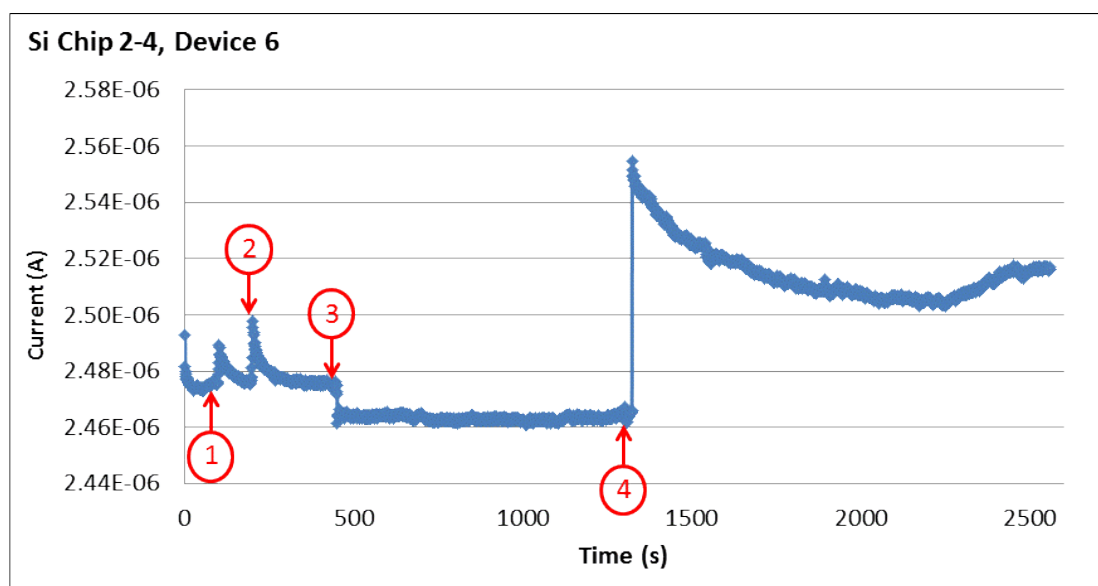
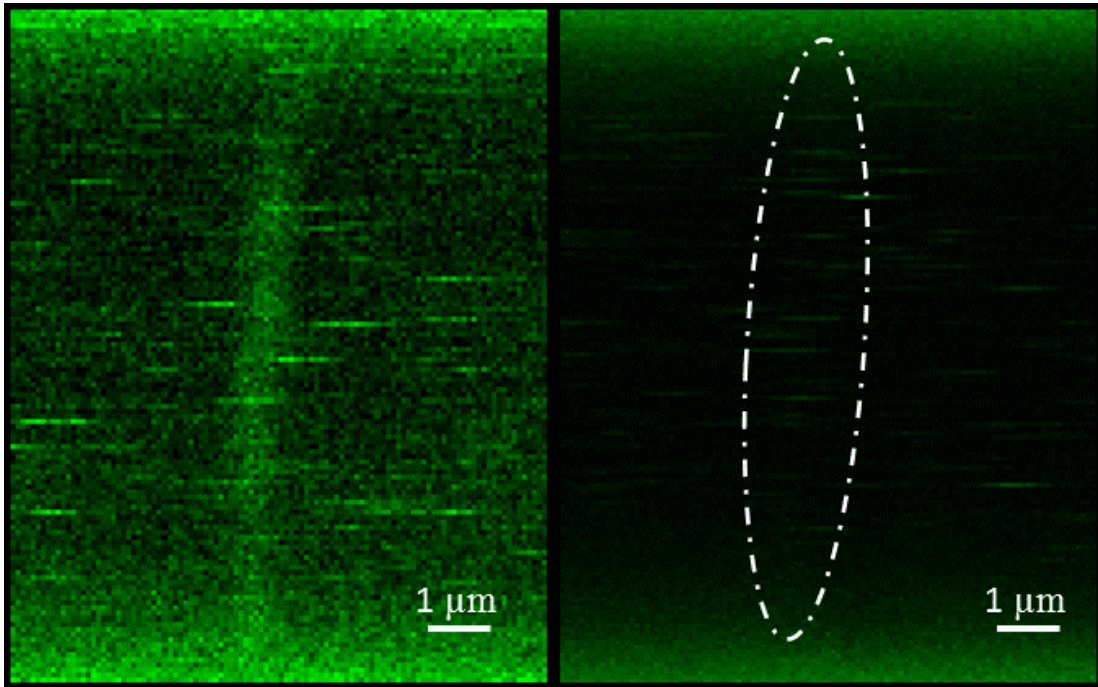


Figure 34: Si NW FET device response to 1) phosphate buffer, 2) phosphate buffer, 3) PC/PG liposome solution, and 4) the NA-CATH antimicrobial peptide.

After the stabilization of the device in buffer (the circles marked as 1 and 2 in Figure 34), the PC/PG liposome solution caused the device current to decrease (circle marked as 3 in Figure 34); likely due to the formation of a lipid bilayer on the NW as described in 4.4.3: Mechanism of Lipid Layer Formation & Destruction. Addition of the NA-CATH peptide to the lipid encapsulated NW caused the NW current to dramatically increase, see circle 4 of Figure 34. This increase in current can likely be attributed to the

removal of the lipid bilayer from the NW and the subsequent interaction of the NA-CATH peptide with the NW surface [78]. The NA-CATH peptide contains a very high net positive charge (+15) and it is expected that after the peptide removes the lipid bilayer from the NW, the NW device current would remain at an increased value as compared to the pure buffer solution [78]. The charge of the NA-CATH peptide acts as a positive gate on the n-type Si NW surface and thus induces an increase in NW current as compared to the pure buffer. Figure 35 demonstrates the corresponding confocal fluorescence microscopy images (at a 40 x magnification) after the addition of the PC/PG liposome solution (left image) and after the addition of the NA-CATH peptide (right image) to the Si NW FET device. The left image of Figure 35 corresponds to the region between the circles marked as 3 and 4 in Figure 34 and the right image of Figure 35 corresponds to the region after the circle marked as 4 in Figure 34.



**Figure 35:** Confocal fluorescence microscopy images of a Si NW FET device after exposure to PC/PG liposomes (left image) and after the application of NA-CATH to the lipid coated NW (right image). The dashed oval in the right image marks the region of the non-fluorescing NW. The scale bar in both images is 1  $\mu\text{m}$ .

From the fluorescence microscopy images, it is evident that application of the PC/PG solution to the NW device results in the formation of a lipid bilayer on the NW. Subsequent exposure of the lipid encapsulated NW to NA-CATH causes the lipid bilayer to be removed from the NW. However, it is likely that the mechanism of NA-CATH bilayer destruction is different from that of Tween20 described above in 4.4.3: Mechanism of Lipid Layer Formation & Destruction. While Tween20 solubilizes lipids, NA-CATH tends to aggregate lipid molecules, disrupting bilayer interactions as was seen in Figure 35 (right image) [78], [82]. In the right image of Figure 35 (after NA-CATH exposure), liposomes are still visible in the FET fluid channel suggesting that the lipids are aggregated rather than solubilized from the NW surface.

In the future, experiments will be conducted in which different concentrations of the NA-CATH peptide as well different peptides are applied to the lipid encapsulated Si NW FETs. It is possible that the kinetics of antimicrobial peptide destruction of bacterial cell membranes may be obtained using the novel FET devices demonstrated in chapter 4 of this work. The *E. coli* cell membrane coated Si NW FETs may be able to provide direct electrical measurements that give insight into the mechanisms and interactions of antimicrobial or antibiotic compounds with bacterial cell membranes.

## REFERENCES

- [1] F. Patolsky, G. Zheng, and C. M. Lieber, "Nanowire-Based Biosensors," *Anal. Chem.*, vol. 78, no. 13, pp. 4260–4269, 2006.
- [2] F. Patolsky, G. Zheng, and C. M. Lieber, "Nanowire sensors for medicine and the life sciences.," *Nanomedicine (Lond.)*, vol. 1, no. 1, pp. 51–65, Jun. 2006.
- [3] Y. Paska, T. Stelzner, O. Assad, U. Tisch, S. Christiansen, and H. Haick, "Molecular Gating of Silicon Nanowire Field-Effect Transistors with Nonpolar Analytes," *ACS Nano*, vol. 6, no. 1, pp. 335–345, Dec. 2011.
- [4] S. J. Pearton, F. Ren, Y.-L. Wang, B. H. Chu, K. H. Chen, C. Y. Chang, W. Lim, J. Lin, and D. P. Norton, "Recent advances in wide bandgap semiconductor biological and gas sensors," *Prog. Mater. Sci.*, vol. 55, no. 1, pp. 1–59, Jan. 2010.
- [5] N. Chaniotakis and N. Sofikiti, "Novel semiconductor materials for the development of chemical sensors and biosensors: a review.," *Anal. Chim. Acta*, vol. 615, no. 1, pp. 1–9, May 2008.
- [6] C. M. Lieber and F. Patolsky, "Nanowire nanosensors," *Mater. Today*, vol. 8, no. 4, pp. 20–28, 2005.
- [7] E. Stern, A. Vacic, M. A. Reed, "Semiconducting Nanowire Field-Effect Transistor Biomolecular Sensors," vol. 55, no. 11, pp. 3119–3130, 2008.
- [8] Y. Cui, Q. Wei, H. Park, and C. M. Lieber, "Nanowire nanosensors for highly sensitive and selective detection of biological and chemical species.," *Science*, vol. 293, no. 5533, pp. 1289–92, Aug. 2001.
- [9] G.-J. Zhang and Y. Ning, "Silicon nanowire biosensor and its applications in disease diagnostics: a review.," *Anal. Chim. Acta*, vol. 749, pp. 1–15, Oct. 2012.
- [10] X. P. A. Gao, G. Zheng, and C. M. Lieber, "Subthreshold regime has the optimal sensitivity for nanowire FET biosensors.," *Nano Lett.*, vol. 10, no. 2, pp. 547–52, Feb. 2010.
- [11] D. J. Guo, A. I. Abdulagatov, D. M. Rourke, K. A. Bertness, S. M. George, Y. C. Lee, and W. Tan, "GaN nanowire functionalized with atomic layer deposition

- techniques for enhanced immobilization of biomolecules.,” *Langmuir*, vol. 26, no. 23, pp. 18382–91, Dec. 2010.
- [12] G. T. Hermanson, *Bioconjugate techniques*, 2nd ed. USA: Academic Press, 2008.
- [13] B. Baur, G. Steinhoff, J. Hernando, O. Purruicker, M. Tanaka, B. Nickel, M. Stutzmann, and M. Eickhoff, “Chemical functionalization of GaN and AlN surfaces,” *Appl. Phys. Lett.*, vol. 87, no. 26, p. 263901, 2005.
- [14] A. Arranz, C. Palacio, D. García-Fresnadillo, G. Orellana, A. Navarro, and E. Muñoz, “Influence of surface hydroxylation on 3-aminopropyltriethoxysilane growth mode during chemical functionalization of GaN Surfaces: an angle-resolved X-ray photoelectron spectroscopy Study,” *Langmuir*, vol. 24, no. 16, pp. 8667–71, Aug. 2008.
- [15] B. S. Kang, F. Ren, L. Wang, C. Lofton, W. W. Tan, S. J. Pearton, A. Dabiran, A. Osinsky, and P. P. Chow, “Electrical detection of immobilized proteins with ungated AlGaIn/GaN high-electron-mobility Transistors,” *Appl. Phys. Lett.*, vol. 87, no. 2, p. 023508, 2005.
- [16] E. H. Williams, A. V. Davydov, A. Motayed, S. G. Sundaresan, P. Bocchini, L. J. Richter, G. Stan, K. Steffens, R. Zangmeister, J. A. Schreifels, and M. V. Rao, “Immobilization of streptavidin on 4H–SiC for biosensor development,” *Appl. Surf. Sci.*, vol. 258, no. 16, pp. 6056–6063, Jun. 2012.
- [17] J. Kim, P. Seidler, L. S. Wan, and C. Fill, “Formation, structure, and reactivity of amino-terminated organic films on silicon substrates,” *J. Colloid Interface Sci.*, vol. 329, no. 1, pp. 114–9, Jan. 2009.
- [18] J. Wang, L. S. Pedroza, and A. Poissier, “Water Dissociation at the GaN(101 $\bar{0}$ ) Surface: Structure, Dynamics and Surface Acidity,” pp. 2–9, 2012.
- [19] R. M. Petoral, G. R. Yazdi, A. Lloyd Spetz, R. Yakimova, and K. Uvdal, “Organosilane-functionalized wide band gap semiconductor surfaces,” *Appl. Phys. Lett.*, vol. 90, no. 22, p. 223904, 2007.
- [20] R. Yakimova, G. Steinhoff, R. M. Petoral, C. Vahlberg, V. Khranovskyy, G. R. Yazdi, K. Uvdal, and A. Lloyd Spetz, “Novel material concepts of transducers for chemical and biosensors,” *Biosens. Bioelectron.*, vol. 22, no. 12, pp. 2780–5, Jun. 2007.
- [21] R. Yakimova, R. M. Petoral, G. R. Yazdi, C. Vahlberg, A. Lloyd Spetz, and K. Uvdal, “Surface functionalization and biomedical applications based on SiC,” *J. Phys. D: Appl. Phys.*, vol. 40, no. 20, pp. 6435–6442, Oct. 2007.

- [22] M. J. Schoning and A. Poghossian, “Recent advances in biologically sensitive field-effect transistors (BioFETs),” *Analyst*, vol. 127, no. 9, pp. 1137–1151, Sep. 2002.
- [23] P. Bergveld, “Development of an Ion-Sensitive Solid-State Device for Neurophysiological Measurements,” *Biomedical Engineering, IEEE Transactions*, vol. BME-17, no. 1, pp. 70–71, 1970.
- [24] M. Hasan, M. F. Huq, and Z. H. Mahmood, “A review on electronic and optical properties of silicon nanowire and its different growth techniques.,” *Springerplus*, vol. 2, no. 1, p. 151, Dec. 2013.
- [25] P. Bergveld, “Future applications of ISFETs,” *Sensors Actuators B Chem.*, vol. 4, no. 1–2, pp. 125–133, May 1991.
- [26] M. Stutzmann, J. A. Garrido, M. Eickhoff, and M. S. Brandt, “Direct biofunctionalization of semiconductors: A survey,” *Phys. status solidi*, vol. 203, no. 14, pp. 3424–3437, 2006.
- [27] B. S. Simpkins, K. M. McCoy, L. J. Whitman, and P. E. Pehrsson, “Fabrication and characterization of DNA-functionalized GaN nanowires,” *Nanotechnology*, vol. 18, no. 35, p. 355301, Sep. 2007.
- [28] G. S. Aluri, A. Motayed, A. V. Davydov, V. P. Oleshko, K. A. Bertness, N. A. Sanford, and M. V. Rao, “Highly selective GaN-nanowire/TiO<sub>2</sub>-nanocluster hybrid sensors for detection of benzene and related environment pollutants.,” *Nanotechnology*, vol. 22, no. 29, p. 295503, Jul. 2011.
- [29] F. Patolsky, G. Zheng, and C. M. Lieber, “Fabrication of silicon nanowire devices for ultrasensitive, label-free, real-time detection of biological and chemical species.,” *Nat. Protoc.*, vol. 1, no. 4, pp. 1711–24, Jan. 2006.
- [30] K.-I. Chen, B.-R. Li, and Y.-T. Chen, “Silicon nanowire field-effect transistor-based biosensors for biomedical diagnosis and cellular recording investigation,” *Nano Today*, vol. 6, no. 2, pp. 131–154, Apr. 2011.
- [31] Z. Gao, A. Agarwal, A. D. Trigg, N. Singh, C. Fang, C.-H. Tung, Y. Fan, K. D. Buddharaju, and J. Kong, “Silicon nanowire arrays for label-free detection of DNA.,” *Anal. Chem.*, vol. 79, no. 9, pp. 3291–7, May 2007.
- [32] G. Zheng, F. Patolsky, Y. Cui, W. U. Wang, and C. M. Lieber, “Multiplexed electrical detection of cancer markers with nanowire sensor arrays,” *Nat Biotech.*, vol. 23, no. 10, pp. 1294–1301, Oct. 2005.

- [33] N. Misra, J. A. Martinez, S. J. Huang, Y. Wang, P. Stroeve, and C. P. Grigoropoulos, "Bioelectronic silicon nanowire devices," vol. 106, no. 33, 2009.
- [34] A. Noy, "Bionanoelectronics.," *Adv. Mater.*, vol. 23, no. 7, pp. 807–20, Feb. 2011.
- [35] J. A. Martinez, N. Misra, Y. Wang, P. Stroeve, C. P. Grigoropoulos, and A. Noy, "Highly efficient biocompatible single silicon nanowire electrodes with functional biological pore channels.," *Nano Lett.*, vol. 9, no. 3, pp. 1121–6, Mar. 2009.
- [36] S.-C. J. Huang, A. B. Artyukhin, J. A. Martinez, D. J. Sirbully, Y. Wang, J.-W. Ju, P. Stroeve, and A. Noy, "Formation, stability, and mobility of one-dimensional lipid bilayers on polysilicon nanowires," *Nano Lett.*, vol. 7, no. 11, pp. 3355–9, Nov. 2007.
- [37] L. Römhildt, A. Gang, L. Baraban, J. Opitz, and G. Cuniberti, "High yield formation of lipid bilayer shells around silicon nanowires in aqueous solution," *Nanotechnology*, vol. 24, no. 35, p. 355601, Sep. 2013.
- [38] C.-P. Chen, A. Ganguly, C.-Y. Lu, T.-Y. Chen, C.-C. Kuo, R.-S. Chen, W.-H. Tu, W. B. Fischer, K.-H. Chen, and L.-C. Chen, "Ultrasensitive in situ label-free DNA detection using a GaN nanowire-based extended-gate field-effect-transistor sensor.," *Anal. Chem.*, vol. 83, no. 6, pp. 1938–43, Mar. 2011.
- [39] Y.-T. Lai, A. Ganguly, L.-C. Chen, and K.-H. Chen, "Direct voltammetric sensing of L-cysteine at pristine GaN nanowires electrode," *Biosens. Bioelectron.*, vol. 26, no. 4, pp. 1688–91, Dec. 2010.
- [40] Z. Li, Y. Chen, X. Li, T. I. Kamins, K. Nauka, and R. S. Williams, "Sequence-Specific Label-Free DNA Sensors Based on Silicon Nanowires," no. 2, pp. 10–12, 2004.
- [41] J. Kim, M. Junkin, D.-H. Kim, S. Kwon, Y. S. Shin, P. K. Wong, and B. K. Gale, "Applications, techniques, and microfluidic interfacing for nanoscale biosensing," *Microfluid. Nanofluidics*, vol. 7, no. 2, pp. 149–167, Apr. 2009.
- [42] M. Shao, D. D. D. Ma, and S.-T. Lee, "Silicon Nanowires – Synthesis, Properties, and Applications," *Eur. J. Inorg. Chem.*, vol. 2010, no. 27, pp. 4264–4278, 2010.
- [43] C. M. Lieber, "Semiconductor nanowires: A platform for nanoscience and nanotechnology.," *MRS Bull.*, vol. 36, no. 12, pp. 1052–1063, Dec. 2011.
- [44] J. A. Siooss, R. L. Stoermer, M. Y. Sha, and C. D. Keating, "Silica-Coated, Au/Ag Striped Nanowires for Bioanalysis," *Langmuir*, vol. 23, no. 22, pp. 11334–11341, Sep. 2007.

- [45] S. Krylyuk, A. V. Davydov, and I. Levin, "Tapering control of Si nanowires grown from SiCl<sub>4</sub> at reduced pressure.," *ACS Nano*, vol. 5, no. 1, pp. 656–64, Jan. 2011.
- [46] B. Krishnan, R. V. K. G. Thirumalai, Y. Koshka, S. Sundaresan, I. Levin, A. V. Davydov, and J. N. Merrett, "Substrate-Dependent Orientation and Polytype Control in SiC Nanowires Grown on 4H-SiC Substrates," *Cryst. Growth Des.*, vol. 11, no. 2, pp. 538–541, Jan. 2011.
- [47] CasaXPS, "Software for XPS data analysis." Casa Software Ltd., 2012.
- [48] I. Horcas, R. Fernández, J. M. Gómez-Rodríguez, J. Colchero, J. Gómez-Herrero, and A. M. Baro, "WSXM: a software for scanning probe microscopy and a tool for nanotechnology," *Rev. Sci. Instrum.*, vol. 78, no. 1, p. 013705, Jan. 2007.
- [49] ImageJ, "Software for image analysis." NIH, 2012.
- [50] C. Wagner, A. V. Naumkin, A. Kraut-Vass, J. W. Allison, C. J. Powell, and J. R. Rumble, "NIST X-ray photoelectron spectroscopy database, NIST standard reference database 20," 2007.
- [51] M. Morita, T. Ohmi, E. Hasegawa, M. Kawakami, and M. Ohwada, "Growth of native oxide on a silicon surface," *J. Appl. Phys.*, vol. 68, no. 3, p. 1272, 1990.
- [52] M. F. Beaux, N. J. Bridges, M. DeHart, T. E. Bitterwolf, and D. N. McIlroy, "X-ray photoelectron spectroscopic analysis of the surface chemistry of silica nanowires," *Appl. Surf. Sci.*, vol. 257, no. 13, pp. 5766–5771, Apr. 2011.
- [53] E. T. Vandenberg, L. Bertilsson, B. Liedberg, K. Uvdal, R. Erlandsson, H. Elwing, and I. Lundström, "Structure of 3-aminopropyl triethoxy silane on silicon oxide," *J. Colloid Interface Sci.*, vol. 147, no. 1, pp. 103–118, Nov. 1991.
- [54] K. Bierbaum, M. Kinzler, C. Woell, M. Grunze, G. Haehner, S. Heid, and F. Effenberger, "A Near Edge X-ray Absorption Fine Structure Spectroscopy and X-ray Photoelectron Spectroscopy Study of the Film Properties of Self-Assembled Monolayers of Organosilanes on Oxidized Si(100)," *Langmuir*, vol. 11, no. 2, pp. 512–518, Feb. 1995.
- [55] L. A. Ruiz-Taylor, T. L. Martin, and P. Wagner, "X-ray Photoelectron Spectroscopy and Radiometry Studies of Biotin-Derivatized Poly(l-lysine)-grafted-Poly(ethylene glycol) Monolayers on Metal Oxides," *Langmuir*, vol. 17, no. 23, pp. 7313–7322, Oct. 2001.
- [56] Z. Yang, Z. Xie, H. Liu, F. Yan, and H. Ju, "Streptavidin-Functionalized Three-Dimensional Ordered Nanoporous Silica Film for Highly Efficient

- Chemiluminescent Immunosensing,” *Adv. Funct. Mater.*, vol. 18, no. 24, pp. 3991–3998, 2008.
- [57] Y. Hijikata, H. Yaguchi, M. Yoshikawa, and S. Yoshida, “Composition analysis of SiO<sub>2</sub>/SiC interfaces by electron spectroscopic measurements using slope-shaped oxide films,” *Appl. Surf. Sci.*, vol. 184, no. 1–4, pp. 161–166, Dec. 2001.
- [58] A. Busiakiewicz, A. Huczko, H. Lange, P. J. Kowalczyk, M. Rogala, W. Kozłowski, Z. Klusek, W. Olejniczak, K. Polanski, and S. Cudziło, “Silicon carbide nanowires: chemical characterization and morphology investigations,” *Phys. status solidi*, vol. 245, no. 10, pp. 2094–2097, 2008.
- [59] B. Hornetz, H.-J. Michel, and J. Halbritter, “ARXPS studies of SiO<sub>2</sub>-SiC interfaces and oxidation of 6H SiC single crystal Si- (OOI) and C- (OOI) surfaces,” *J. Mater. Res.*, vol. 9, no. 12, pp. 3088–3094, 1994.
- [60] J. Q. Hu, Q. Y. Lu, K. B. Tang, B. Deng, R. R. Jiang, Y. T. Qian, W. C. Yu, G. E. Zhou, X. M. Liu, and J. X. Wu, “Synthesis and Characterization of SiC Nanowires through a Reduction–Carburization Route,” *J. Phys. Chem. B*, vol. 104, no. 22, pp. 5251–5254, May 2000.
- [61] G. Shen, D. Chen, K. Tang, Y. Qian, and S. Zhang, “Silicon carbide hollow nanospheres, nanowires and coaxial nanowires,” *Chem. Phys. Lett.*, vol. 375, no. 1–2, pp. 177–184, Jun. 2003.
- [62] F. Amy and Y. J. Chabal, “Interaction of H, O<sub>2</sub>, and H<sub>2</sub>O with 3C-SiC surfaces,” *J. Chem. Phys.*, vol. 119, no. 12, pp. 6201–6209.
- [63] G. Cicero, G. Galli, and A. Catellani, “Interaction of Water Molecules with SiC(001) Surfaces,” *J. Phys. Chem. B*, vol. 108, no. 42, pp. 16518–16524, Sep. 2004.
- [64] P. G. Righetti, G. Tudor, and K. Ek, “Isoelectric points and molecular weights of proteins,” *J. Chromatogr. A*, vol. 220, no. 2, pp. 115–194, Oct. 1981.
- [65] Y. Wang, W. Qian, Y. Tan, and S. Ding, “A label-free biosensor based on gold nanoshell monolayers for monitoring biomolecular interactions in diluted whole blood,” *Biosens. Bioelectron.*, vol. 23, no. 7, pp. 1166–70, Feb. 2008.
- [66] G. S. Aluri, A. Motayed, A. V. Davydov, V. P. Oleshko, K. A. Bertness, and M. V. Rao, “Nitro-Aromatic Explosive Sensing Using GaN Nanowire-Titania Nanocluster Hybrids,” vol. 13, no. 5, pp. 1883–1888, 2013.
- [67] R. Bajpai, A. Motayed, A. V. Davydov, V. P. Oleshko, G. S. Aluri, K. A. Bertness, M. V. Rao, and M. E. Zaghoul, “UV-assisted alcohol sensing using SnO<sub>2</sub>

- functionalized GaN nanowire devices,” *Sensors Actuators B Chem.*, vol. 171–172, pp. 499–507, Aug. 2012.
- [68] R. Bajpai, A. Motayed, A. V. Davydov, K. A. Bertness, and M. E. Zaghloul, “UV-Assisted Alcohol Sensing With Zinc Oxide-Functionalized Gallium Nitride Nanowires,” *IEEE Electron Device Lett.*, vol. 33, no. 7, pp. 1075–1077, Jul. 2012.
- [69] G. S. Aluri, A. Motayed, A. V. Davydov, V. P. Oleshko, K. A. Bertness, N. A. Sanford, and R. V. Mulpuri, “Methanol, ethanol and hydrogen sensing using metal oxide and metal (TiO<sub>2</sub>)-Pt composite nanoclusters on GaN nanowires: a new route towards tailoring the selectivity of nanowire/nanocluster chemical sensors,” *Nanotechnology*, vol. 23, no. 17, p. 175501, May 2012.
- [70] E. H. Williams, J. A. Schreifels, M. V. Rao, A. V. Davydov, V. P. Oleshko, N. J. Lin, K. L. Steffens, S. Krylyuk, K. A. Bertness, A. K. Manocchi, and Y. Koshka, “Selective streptavidin bioconjugation on silicon and silicon carbide nanowires for biosensor applications,” *J. Mater. Res.*, vol. 28, no. 01, pp. 68–77, Aug. 2012.
- [71] K. A. Bertness, N. A. Sanford, and A. V. Davydov, “GaN Nanowires Grown by Molecular Beam Epitaxy,” vol. 17, no. 4, pp. 847–858, 2011.
- [72] N. J. Watkins, G. W. Wicks, and Y. Gao, “Oxidation study of GaN using x-ray photoemission spectroscopy,” *Appl. Phys. Lett.*, vol. 75, no. 17, p. 2602, 1999.
- [73] H. Ishikawa, S. Kobayashi, and Y. Koide, “Effects of surface treatments and metal work functions on electrical properties at p-GaN / metal interfaces,” vol. 81, no. February, pp. 1315–1322, 1997.
- [74] S. Pal, R. Mahapatra, S. K. Ray, B. R. Chakraborty, S. M. Shivaprasad, S. K. Lahiri, and D. N. Bose, “Microwave plasma oxidation of gallium nitride,” vol. 425, pp. 20–23, 2003.
- [75] T. Sasaki and T. Matsuoka, “Substrate-polarity dependence of metal-organic vapor-phase epitaxy-grown GaN on SiC,” *J. Appl. Phys.*, vol. 64, no. 9, pp. 4531–4535, 1988.
- [76] E. Vanea and V. Simon, “XPS study of protein adsorption onto nanocrystalline aluminosilicate microparticles,” *Appl. Surf. Sci.*, vol. 257, no. 6, pp. 2346–2352, Jan. 2011.
- [77] S. Wolter, J. DeLucca, S. Mohny, R. Kern, and C. Kuo, “An investigation into the early stages of oxide growth on gallium nitride,” *Thin Solid Films*, vol. 371, no. 1–2, pp. 153–160, Aug. 2000.

- [78] M. Juba, D. Porter, S. Dean, S. Gillmor, and B. Bishop, "Characterization and performance of short cationic antimicrobial peptide isomers.," *Biopolymers*, vol. 100, no. 4, pp. 387–401, Jul. 2013.
- [79] B. W. Koenig, S. Krueger, W. J. Orts, C. F. Majkrzak, N. F. Berk, J. V Silverton, and K. Gawrisch, "Neutron Reflectivity and Atomic Force Microscopy Studies of a Lipid Bilayer in Water Adsorbed to the Surface of a Silicon Single Crystal," no. 11, pp. 1343–1350, 1996.
- [80] S. J. Johnson, T. M. Bayerl, D. C. McDermott, G. W. Adam, A. R. Rennie, R. K. Thomas, and E. Sackmann, "Structure of an adsorbed dimyristoylphosphatidylcholine bilayer measured with specular reflection of neutrons.," *Biophys. J.*, vol. 59, no. 2, pp. 289–94, Feb. 1991.
- [81] P. S. Cremer and S. G. Boxer, "Formation and Spreading of Lipid Bilayers on Planar Glass Supports," vol. 291, pp. 2554–2559, 1999.
- [82] M. le Maire, P. Champeil, and J. V Moller, "Interaction of membrane proteins and lipids with solubilizing detergents.," *Biochim. Biophys. Acta*, vol. 1508, no. 1–2, pp. 86–111, Nov. 2000.

## **BIOGRAPHY**

Elissa H. Williams graduated Summa Cum Laude from W.T. Woodson High School, Fairfax, VA, in 2004. She received her Bachelor of Science degree in Chemistry & Biochemistry from George Mason University (GMU) in 2008, graduating with a Summa Cum Laude institutional honor. During her time as a graduate student, Elissa served as a Guest Researcher at the National Institute of Standards and Technology (NIST, Gaithersburg MD) and also as the supervisor of the George Mason University Testing & Tutoring Center. Elissa received her Master of Science degree in Chemistry from George Mason University in 2010. Elissa received a Ph.D. in Chemistry & Biochemistry from GMU in 2014 and aspires to be a leading scientist in the field of Applied Chemistry. On June 16<sup>th</sup>, 2014, Elissa will begin an associateship tenure as a National Research Council (NRC) Postdoctoral Fellow at NIST in Gaithersburg, MD.